

EXTRAGALACTIC SCIENCE, COSMOLOGY AND GALACTIC ARCHAEOLOGY WITH THE SUBARU PRIME FOCUS SPECTROGRAPH (PFS)

MASAHIRO TAKADA¹, RICHARD ELLIS², MASASHI CHIBA³, JENNY E. GREENE⁴, HIROAKI AIHARA^{1,5}, NOBUO ARIMOTO⁶, KEVIN BUNDY¹, JUDITH COHEN², OLIVIER DORÉ^{2,7}, GENEVIEVE GRAVES⁴, JAMES E. GUNN⁴, TIMOTHY HECKMAN⁸, CHRIS HIRATA², PAUL HO⁹, JEAN-PAUL KNEIB¹⁰, OLIVIER LE FÈVRE¹⁰, LIHWAI LIN⁹, SURHUD MORE¹, HITOSHI MURAYAMA^{1,11}, TOHRU NAGAO¹², MASAMI OUCHI¹³, MICHAEL SEIFFERT^{2,7}, JOHN SILVERMAN¹, LAERTE SODRÉ JR¹⁴, DAVID N. SPERGER^{1,4}, MICHAEL A. STRAUSS⁴, HAJIME SUGAI¹, YASUSHI SUTO⁵, HIDEKI TAKAMI⁶, ROSEMARY WYSE⁸

Draft version January 24, 2022

ABSTRACT

The Subaru Prime Focus Spectrograph (PFS) is a massively-multiplexed fiber-fed optical and near-infrared 3-arm spectrograph ($N_{\text{fiber}}=2400$, $380 \leq \lambda \leq 1260\text{nm}$, 1.3 degree diameter hexagonal field), offering unique opportunities in survey astronomy. Following a successful external design review the instrument is now under construction with first light anticipated in late 2017. Here we summarize the science case for this unique instrument in terms of provisional plans for a Subaru Strategic Program of $\simeq 300$ nights. We describe plans to constrain the nature of dark energy via a survey of emission line galaxies spanning a comoving volume of $9.3h^{-3}\text{Gpc}^3$ in the redshift range $0.8 < z < 2.4$. In each of 6 independent redshift bins, the cosmological distances will be measured to 3% precision via the baryonic acoustic oscillation scale, and redshift-space distortion measures will be used to constrain structure growth to 6% precision. In the near-field cosmology program, radial velocities and chemical abundances of stars in the Milky Way and M31 will be used to infer the past assembly histories of spiral galaxies and the structure of their dark matter halos. Data will be secured for 10^6 stars in the Galactic thick-disk, halo and tidal streams as faint as $V \sim 22$, including stars with $V < 20$ to complement the goals of the Gaia mission. A medium-resolution mode with $R = 5,000$ to be implemented in the red arm will allow the measurement of multiple α -element abundances and more precise velocities for Galactic stars, elucidating the detailed chemo-dynamical structure and evolution of each of the main stellar components of the Milky Way Galaxy and of its dwarf spheroidal galaxies. The M31 campaign will target red giant branch stars with $21.5 < V < 22.5$, obtaining radial velocities and metallicities over an unprecedented area of 65 deg^2 . For the extragalactic program, our simulations suggest the wide wavelength range of PFS will be particularly powerful in probing the galaxy population and its clustering over a wide redshift range. We propose to conduct a color-selected survey of $1 < z < 2$ galaxies and AGN over 16 deg^2 to $J \simeq 23.4$, yielding a fair sample of galaxies with stellar masses above $\sim 10^{10} M_{\odot}$ at $z \simeq 2$. A two-tiered survey of higher redshift Lyman break galaxies and Lyman alpha emitters will quantify the properties of early systems close to the reionization epoch. PFS will also provide unique spectroscopic opportunities beyond these currently-envisaged surveys, particularly in the era of Euclid, LSST and TMT.

Subject headings: PFS — cosmology — galactic archaeology — galaxy evolution

1. INTRODUCTION

¹ Kavli Institute for the Physics and Mathematics of the Universe (Kavli IPMU, WPI), The University of Tokyo, Chiba 277-8583

² California Institute of Technology, Pasadena, CA 91125, U.S.A

³ Astronomical Institute, Tohoku University, Sendai, 980-8578

⁴ Department of Astrophysical Sciences, Princeton University, Princeton, NJ 08544, U.S.A

⁵ Department of Physics, The University of Tokyo, Tokyo, 113-0033

⁶ National Astronomical Observatory of Japan, Tokyo, 181-8588

⁷ Jet Propulsion Laboratory, California Institute of Technology, Pasadena, CA, U.S.A.

⁸ Department of Physics & Astronomy, Johns Hopkins University, Baltimore, MD 21218, U.S.A.

⁹ Institute of Astronomy and Astrophysics, Academia Sinica, Taipei 10617, Taiwan

¹⁰ Laboratoire d'Astrophysique de Marseille, F-13388 Marseille Cedex 13, France

¹¹ Physics Department, University of California, Berkeley and Lawrence Berkeley National Laboratory, Berkeley, California 94720, U.S.A

¹² The Hakubi Center for Advanced Research, Kyoto University, Kyoto 606-8302

¹³ Institute for Cosmic Ray Research, The University of Tokyo, Chiba 277-8582

¹⁴ Instituto de Astronomia, Geofísica e Ciências Atmosféricas São Paulo, 05508-090, Brazil

There is currently a major expansion in survey imaging capability via the use of CCD and near-infrared detector mosaics on a wide range of ground-based telescopes. Such imaging surveys provide accurate photometric and other data to enable the study of gravitational lensing signals which trace the distribution of dark matter and to conduct census studies of Galactic structures and distant star-forming galaxies. For over a decade it has been recognized that a similar revolution would be provided by a massively-multiplexed spectrograph on a large aperture telescope. Spectra provide precise radial velocities, metallicities and emission line properties for faint and distant sources and enable additional probes of cosmology. The main challenge in realizing this second revolution has been access to a wide field telescope, essential for efficient multi-object spectroscopy of panoramic fields, and the cost of implementing the appropriate instrumentation.

A proposal to construct a Subaru Prime Focus Spectrograph (PFS) emerged following the cancellation in May 2009 of the Gemini-sponsored Wide-Field Multi-Object Spectrometer (WFMOS). WFMOS was envisaged as a facility instrument on the Subaru telescope sharing the optics designed for the new prime focus camera, Hyper Suprime-Cam (HSC). Two teams received Gemini funding for a conceptual design study

of WFMOS and, prior to cancellation, a team led by Caltech and the Jet Propulsion Laboratory (JPL) secured preliminary approval. Soon after, however, the Gemini Board indicated they did not have sufficient funding to proceed and the WFMOS project was terminated.

The Kavli Institute for the Physics and Mathematics of the Universe (Kavli IPMU) at the University of Tokyo submitted a proposal for stimulus funding to the Japanese government in September 2009 using design concepts pioneered in the WFMOS study led by Caltech and JPL. The successful outcome of this proposal in early 2010 initiated the present PFS partnership which now includes Caltech/JPL, Princeton and Johns Hopkins Universities, the Laboratoire d’Astrophysique de Marseille, Academia Sinica Institute of Astronomy & Astrophysics (ASIAA) Taiwan, the University of São Paulo and the Laboratório Nacional de Astrofísica in Brazil.

In addition to the leadership funding provided by Kavli IPMU, four important milestones have enabled progress and led to the decision to commence construction. Firstly, in January 2011 the Subaru Users Meeting endorsed the PFS project as a next-generation instrument for the Subaru Prime Focus, recognizing the international PFS team and its responsibilities. This decision led to the establishment of a PFS project office at Kavli IPMU in early 2011 and an allocation of funds and manpower by the National Astronomical Observatory of Japan (NAOJ) towards integration, commissioning and survey operations. A second milestone followed the MOU in December 2011 between the Director-General of NAOJ and the Director of Kavli IPMU, that anticipates a Subaru Strategic Program for PFS providing up to 300 nights of observing time for the PFS team in collaboration with the Japanese astronomical community. These developments provided the essential impetus for the science plans and technical requirements defined in this article. The third milestone was a successful Conceptual Design Review (CoDR) held in March 2012 which triggered the decision to commence construction with first light anticipated in 2017. The fourth milestone was a successful Preliminary Design Review (PDR) held in Feb 2013. The CoDR and PDR documentations included a detailed science case for PFS and a list of technical requirements. This article reproduces these for general interest.

This article is not intended to provide a technical description of PFS but a brief overview is helpful (see Fig. 1). Further technical details of the instrument and its current design can be found at <http://sumire.ipmu.jp/en/2652> (Sugai et al. 2012). PFS is designed to allow simultaneous low and intermediate-resolution spectroscopy of 2400 astronomical targets over a 1.3 degree diameter hexagonal field. It shares the *Wide Field Corrector* and associated *Field Rotator* and *Hexapod* already constructed for the HSC. An array of 2400 optical fibers is in the *Prime Focus Instrument* and each fiber tip position is controlled in-plane by a two-stage piezoelectric *Fiber Positioner* Cobra system. Each fiber can be positioned within a particular patrol region such that these patrol regions fully sample the 1.3 degree field. A *Fiber Connector* relays light to four identical fixed-format 3-arm twin-dichroic all-Schmidt *Spectrographs* providing continuous wavelength coverage from 380nm to 1.26 μ m. The blue and red channels will use two Hamamatsu 2K \times 4K edge-buttable fully-depleted CCDs (as in HSC). The near-infrared channel will use a new Teledyne 4RG 4K \times 4K HgCdTe 1.7 μ m cut-off array. We also plan to have a medium resolution mode with $R \simeq 5000$ for the red channel, which is feasible by using a simple grating/grism exchange mechanism at the red-channel

spectrograph.

The present article describes the detailed scientific case for PFS in the context of a Subaru Strategic Program (SSP) of $\simeq 300$ nights of observing time. Since such a program would not be implemented until 2017 at the earliest, the main motivation in formulating the team’s plans at this stage is in providing a list of key science requirements for the technical design. In Sections 2 – 4 we describe 3 key components of the science case for PFS that will likely form the basis of the Subaru Strategic Program. For each of these 3 cases we provide a summary, a detailed science justification and survey strategy as well as the flow-down from these to the technical requirements for the instrument. We summarize these science requirements for PFS in more detail in Section 5 and discuss some outstanding issues in Section 6.

2. COSMOLOGY

Summary: PFS will be remarkably powerful in spectroscopic surveys of faint galaxies because of its large multiplex gain and the 8.2 meter aperture of the Subaru telescope. The extended wavelength coverage provided by the red and near-infrared spectrograph arms (650 – 1260 nm) will permit a unique survey of [O II] emission-line galaxies extending over the redshift range $0.8 \leq z \leq 2.4$. As large-scale structures remain in the linear regime at high redshift, such a survey will give detailed new information on the cosmological parameters as well as the growth rate of structure formation. This combination will provide a valuable test of alternative models of gravity on large scale which may provide a possible explanation for dark energy. Multi-color data planned to arrive from the HSC imager will be used to select target galaxies for spectroscopy and the expected high throughput should yield a $\simeq 75\%$ success rate of detecting [O II] emission at $S/N > 8.5$. Herein, we propose to conduct a 100 night cosmological survey over 1400 deg², sampling galaxies within a comoving volume of 9 (Gpc/h)³ over $0.8 \leq z \leq 2.4$. This will complement the lower redshift survey being undertaken by the SDSS BOSS collaboration.

The primary goals of the PFS cosmology survey are to: (1) measure the Hubble expansion rate and the angular diameter distance to 3% fractional accuracies in each of 6 redshift bins over $0.8 < z < 2.4$ via the baryonic acoustic oscillation (BAO) method, (2) use the distance measurements for determining the dark energy density parameter $\Omega_{de}(z)$ to about 7% accuracy in each redshift bin, when combined with lower redshift BAO measurements, (3) use the geometrical constraints to determine the curvature parameter Ω_K to 0.3% accuracy, and (4) measure the redshift-space distortion (RSD) in order to reconstruct the growth rate of large-scale structure to 6% accuracy since a redshift $z = 2.4$. These PFS measurements of the large scale galaxy distribution can be combined with complementary weak lensing information from the HSC survey in order to significantly improve the cosmological and structure growth constraints and reduce uncertainties arising from galaxy bias and nonlinear effects that are otherwise major sources of systematic error in spectroscopic surveys.

2.1. Cosmology Objectives

The accelerated expansion of the Universe is the most intriguing problem in cosmology. It either requires the introduction of a mysterious form of energy, “dark energy”, or it could signal a breakdown of Einstein theory of General Relativity on cosmological scales. To distinguish between these and

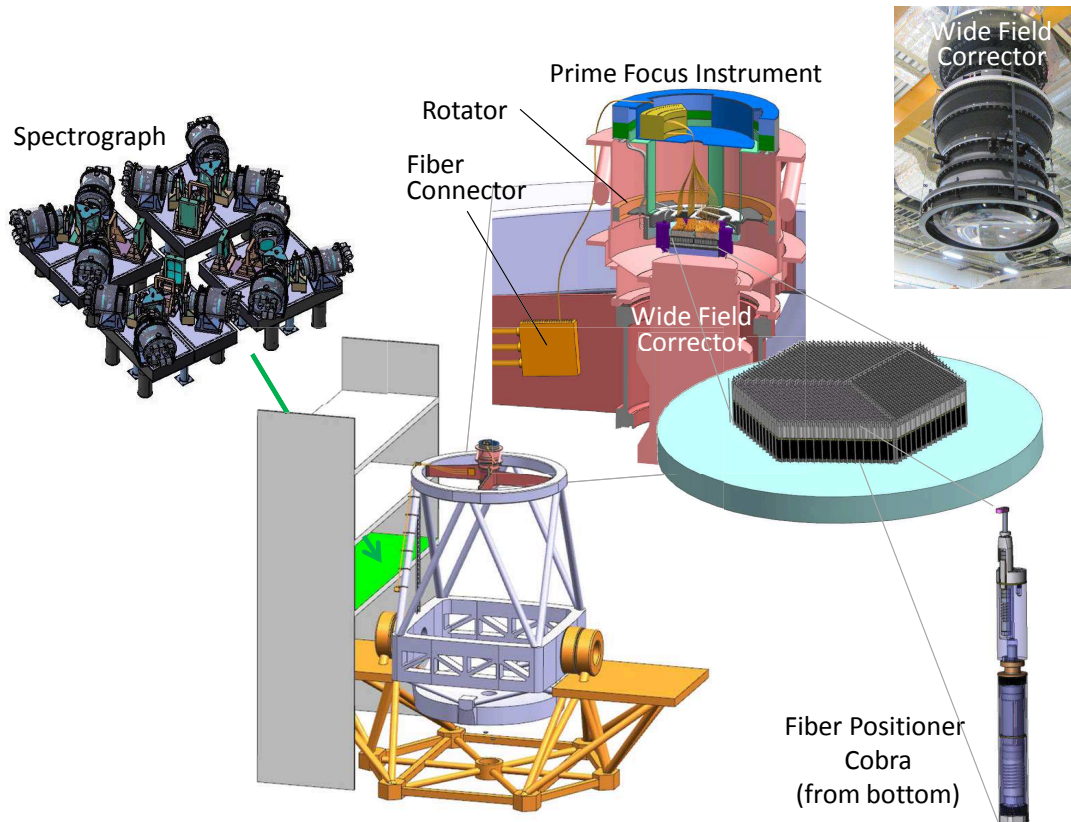


FIG. 1.— A brief overview of the baseline design of PFS instruments, which consist of components **Wide Field Corrector**, **Field Rotator**, **Prime Focus Unit**, and **Fiber Positioner**. A **Fiber Connector** relays light to four identical fixed-format 3-arm twin-dichroic all-Schmidt **Spectrographs** providing continuous wavelength coverage from 380nm to 1.26 μ m.

other possibilities requires precise observational constraints on both the expansion history of the universe and the growth rate of large-scale structure.

Measurements of galaxy clustering statistics are one of the most powerful means of addressing the nature of dark energy. The tight coupling between baryons and photons prior to the decoupling epoch of $z \simeq 1100$ leaves a characteristic imprint on the pattern of galaxy clustering on large scales – the so-called baryonic acoustic oscillation (BAO) scale. As the BAO length scale is precisely constrained to be 147 ± 0.6 Mpc from cosmic microwave background (CMB) experiments (Komatsu et al. 2011; Planck 2013 Results XVI 2013), it offers a standard ruler by which we can infer the angular diameter distance and the Hubble expansion rate from the observed correlation function of the galaxy distribution. The BAO scale is in the linear or weakly-nonlinear density regime and thus provides a robust geometrical test. Furthermore, if uncertainties arising from galaxy bias can be removed or accurately modeled, we can use the amplitude and shape information of the galaxy correlation function in order to constrain cosmological parameters as well as the growth rate of structure formation.

Recognizing this, the main scientific questions we seek to address with the PFS cosmology survey are:

1. *Is the cosmic acceleration caused by dark energy or does it represent a failure of Einstein's theory of gravity on cosmological length scales?*
2. *What is the physics of the early universe that generates*

the primordial fluctuations as the seed of large-scale structures?

To address these fundamental questions, the main goals for the PFS cosmology survey are to:

- Constrain the angular diameter distance and the Hubble expansion rate via the BAO experiment to a precision comparable with, or better than, existing, ongoing or planned BAO surveys.
- Derive the BAO constraints in a redshift range that is complementary to those probed by the existing or planned BAO surveys on the time scale of the PFS survey.
- Utilize the unique capabilities of the 8.2m Subaru Telescope and the PFS spectrograph for maximizing cosmological science.
- Use the shape and amplitude of galaxy correlation function in order to constrain cosmological parameters as well as the growth rate of structure formation.
- Combine the weak lensing information, delivered from the HSC survey, with the PFS cosmology survey in order to improve the cosmological constraints by calibrating systematic uncertainties that cannot be resolved by either of the PFS and HSC surveys alone.

TABLE 1
INSTRUMENTATION PARAMETERS

Number of fibers	2400 (600 for each spectrograph)		
Field of view	1.3 deg (hexagonal – diameter of circumscribed circle)		
Field of view area	1.098 deg ²		
Fiber diameter	1.13'' diameter at the field center; 1.03'' at the edge		
	Blue arm	Red arm	IR arm
Wavelength coverage [nm]	380–670	650–1000	970–1260
Spectral resolution $\lambda/\Delta\lambda$	1900	2400	3500
Pixel scale [$\text{\AA}/\text{pix}$]	0.71	0.85	0.81
Read-out noise [e^- rms/pix]	3	3	4 ^a
Detector type/read-out mode	CCD	CCD	HgCdTe/SUTR
Thermal background [$e^-/\text{pix}/\text{sec}$]	None	None	0.013
Dark current [$e^-/\text{pix}/\text{sec}$]	3.89×10^{-4}	3.89×10^{-4}	0.01
Spectrograph image quality [μm rms/axis]	14	14 ^b	14
Sky continuum	21.56 mag AB/arcsec ² @ 1 μm at zenith ^c		
OH line brightness	16.6 mag AB/arcsec ² @ <i>J</i> band at zenith ^c		
Moonlight	None (dark time)		
Atmospheric extinction	Variable; continuum is 0.05 mag/airmass @ $\lambda > 0.9\mu\text{m}$		
Instrument throughput	Based on the Preliminary Design Review studies		
Grating wings	Lorentzian with $\frac{1}{3}$ of the true number of lines		
Diffuse stray light	2% of the total light reaching the detector		
Sky subtraction residuals	2% per pixel ^c		

NOTE. — PFS instrumentation parameters and associated assumptions used for estimating an expected signal-to-noise ratio for an observation of emission-line galaxies.

^a Per sub-exposure; if the NIR channel is not reset between exposures, the actual assumption corresponds to $4\sqrt{2} = 5.6 e^-$ rms.

^b Defocus within the thick CCD is considered separately.

^c Equivalent to 1% per 4-pixel resolution element.

2.2. PFS Cosmology Survey

Here we describe the parameters of the PFS cosmology survey that are required to meet the above scientific goals.

Firstly, we will consider which type of galaxies to target with PFS. Given the optical and near infrared wavelength coverage of PFS, [O II] emission-line galaxies (ELG; [O II] = 3727 \AA) are particularly useful tracers allowing an efficient survey out to high redshift beyond $z = 1$, a redshift range that is difficult to probe with 4m-class telescopes. Luminous red galaxies (LRGs) are a further potentially-useful tracer of large-scale structure as studied by the SDSS survey, but at $z \gtrsim 1.4$ they reveal weaker spectral features and are less abundant per unit volume. In the following we focus on ELGs to explore an optimal survey design. We may retain LRGs in future considerations of our survey plans, but their study is not required to meet the PFS cosmology objectives defined above.

2.2.1. Sensitivity of the PFS spectrograph

To estimate the feasibility of PFS for a wide-field survey of ELGs, we have studied the expected performance of measuring a [O II] line of a galaxy in our targeted redshift range for a representative exposure time during the dark lunar phase. In doing so, we properly account for the sky emission (continuum plus OH emission lines) and absorption as well as the instrumentation parameters for the current baseline design (as listed in Table 1).

Fig. 2 shows the expected signal-to-noise ratio of the [O II] line as a function of redshift, measured with each of the blue, red and near-infrared (NIR) arms of PFS. As a working example, here we assume $f_{[\text{O II}]} = 5 \times 10^{-17} \text{ erg/s/cm}^2$ for the total flux of the [O II] doublet, 15min for the exposure time, 0.8'' seeing size and $E(B - V) = 0.05$ for the Galactic dust extinction, respectively. The galaxy radial profile is assumed to be an exponential disk with a half-light radius of 0.3'' (about 3.5 kpc/ h for a galaxy at $z = 1$). Note that for

the galaxy yield forecasts, we use half-light radii from the COSMOS Mock Catalog (Jouvel et al. 2011), and re-compute the fiber aperture correction for each galaxy.¹⁵ We have assumed the 15 minute integration is split into 2 sub-exposures for cosmic ray (CR) detection in the CCD channel. The NIR channel will perform CR rejection by processing of the frames acquired during sample-up-the-ramp (SUTR) mode. The cosmology ETC assumes 4 e^- read noise per sub-exposure (appropriate for ~ 90 samples along a 450sec ramp). We will probably *not* reset the NIR channel in between sub-exposures, so we assume an overall read noise of $4\sqrt{2} = 5.6 e^-$ per pixel for the following study.

In addition to throughput and sky brightness considerations, we have considered several other potential limitations. Their amplitude is difficult to estimate, but they have been important for previous spectrographs and so we make an explicit allowance for them so as to adopt a conservative approach. The systematic sky subtraction residuals and small-angle stray light are very important factors in the study of galaxy spectra where [O II] is partially blended with a sky line. Diffuse stray light is a concern when [O II] lies in a cleaner part of the NIR spectrum.

- *Systematic sky subtraction residuals* – These are modeled by adding a “noise” term corresponding to some percentage of the sky counts in each spectral pixel. We currently set this to 2% of the brightest of the pixel and its neighbor on either side (equivalent to 1% sky subtraction accuracy on a 4-pixel resolution element).
- *Small-angle stray light* – We assign to the grating an effective number of lines that is 1/3 of the actual number.
- *Diffuse stray light* – We take 2% of the OH line flux

¹⁵ This assumes that the [O II] emission traces the *i*-band continuum in which the galaxy sizes were measured.

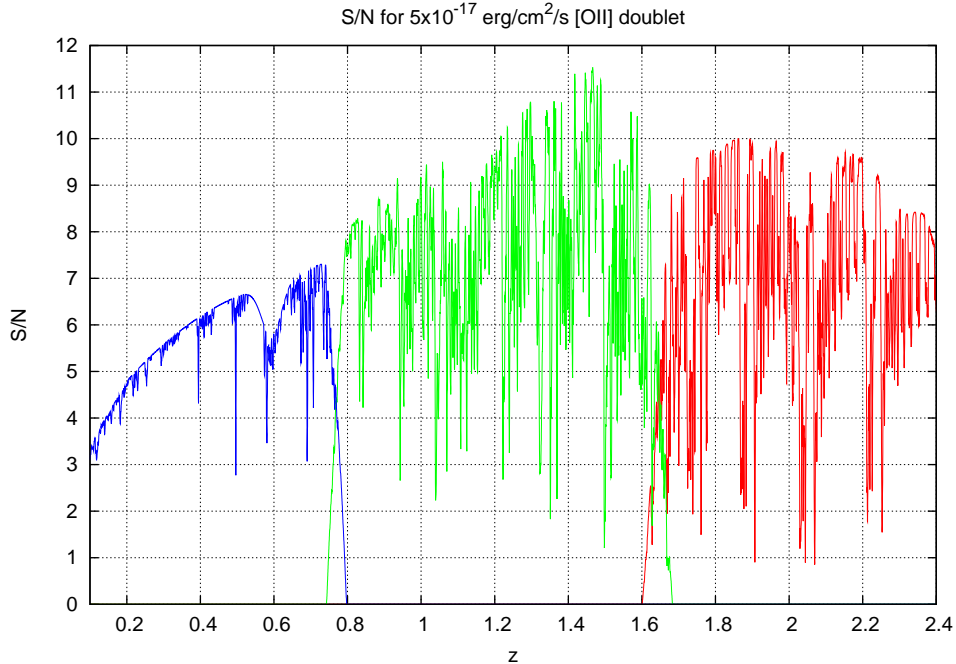


FIG. 2.— Expected signal-to-noise (S/N) ratio for measuring the [O II] emission line as a function of redshift; the blue, green and red curves show the results for the PFS blue, red and IR arms in Table 1, respectively, for an total emission line flux of 5×10^{-17} erg/cm²/s. To properly account for the uncertainties, we assumed the instrumentation parameters of the current baseline design listed in Table 1, an observation at the edge of the focal plane, and included the sky emission/absorption and the Galactic dust extinction of $E(B - V) = 0.05$ and 26 degrees for the zenith angle of the telescope. This computation assumes 15 min total exposure (split into two exposures; 450sec \times 2), $\sigma_v = 70$ km/s for the velocity dispersion (the intrinsic line width), and $0.8''$ for the seeing FWHM. We also accounted for the finite galaxy size relative to the seeing profile and the fiber size, assuming an exponential profile with scale radius $0.3''$ for the emission-line region (about 3.5 kpc/ h for a galaxy at $z = 1$). Note that S/N is estimated by the root-sum-square of the spectral pixels (i.e. it is a matched filter combining both doublet members). The current design allows a significant detection of [O II] emission line over a wide range of redshift, up to $z \simeq 2.4$ with near-equal sensitivities of the red and NIR arms.

incident on the detector and uniformly spread it over all pixels. (This may be appropriate for a detector that reflects 10% of the incident radiation, and then there are many surfaces that could potentially reflect this radiation back. Refining this parameter will be a priority since the S/N forecasts degrade rapidly if it gets worse.)

Continuing our conservative approach, we assumed the instrumentation throughput at the edge of the focal plane and 26 degrees for the zenith angle. (The latter corresponds to observations at declination 5° S, the southern boundary of the HSC survey region, and ± 0.5 hours away from transit.)

Fig. 2 shows that the current design of PFS allows a significant detection of the [O II] line over a wide range of redshift, up to $z \simeq 2.4$. Most importantly, the baseline design provides near-equal sensitivity of the red and NIR arms for measuring the [O II] line for the same exposure time. Hence PFS can execute a cosmological survey very efficiently over a wide range of redshift, provided sufficiently bright ELGs are available for study (see below).

In the following analysis, we set a threshold of $S/N = 8.5$ (matched filter) for detection of an ELG. In principle, it may be possible to accept less significant detections. However given the uncertainties in the airglow and the early stage of the instrument design, we consider it prudent to leave some margin in S/N .

2.2.2. Target selection of emission-line galaxies

We now address how to optimally select ELGs as suitable targets in the proposed redshift range. We will assume that

we can use the multi-color imaging data of the planned HSC survey which will be executed ahead of the PFS survey. The currently-planned HSC survey will reach $i \simeq 26$ (5σ for a point source and $2''$ aperture), in the 5 passbands *grizy* over ~ 1500 square degrees.

As seen in Fig. 2, if we target ELGs over the wide redshift range $0.8 \leq z \leq 2.4$, the wide wavelength coverage of red and NIR arms allows a very efficient selection of [OII] emission-line galaxies. A $g - r$ color cut is ideal for selecting galaxies in this redshift range: if an object is blue ($g - r < 0.3$), then it likely has no spectral breaks in the g and r bands – this means the redshift is high enough for the Balmer/4000Å break to have redshifted beyond the r band, but the Lyman break has not yet entered the g band. Furthermore, $g - r < 0.3$ implies a blue rest-frame UV slope, which has a strong correlation with the star-formation activity that produces [O II] emission.

To estimate the efficiency of various target selection algorithms, we used the COSMOS Mock Catalog (Jouvel et al. 2011), where fluxes of various emission lines of each galaxy are estimated based on physical parameters (SFR, stellar mass and metallicity) using the COSMOS 30 passband photometric data and zCOSMOS spectroscopic data. We have chosen the preliminary target selection cuts:

$$22.8 \leq g \leq 24.2 \text{ AND } -0.1 < g - r < 0.3 \\ \text{AND NOT } (g > 23.6 \text{ AND } r - i > 0.3). \quad (1)$$

The HSC depth ($g, r, i \simeq 26$ mag AB at 5σ) is sufficient to find the target galaxies *and* to provide accurate $g - r$ and $r -$

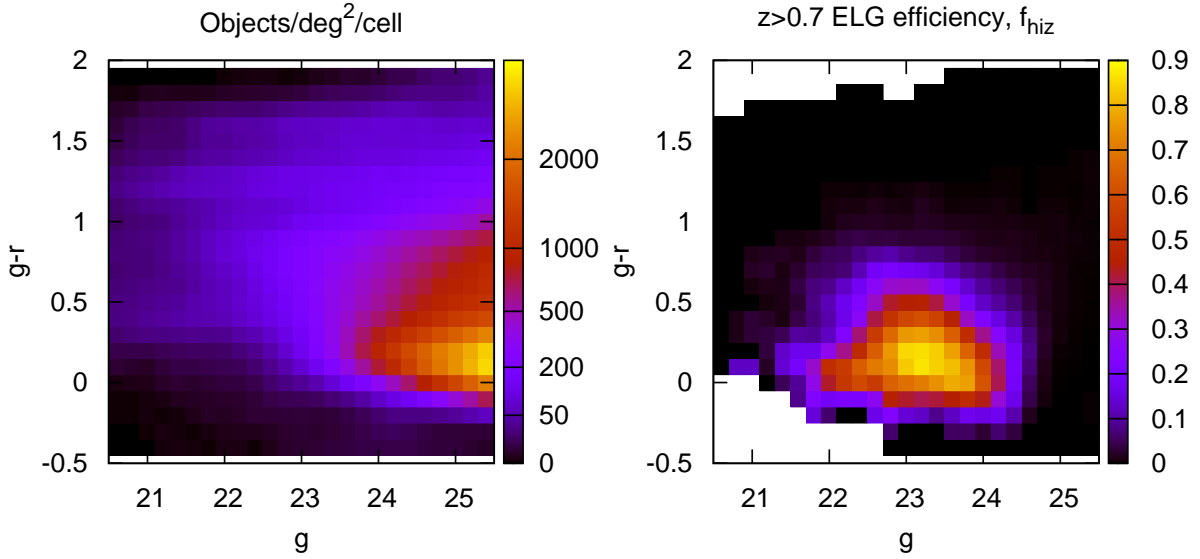


FIG. 3.— *Left panel:* The distribution of objects in the COSMOS Mock Catalog in the color-magnitude diagram. *Right:* The fraction of objects in each cell that are $z > 0.7$ ELGs with [O II] doublets detectable at $\geq 8.5\sigma$ in PFS in 2×7.5 min exposures. The third dimension ($r - i$) is not shown on this 2D plot, but allows us to select lower or higher redshift galaxies within the PFS survey range.

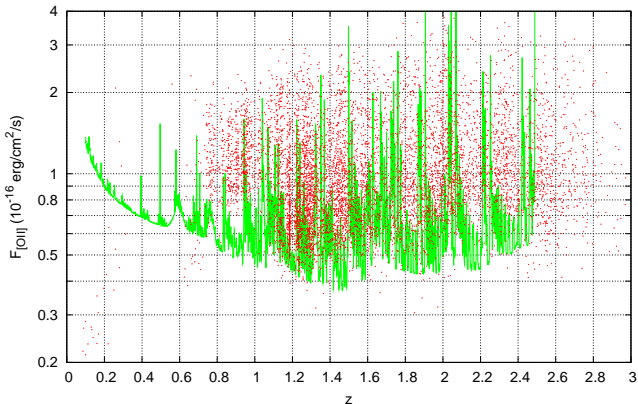


FIG. 4.— The sensitivity of PFS (green curve; 8.5σ , $2 \times 450s$ exposures, dark time) to the [O II] doublet at $r_{\text{eff}} = 0.3''$ and 1:1 line ratio, versus the selected targets (red points). Note that the redshift $z = 2.4$ corresponds to the long wavelength end of the NIR arm. Most targets will yield successful redshifts, but some are lost within the atmospheric emission or absorption lines, a few are at $z \geq 2.5$, and there is a small number of faint blue nearby objects (lower-left corner) for which we cannot detect [O II]. Note that the line ratio ($F_{3726} : F_{3729}$) and effective radius are re-computed for each galaxy in the COSMOS Mock Catalog, and hence the sensitivity curve drawn does not correspond to an exact boundary between detections and non-detections.

i colors. The ELGs in the redshift range $0.8 \lesssim z \lesssim 2.4$ are primarily selected from the color cut $-0.1 < g - r < 0.3$, and the g -magnitude cut gives preference to bright objects while reducing low-redshift contamination, as can be seen in Fig. 3. The condition on $r - i$ for fainter magnitudes is designed to tilt the redshift distribution in favor of more objects at $z > 1$. We can further divide the targets into a “bright subsample” ($g \leq 23.9$) and a “faint subsample” ($g > 23.9$), with the brighter targets prioritized when we wish to increase the success rate.

In the COSMOS Mock Catalog there are 7847 target galaxies available per PFS field-of-view (1.098 deg^2 for the 1.3° FoV diameter). Hence there are a sufficient number of target galaxies compared to the number of fibers ($N=2400$) for the baseline design. The green-solid curve in Fig. 4 shows the redshift dependence of [O II] flux with $S/N \geq 8.5$ for a 15 minutes exposure. To estimate the expected S/N for each galaxy, we employed the same method used in Fig. 2 and also used the galaxy size information and [O II] doublet ratio available from the COSMOS mock catalog.

Assuming 2400 fibers in the focal plane as in Table 1 and using the results in Fig. 3, we can estimate a success rate of finding [O II] emission-line galaxies among the target galaxies. We show the redshift and [O II] flux distributions of the targets in Fig. 4, and the redshift histogram of the successful [O II] detections in Fig. 5. Of the targets, 74% have successful [O II] detections, 6% are faint blue local ($z \leq 0.3$) objects, 6% fail due to an [O II] feature that falls off the red end of the spectrograph, and the remaining 14% fail due to some combination of too faint [O II] feature or overlap with an atmospheric emission or absorption complex. To have a sufficiently dense sampling of galaxies to trace large-scale structures in each redshift slice, we will need multiple visits of each field; our BAO forecasts found that 2 visits gave the best constraints.

To obtain a reliable estimate of the number of observable targets, we took into account the fiber allocation efficiency assuming a Poisson distribution of target galaxies on the sky, which should be a good approximation for a given wide redshift coverage. We conservatively assume non-overlapping patrol zones between the different fibers.¹⁶ The fiber assign-

¹⁶ That is, we allow a galaxy only to be observed by the nearest fiber, even though 21% of galaxies are in overlaps and could potentially be observed by either of two fibers.

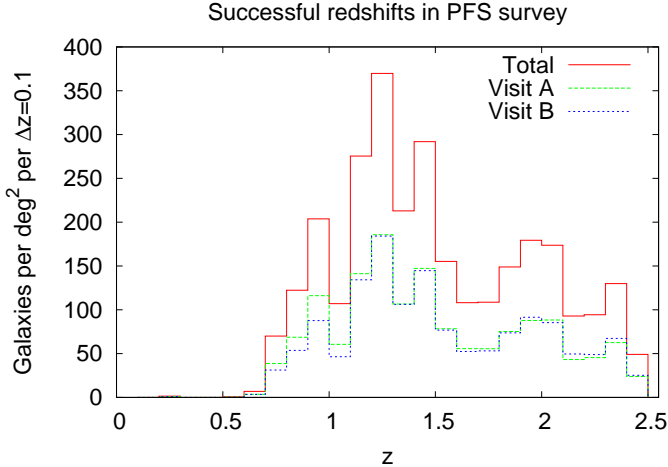


FIG. 5.— The distribution of successful redshifts ([O II] detected at $S/N > 8.5$) for the proposed PFS cosmology survey, including breakdown into the two visits. The jagged features in the curves reflect the effect of sampling variance of large-scale structures in the COSMOS field due to the finite survey area (the mock is based on the data of 1.24 square degrees). We refer to the two visits as “Visit A” and “Visit B” (see text for details), respectively, where we preferentially select brighter targets with $g < 23.9$ in Visit A in order to have some flexibility between dark/grey nights.

ment algorithm is designed to put the easier, i.e. brighter, targets in one of the visits (“Visit A”) and then the harder targets that require better conditions in another (“Visit B”). We divide our targets into two tiers – the bright ($g \leq 23.9$) and faint ($g > 23.9$) subsamples. The fiber assignment logic within each patrol zone is then:

- If at least two bright targets are available, one is assigned to Visit A and another to Visit B.
- If one bright target and at least one faint target are available, then the bright target is observed in Visit A and one of the faint targets is observed in Visit B.
- If one bright target and no faint targets are available, then the bright target is observed in Visit A and the fiber becomes a sky fiber in Visit B.
- If more than two bright targets, although unlikely, are available, then the brightest target is observed in Visit A and the next brightest target is observed in Visit B.
- If no bright targets are available and there are at least two faint targets, then a faint target is observed in both Visits A and B.
- If no bright targets are available and there is only one faint target, then the fiber becomes a sky fiber in Visit A and the faint target is observed in Visit B.
- If no targets are available, then the fiber is a sky fiber in both Visits A and B.

This algorithm produces a roughly balanced fraction of sky fibers in the two visits. The predicted allocations of the fibers are:

- Visit A: 85% bright targets, 6% faint targets, 9% sky.
- Visit B: 56% bright targets, 33% faint targets, 11% sky.

Thus this leaves about 240 sky fibers in each visit for calibrating the sky spectrum.

Note that the two visits could be scheduled in either order. Since Visit A has the brighter targets, it can achieve a high success fraction under worse conditions than Visit B. We have therefore assumed that Visit B takes place during dark time, whereas Visit A is scheduled on a night of 7 days from the New Moon (but at least 45° away from the moon). The exposure times in both cases are kept at 2×450 sec. The predicted redshift success rate for a $S/N > 8.5$ threshold is 75% (Visit A)¹⁷ or 73% (Visit B).

An alternative to the baseline (using gray time for Visit A) would be to use dark time only for the cosmology survey, and shorten the exposure time for Visit A, thereby reducing the total number of nights required but using time that may be in high demand by other programs. This trade will be made when we design an integrated observing schedule for PFS.

2.2.3. Survey Strategy

Using the results of target selection in Fig. 5, we have adopted parameters for the PFS cosmology survey summarized in Table 2. Since our primary observable is the galaxy two-point correlation function or the galaxy power spectrum, the key factors that govern the results are the geometrical volume surveyed and the ratio of clustering power to shot noise, $\bar{n}_g P_g$. To have a galaxy power spectrum measurement that reaches the sampling variance limit for our volume and is not degraded by shot noise, the number density of galaxies must satisfy $\bar{n}_g P_g \gtrsim 1$ at BAO scales. As given by the columns of Table 2, the PFS survey we are proposing has $\bar{n}_g P_g \gtrsim$ a few and slightly less than 1 at $k = 0.1$ and $0.2 h/\text{Mpc}$, respectively, over the entire target redshift range. With only one visit per field, these numbers are about a factor 2 smaller than in Table 2. On the other hand, if we have more than two visits, the survey area we can cover for a given number of nights becomes smaller. Incorporating multiple visits ensures more flexibility in optimizing the survey, for example in including a mixture of targets in different magnitude ranges.

We have assumed that the bias factor for the ELGs is given by $b_g(z) = 0.9 + 0.4z$. This specific function was a fit to semi-analytic models (Orsi et al. 2010), but compares very well to real data: e.g. the DEEP2 “main blue” sample has a measured bias of $b_g = 1.28 \pm 0.04$ at $z = 0.9$ (Coil et al. 2008).¹⁸ We have much less information about clustering of ELGs at redshifts beyond the DEEP2 survey, but H α emitters at $z = 2.23$ have a correlation length of $r_0 = 3.1 \pm 0.7 \text{ Mpc}/h$ (Sobral et al. 2010), implying a bias of $b_g = 1.87^{+0.24}_{-0.26}$.

The power spectrum measurement accuracy depends also on the area coverage. In order for the PFS survey to have a constraining power on cosmological parameters comparable with the existing or planned BAO surveys, we need a sufficiently large area coverage. We have found that, if about 100 clear nights are allocated to the PFS cosmology survey, it can meet our scientific goals. Hence we assume 100 clear nights for the following analysis, and the total area covered is estimated as

$$\frac{100 \text{ [nights]} \times 8 \text{ [hours]} \times 60 \text{ [min]}}{2 \text{ [visits]} \times (15 \text{ [min]} + 3 \text{ [min]})} \times 1.098 \text{ [sq. degrees per FoV]} = 1464 \text{ sq. degrees}(2)$$

¹⁷ This would rise to 79% if Visit A were during dark time.

¹⁸ This was normalized to a $\sigma_8 = 0.9$ model; with the lower σ_8 now favored, the bias would be higher, i.e. “better” for the BAO analysis.

TABLE 2
PFS COSMOLOGY SURVEY PARAMETERS

redshift	V_{survey} [Gpc/h] ³	N_g per field	\bar{n}_g [10 ⁻⁴ (h/Mpc) ³]	bias b_g	$\bar{n}_g P_g(k)$ $k = 0.1 h/\text{Mpc}$	$\bar{n}_g P_g(k)$ $k = 0.2 h/\text{Mpc}$
0.6 < z < 0.8	0.59	85	1.9	1.18	0.74	0.25
0.8 < z < 1.0	0.79	358	6.0	1.26	2.23	0.74
1.0 < z < 1.2	0.96	420	5.8	1.34	2.10	0.68
1.2 < z < 1.4	1.09	640	7.8	1.42	2.64	0.87
1.4 < z < 1.6	1.19	491	5.5	1.50	1.78	0.59
1.6 < z < 2.0	2.58	598	3.1	1.62	0.95	0.31
2.0 < z < 2.4	2.71	539	2.7	1.78	0.76	0.25

NOTE. — The leftmost column shows the redshift range of each slice, and the other columns show the comoving volume (V), the number of [OII] galaxies per field (N_g), the mean comoving number density (\bar{n}_g), the linear bias parameter (b_g) and the values of $\bar{n}_g P_g(k)$ at $k = 0.1$ and $0.2 h/\text{Mpc}$ for each slice, respectively. The survey volume is for a survey area of 1464 square degrees, which is estimated assuming 15 min of open-shutter time per visit, 2 visits per field, 3 min overhead per visit, and 100 clear nights. For comparison, the BOSS BAO survey has the survey parameters: 10000 sq. degrees area coverage over $0.4 < z < 0.7$, $V_{\text{survey}} = 4.4 (\text{Gpc}/h)^3$, $\bar{n}_g = 3 \times 10^{-4} (h/\text{Mpc})^3$, $b_g = 2.3$ and $\bar{n}_g P_g(k = 0.1 h/\text{Mpc}) \simeq 5$.

Here we conservatively assumed 3min overhead for each new pointing, which covers readout, slewing and the time for accurate fiber positioning, and assumed that 8 hours per night are available for observation on source. The comoving volume in each redshift slice is given in Table 2. The total volume is about $9.3 (\text{Gpc}/h)^3$, a factor 2 larger volume than the SDSS BOSS galaxy survey, which is about $4.4 (\text{Gpc}/h)^3$. A notable strength of the PFS survey is that it probes large-scale structure in higher redshifts, where the fluctuations are largely in the linear regime and therefore allow a cleaner estimation of cosmological parameters. In fact the genuine cosmological power comes from the volume in Fourier space; the effective volume at each wavenumber is given as $V_{\text{eff}}(k) = [\bar{n}_g P_g(k)/(1 + \bar{n}_g P_g(k))]^2 V_{\text{survey}}$, where V_{survey} is the comoving volume. The total number of the Fourier modes usable for constraining cosmology is estimated by integrating the effective volume in Fourier space up to the maximum wavenumber k_{max} which is determined such that the theoretical model to be compared with the measurement is reliable up to k_{max} . The larger the redshift, the higher the wavenumber we can use, because the nonlinear scale becomes smaller (higher k). Hence, the proposed PFS survey offers much more than a factor 2 improvement compared to the BOSS constraint (e.g., Anderson et al. 2012). Although Table 2 also gives estimates for the lower redshift slice $0.6 < z < 0.8$, which partially overlaps the ongoing BOSS and WiggleZ surveys, the cosmological constraining power of this slice is not as great due to the smaller areal coverage and reduced galaxy number density. However, we consider it important to retain this redshift slice as it can give a useful benchmark in comparison with other surveys such as the BOSS and WiggleZ surveys, particularly for calibrating systematic issues.

2.2.4. Expected cosmological constraints

We now can estimate the power of the PFS cosmology survey in Table 2 for constraining cosmological parameters. To ensure a fair comparison with other surveys, we primarily assess the power of PFS survey in terms of its BAO geometrical constraints.

Geometrical constraints:

The galaxy two-point correlation function is measured as a function of the separation between paired galaxies. The position of each galaxy needs to be inferred from the measured

redshift and angular position. Then the separation lengths perpendicular and parallel to the line-of-sight direction from the measured quantities are given as $r_{\perp} \propto \Delta\theta$ and $r_{\parallel} \propto \Delta z$, where $\Delta\theta$ and Δz are the differences between the angular positions and the redshifts of the paired galaxies. For this conversion, we need to assume a reference cosmological model to relate the observables ($\Delta\theta$, Δz) to the quantities (r_{\perp} , r_{\parallel}). Thus, the wavenumbers are given as

$$k_{\perp,\text{ref}} = \frac{D_A(z)}{D_{A,\text{ref}}(z)} k_{\perp}, \quad k_{\parallel,\text{ref}} = \frac{H_{\text{ref}}(z)}{H(z)} k_{\parallel}. \quad (3)$$

The quantities with subscript ‘‘ref’’ are the quantities estimated from the observables assuming a ‘‘reference’’ cosmological model, and the quantities without the subscript are the underlying true values. Since the reference cosmological model assumed generally differs from the underlying true cosmology, it causes an apparent distortion in the two-dimensional pattern of galaxy clustering. In principle, the distortion could be measured using only the anisotropy of clustering statistics (Alcock & Paczynski 1979), but a more robust measurement can be obtained using features in the power spectrum, particularly if they are at a known scale so that we can measure both $D_A(z)$ and $H(z)$. In particular, the CMB-inferred BAO scale of 150 Mpc gives a powerful standard ruler for this geometrical test (Eisenstein et al. 2005; Percival et al. 2007; Blake et al. 2011; Hu & Haiman 2003; Seo & Eisenstein 2003).

The use of this scale without edge effects in a survey field requires the survey to be contiguous on a scale large compared to the BAO length; at our minimum redshift ($z = 0.8$), 2.5 BAO lengths corresponds to 7.5 degrees on the sky, so we set this as our minimum width. This requirement will be refined further by simulations.

In more detail, the galaxy power spectrum in redshift space is given in the linear regime as

$$P_{g,s}(k_{\perp,\text{ref}}, k_{\parallel,\text{ref}}; z) = \frac{D_{A,\text{ref}}(z)^2 H(z)}{H_{\text{ref}}(z) D_A(z)^2} \left[1 + \beta(z) \frac{k_{\parallel}^2}{k^2} \right]^2 \times b_g^2 P_m^L(k; z) + P_{\text{sn}}, \quad (4)$$

where b_g is the linear bias parameter, β is the linear redshift-space distortion (RSD) parameter, defined as $\beta \equiv (1/b_g) d \ln D / d \ln a|_z$ (Kaiser 1987), D is the linear growth

rate, P_m^L is the linear mass power spectrum, and P_{sn} is a parameter to model the residual shot noise. We can use the BAO features in the linear power spectrum P_m^L as a standard ruler in order to constrain $D_A(z)$ and $H(z)$. The BAO constraints are relatively robust against the galaxy bias uncertainty and the other nonlinearity effects, because none of the systematic effects introduces any particular length scale comparable with the BAO scale. Further, if we can use the shape and amplitude information in the galaxy power spectrum, we can constrain the growth rate as well as other cosmological parameters such as the neutrino mass and the primordial power spectrum parameters (Takada et al. 2006), as we will discuss below.

To make the parameter forecast, we have used the method developed in Seo & Eisenstein (2007). In this method, we include the smearing effect of the BAO features due to the bulk flow of galaxies in large-scale structure (Matsubara 2008; Taruya et al. 2009; Nishimichi & Taruya 2011). For the BAO survey of multiple redshift bins, the Fisher information matrix of model parameters can be computed as

$$F_{\alpha\beta} = \sum_{z_i} \int_{-1}^1 d\mu \int_{k_{\text{min}}}^{k_{\text{max}}} \frac{2\pi k^2 dk}{2(2\pi)^3} \frac{\partial \ln P_{g,s}(k, \mu; z_i)}{\partial p_\alpha} \times \frac{\partial \ln P_{g,s}(k, \mu; z_i)}{\partial p_\beta} V_{\text{eff}}(k; z_i) \times \exp \left[-k^2 \Sigma_\perp^2 - k^2 \mu^2 (\Sigma_\parallel^2 - \Sigma_\perp^2) \right], \quad (5)$$

where μ is the cosine between the wavevector and the line-of-sight direction, $\mu \equiv k_\parallel/k$; \sum_{z_i} is the sum over different redshift bins; $\partial P_{g,s}/\partial p_\alpha$ is the partial derivative of the galaxy power spectrum (Eq. 4) with respect to the α -th parameter around the fiducial cosmological model; the effective survey volume V_{eff} and the Lagrangian displacement fields Σ_\parallel and Σ_\perp to model the smearing effect are given as

$$V_{\text{eff}}(k, \mu; z_i) \equiv \left[\frac{\bar{n}_g(z_i) P_{g,s}(k, \mu; z_i)}{\bar{n}_g(z_i) P_{g,s}(k, \mu; z_i) + 1} \right]^2 V_{\text{survey}}(z_i) \quad (6)$$

$$\Sigma_\perp(z) \equiv c_{\text{rec}} D(z) \Sigma_0, \quad (7)$$

$$\Sigma_\parallel(z) \equiv c_{\text{rec}} D(z) (1 + f_g) \Sigma_0. \quad (8)$$

Here $V_{\text{survey}}(z_i)$ is the comoving volume of the redshift slice centered at z_i ; the present-day Lagrangian displacement field is $\Sigma_0 = 11h^{-1}\text{Mpc}$ for $\sigma_8 = 0.8$ (Eisenstein et al. 2007); $D(z)$ is the growth rate normalized as $D(z=0) = 1$; $f_g = d \ln D / d \ln a$. The parameter c_{rec} is a parameter to model the reconstruction method of the BAO peaks (see below). In Eq. (5), we take the exponential factor of the smearing effect outside of the derivatives of $P_{g,s}$. This is equivalent to marginalizing over uncertainties in Σ_\parallel and Σ_\perp . The growth rate in Σ_\parallel or Σ_\perp takes into account the smaller smearing effect at higher redshift due to the less evolved large-scale structure. For the parameters, we included the cosmological parameters, the distances in each redshift slice, and the nuisance parameters:

$$p_\alpha = \{ \Omega_{\text{m}0}, A_s, n_s, \alpha_s, \Omega_{\text{m}0} h^2, \Omega_{\text{b}0} h^2, D_A(z_i), H(z_i), b_g(z_i), \beta(z_i), P_{\text{sn}}(z_i) \}, \quad (9)$$

where A_s , n_s and α_s are parameters of the primordial power spectrum; A_s is the amplitude of the primordial curvature perturbation, and n_s and α_s are the spectral tilt and the running spectral index. The set of cosmological parameters determines the shape of the linear power spectrum. By using

the method above, we can estimate the cosmological distance information solely from the BAO peaks, including marginalization over modeling uncertainties in the broad-band shape of the power spectrum. For the k -integration, we set $k_{\text{min}} = 10^{-4} h/\text{Mpc}$ and $k_{\text{max}} = 0.5 h/\text{Mpc}$ for all the redshift slices, but the exponential factor in Eq. (5) suppresses the information from the nonlinear scales. The Fisher parameter forecasts depend on the fiducial cosmological model, for which we assumed the model consistent with the WMAP 7-year data (Komatsu et al. 2011).

Further, we assume that we can implement the promising method of Eisenstein et al. (2007) for improving the BAO measurements. Since the peculiar velocity field of galaxies in large-scale structure can be inferred from the measured galaxy distribution, the inferred velocity field allows us to pull back each galaxy to its position at an earlier epoch and then reconstructing the galaxy distribution more in the linear regime. As a result, one can correct to some extent the smearing effect in Eq. (5) and sharpen the BAO peaks in the galaxy power spectrum. Recently, Padmanabhan et al. (2012) implemented this method with real data from the SDSS DR7 LRG catalog, and showed that the reconstruction method can improve the distance error in the BAO scale by a factor of 2. The improvement was equivalent to reducing the nonlinear smoothing scale from 8.1 to $\Sigma_{\text{nl}} = 4.4 h^{-1}\text{Mpc}$, about a factor 2 reduction in the displacement field. To implement this reconstruction method requires a sufficiently high number density of the sampled galaxies in order to reliably infer the peculiar velocity field from the measured galaxy distribution. Each redshift slice of the PFS survey (see Table 2) satisfies the requirement; the number density of galaxies in each redshift slice is higher than that of both the SDSS DR7 LRGs ($\bar{n} \simeq 10^{-4} (h/\text{Mpc})^3$) and the BOSS LRGs ($\bar{n} \simeq 3 \times 10^{-4} (h/\text{Mpc})^3$). Hence we can safely assume that the reconstruction method can be applied to the PFS BAO experiment. In the Fisher matrix calculation, we used $c_{\text{rec}} = 0.5$ for an implementation of the reconstruction method¹⁹.

Finally, we have used the CMB information expected from the Planck satellite experiment (Planck 2013 Results XVI 2013), which gives a precise constraint on the sound horizon scale in order for us to use the BAO scale as a standard ruler. In addition to the cosmological parameters ($\Omega_{\text{m}0}, A_s, n_s, \alpha_s, \Omega_{\text{m}0} h^2, \Omega_{\text{b}0} h^2$), we included, in the CMB Fisher matrix, τ (the optical depth to the last scattering surface) and $D_A(z_{\text{CMB}})$ (the angular diameter distance to the last scattering surface). Then we can compute the Fisher matrix for the BAO experiment by adding the galaxy and CMB Fisher matrices; $F_{\alpha'\beta'} = F_{\alpha'\beta'}^{\text{galaxy}} + F_{\alpha'\beta'}^{\text{Planck}}$. The dimension of the Fisher matrix for the PFS survey in combination with the Planck information is 38×38 (see Eq. 9). When further combined with the SDSS and BOSS BAO information (Eisenstein et al. 2005; Anderson et al. 2012), the dimension of the Fisher matrix increases accordingly.

Fig. 6 shows the expected accuracies of determining the angular diameter distance and the Hubble expansion rate in each redshift slice with the PFS cosmology survey (Table 2). The errors include marginalization over uncertainties of other parameters. The PFS forecasts can be compared with the accuracies of the existing and ongoing SDSS/BOSS surveys. As can be clearly seen, the PFS cosmology survey can constrain

¹⁹ With these assumptions, we found we can roughly reproduce the distance measurement accuracy for the SDSS LRGs as found in Padmanabhan et al. (2012).

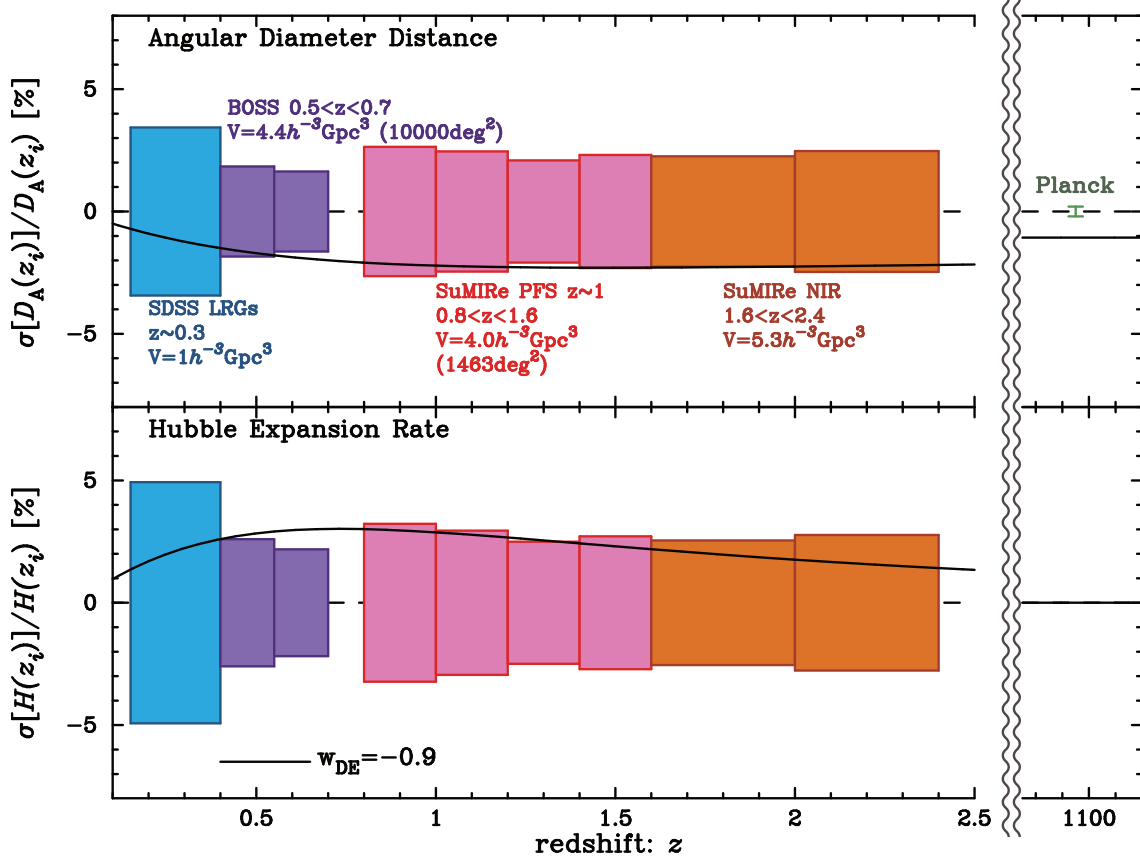


FIG. 6.— Fractional errors in the angular diameter distance and the Hubble expansion rate via the PFS BAO experiment (see Table 2) including marginalization over uncertainties of other parameters. The expected accuracies are compared to the existing and ongoing SDSS and BOSS surveys. The PFS survey will provide geometrical constraints to higher redshift than the SDSS and BOSS surveys, but with comparable precision. The solid curve in each panel shows the fractional difference when changing the dark energy equation of state parameter from the fiducial model $w = -1$ to $w = -0.9$.

$D_A(z)$ and $H(z)$ over a wider range of redshift, yet with similar precision to, the SDSS and BOSS surveys. Even though the PFS area coverage is smaller than that of SDSS or BOSS surveys by a factor of 7 (1400 vs. 10000 sq. degrees), the PFS survey covers a factor 10 and 2 times larger comoving volume than the SDSS and BOSS surveys, respectively.

Cosmological implications:

It is worth noting that the BOSS survey will measure the clustering statistics of the Lyman- α forest over $2.1 \lesssim z \lesssim 3.4$ (Slosar et al. 2013). PFS thus serves to fill a natural ‘gap’ in-between the galaxy and Lyman- α BAO experiments, allowing us to probe the expansion history over the entire range of redshifts, $0 \lesssim z \lesssim 3$, i.e. through the period where it is believed that the cosmic expansion went from decelerated to accelerated phases. If we model the expansion history as parametrized by the dark energy model (w_0, w_a) (Linder 2003) and the curvature parameter (K),

$$H^2(z) = H_0^2 \left[\Omega_{m0}(1+z)^3 - \frac{K}{H_0^2}(1+z)^2 + \Omega_{de,0} a^{-3(1+w_0+w_a)} e^{3w_a(a-1)} \right], \quad (10)$$

we can propagate the distance measurement errors into the accuracies of estimating the parameters. To be more explicit, we can do this, based on the Fisher information matrix formalism, by projecting the BAO Fisher matrix onto different

parameter space:

$$F_{a'b'} \equiv \frac{\partial \tilde{p}_a}{\partial p_{a'}} F_{ab}^{\text{sub}} \frac{\partial \tilde{p}_b}{\partial p_{b'}}. \quad (11)$$

Here the new set of parameters $\tilde{p}_{a'}$ is given as $\tilde{p}_{a'} = (\Omega_{de0}, \Omega_{m0}h^2, \Omega_K, w_0, w_a)$, which specifies the cosmic expansion history given by the above equation, and F_{ab}^{sub} is the sub-matrix computed by inverting the sub-matrix of the inverse of the full BAO matrix, $[F^{-1}]_{\alpha\beta}$, containing only the parts of the geometrical parameters, $p_a = \{\Omega_{m0}, \Omega_{m0}h^2, D_A(z_i), H(z_i)\}$. Hence the derived constraints on $\tilde{p}_{a'}$ include marginalization over other parameters such as the galaxy bias and the β parameters. Table 3 shows the expected accuracies of the dark energy parameters and the curvature parameter for the PFS survey. Here w_{pivot} is the dark energy equation state at the ‘pivot’ redshift, at which the dark energy equation of state is best constrained for a given survey. The quantity FoM_{de} is the dark energy figure-of-merit defined in the Dark Energy Task Force Report (Albrecht et al. 2006), which quantifies the ability of a given survey to constrain both w_0 and w_a ; $\text{FoM}_{de} \equiv 1/[\sigma(w_{\text{pivot}})\sigma(w_a)]$, which is proportional to the area of the marginalized constraint ellipse in a sub-space of (w_0, w_a) . Table 3 clearly shows that the PFS BAO can significantly tighten the parameter constraints over the SDSS and BOSS surveys. Most interestingly, the PFS has the potential to constrain the curvature parameter to a precision of 0.3%. If we can detect a non-zero curvature,

this would represent a *fundamental discovery* giving critical constraint into the physics of the early universe, for example insight into different inflation scenarios (Efstathiou 2003; Contaldi et al. 2003; Freivogel et al. 2006; Kleban & Schillo 2012; Guth & Nomura 2012).

Nature of dark energy:

The parametrization (w_0, w_a) adopted for the dark energy equation of state samples only a narrow range of dark energy models. Given that there is no well-accepted model for dark energy we seek to interpret our PFS data in a more model-independent way. The wide redshift coverage of the PFS survey, in combination with the SDSS and BOSS surveys, allows us to do this by directly reconstructing the dark energy density as a function of redshift solely based on the geometrical BAO constraints. To illustrate this, we use the Hubble expansion history parametrized in terms of dark energy density parameters in each redshift bins:

$$H^2(z) = H_0^2 \left[\Omega_{m0}(1+z)^3 - \frac{K}{H_0^2}(1+z)^2 + \frac{\rho_{de,z_i}(z \in z_i)}{\rho_{cr0}} \right], \quad (12)$$

where ρ_{de,z_i} is the dark energy parameter in the redshift bin centered at z_i . For the combined BAO survey of SDSS, BOSS and PFS, we include the 9 dark energy densities, $\rho_{de}(z_i)$, given in 9 redshift bins (8 redshift bins of the galaxy surveys plus the redshift bin from 2.4 to z_{CMB}). Then, similarly to the method described around Eq. (11), we can propagate the BAO-measured distance errors into the accuracies of reconstructing the dark energy densities in each redshift bin. Fig. 7 shows the result, where we assumed the cosmological constant, $\rho_{de} = \text{constant}$, as the fiducial model. The figure clearly shows that the PFS BAO survey is capable of reconstructing dark energy densities up to high redshift, $z \simeq 2$ for a model in which $\rho_{de}(z) \simeq \text{constant}$, thereby testing various types of early dark energy models. For comparison, the dashed curve shows the dark energy density parameter for an early dark energy (EDE) model proposed in Doran & Robbers (2006), which gives a more significant contribution to the cosmic expansion at higher redshift than in the cosmological constant:

$$\Omega_{de}^{\text{EDE}}(a) = \frac{\Omega_{de0} - \Omega_e(1 - a^{-3w_0})}{\Omega_{de0} + \Omega_{m0}a^{3w_0}} + \Omega_e(1 - a^{-3w_0}), \quad (13)$$

where we fixed the parameters to $\Omega_e = 0.05$ and $w_0 = -1$ as the fiducial model. Note that we set the present-day energy density of EDE to be the same as that of the cosmological constant model. The figure clearly shows that PFS can put a more stringent constraint on such an early-dark energy model thanks to its wide redshift coverage, e.g. compared to the BOSS alone. To be more precise, the combined BOSS and PFS geometrical constraints can achieve a precision of $\sigma(\Omega_e) = 0.048$ even under the conservative setup of our forecasts, while the BOSS alone cannot constrain the parameter well ($\sigma(\Omega_e) = 1.2$).

Further, we should emphasize that adding the PFS BAO measurements to the SDSS and BOSS information can significantly improve the reconstruction of dark energy density at low redshift, partly because the SDSS+BOSS BAO alone cannot break degeneracies between parameters $(\Omega_{m0}, \Omega_{b0}, K, \rho_{de}(z_i))$ given the distance measurements to the three redshifts ($z_{\text{SDSS}}, z_{\text{BOSS}}, z_{\text{CMB}}$), and also because the angular diameter distances for the PFS redshifts are all sensitive to dark energy densities at low redshift via the inte-

gration relation between the angular diameter distance and the Hubble expansion rate. However, we should note that the constraint on the curvature parameter is significantly degraded in this case to $\sigma(\Omega_K) = 0.057$ from the result in Table 3 because of the larger number of free parameters. Thus the accuracy of the curvature parameter is sensitive to which dark energy model we use for marginalization.

Testing the growth of structure:

We now turn to the utility of measuring the *redshift-space distortion (RSD) effect* and the broad-band shape of the galaxy power spectrum. If we can reliably model the RSD and the shape of the power spectrum in the weakly nonlinear regime including a possible scale-dependent bias, we can use this information not only to improve the cosmological constraints (Takada et al. 2006), but also to constrain the growth rate which is sensitive to the theory of gravity on cosmological scales. Encouraging progress is being made via many efforts to develop a more accurate model of the redshift-space power spectrum in the weakly nonlinear regime as we discuss below. (Matsubara 2008; Taruya et al. 2009; Nishimichi & Taruya 2011; Tang et al. 2011; Hikage et al. 2012a,b).

To estimate the power of the PFS survey, we use the linear theory prediction for the amplitude of the RSD effect, $\beta(z) = f_g(z)/b_g(z)$, in Eq. (4), where f_g is defined by the growth rate as $f_g \equiv d \ln D / d \ln a$. Then we can include the RSD effect in the Fisher matrix formalism by using f_g in each redshift slice instead of treating β as parameters (see Eqs. 4 – 9). With this implementation, we can break degeneracies between the RSD effect f_g/b_g and the galaxy bias uncertainty b_g from the measured anisotropic modulations in the redshift-space galaxy power spectrum. Then we can in turn use the amplitude and shape information of the underlying linear power spectrum.

Fig. 8 shows the expected accuracies of constraining the growth rate, $f_g (= d \ln D / d \ln a)$, in each redshift slice via the RSD measurements. The PFS survey can constrain the growth rate in each redshift to a 6% accuracy. In particular, PFS will provide accurate constraints on the growth rate at redshifts beyond $z = 1$, when the cosmic expansion is in its decelerated phase. Such constraint are very important for testing whether dark energy is an illusion caused by an incomplete understanding of General Relativity.

Other constraints:

With the growth rate constraints and the information on the shape of the galaxy power spectrum, we can also constrain other interesting parameters, such as the sum of neutrino masses ($m_{\nu, \text{tot}}$) and the degree of primordial non-Gaussianity (f_{NL}). Primordial non-Gaussianity induces a characteristic scale-dependent biasing effect on the galaxy distribution at very large scales (Dalal et al. 2008) that are well in the linear regime and cannot be explained by other nonlinearity effects. Hence we can use the largest-scale signal of galaxy clustering to explore the signature of the primordial non-Gaussianity. Table 3 shows the expected accuracy of constraining f_{NL} to an accuracy of $\sigma(f_{\text{NL}}) \simeq 11$ if systematic errors are under control (see below for discussion on possible systematic errors). The Planck experiment showed a more stringent upper limit on f_{NL} such as $f_{\text{NL}} \lesssim 5$ (68% C.L.) (Planck 2013 Results XXIV 2013); PFS is limited by its relatively small area coverage to access the largest-length scales.

On the other hand, the massive neutrinos, as found by terrestrial experiments, suppress the galaxy clustering power on scales smaller than the neutrino free-streaming scale, which

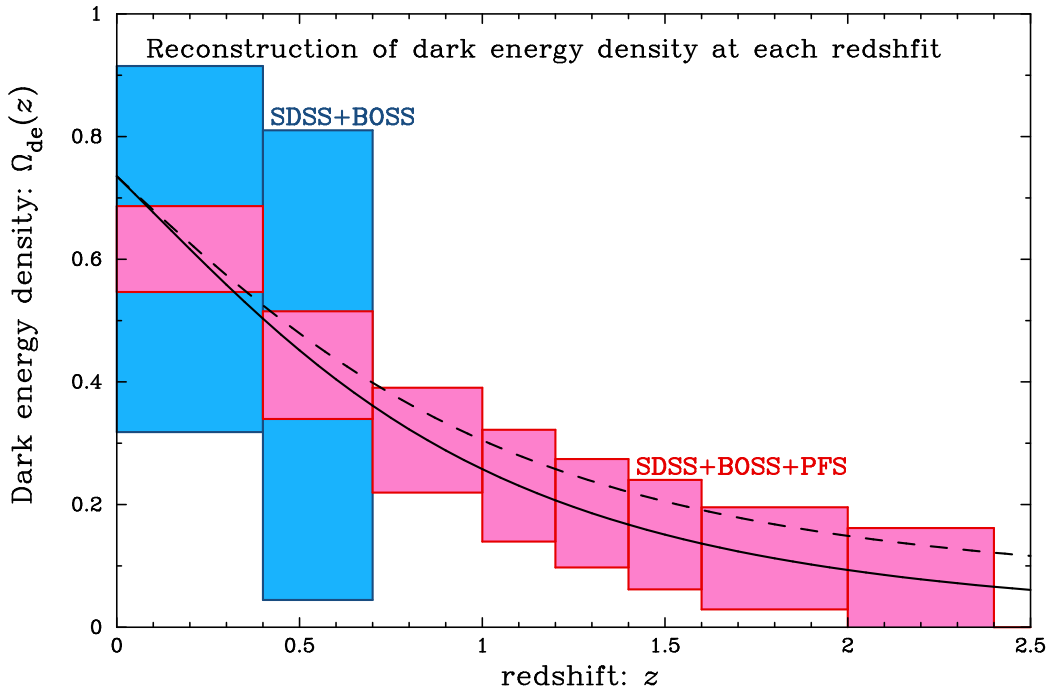


FIG. 7. — Expected accuracy of reconstructing the dark energy density parameter at each redshift, $\Omega_{\text{de}}(z) \equiv \rho_{\text{de}}(z)/[3H^2(z)/8\pi G]$ from the BAO-measured $D_A(z)$ and $H(z)$ in Fig. 6. Here we considered the cosmological constant ($\rho_{\text{de}}(z) = \rho_{\text{de}0} = \text{constant}$) and the flat universe ($\Omega_K = 0$) as the fiducial model. Adding the PFS BAO constraints to the SDSS and BOSS constraints enables reconstruction of the dark energy density to $z \simeq 2$, and also significantly improves the precision at low redshifts, as the comoving distance at the high redshift arises from an integration of $H(z)$. The solid curve shows the energy density parameter for the fiducial Λ CDM model, while the dashed curve shows the redshift evolution for an early dark energy model in Droan & Robbers (2006), where we employed $w_0 = -1$ and $\Omega_{\text{de}}^0 = 0.05$ for the model parameters (see text for details).

TABLE 3
FORECASTED ACCURACIES OF COSMOLOGICAL PARAMETERS

Survey	$\Omega_{\text{de}0}$	w_{pivot}	w_a	FoM _{de}	Ω_K	$m_{\nu,\text{tot}}$ [eV]	f_{NL}
SDSS+BOSS	0.0061	0.076	1.2	11	0.0071	0.188	16
SDSS+BOSS+PFS	0.0051	0.059	0.36	47	0.0030	0.133	11

NOTE. — The constraints on $\Omega_{\text{de}0}$, w_{pivot} , w_a and $\Omega_K (\equiv -K/H_0^2)$ are from the BAO distance measurements in Fig. 6, i.e. not including the information on the broadband shape of the galaxy power spectrum. Note that w_{pivot} is the dark energy equation state at the “pivot” redshift, at which the dark energy equation state parameter is best constrained for the given PFS BAO measurements. The constraints on the neutrino mass $m_{\nu,\text{tot}}$ and f_{NL} are derived by including the broadband shape information. See the text for details.

imprints a characteristic scale-dependent effect on the galaxy power spectrum (Takada et al. 2006). The amount of the suppression scales with the sum of neutrino mass as $\Delta P_g/P_g \simeq -8\Omega_{\nu 0}/\Omega_{\text{m}0} \simeq -8m_{\nu,\text{tot}}/(94.1 \text{ eV}\Omega_{\text{m}0}h^2)$ at the scales smaller than the neutrino free-streaming scale. Thus the neutrinos of $m_{\nu,\text{tot}} = 0.1 \text{ eV}$, close to the lower bound of the inverted neutrino mass hierarchy, lead to about 6% suppression in the galaxy power spectrum compared to the case without the massive neutrinos. Hence, we can use the measured clustering amplitude to constrain the neutrino mass. However, the achievable precision of neutrino mass depends on the level of our understanding of the nonlinear power spectrum including the galaxy bias uncertainty (Saito et al. 2008, 2009). Here, by assuming that an accurate model of the galaxy power spectrum is available, we estimate the power of PFS to constrain the neutrino mass. To be more precise, we assumed that the following set of parameters, instead of Eq. (9), can model the

redshift-space galaxy power spectrum based on the extended perturbation theory based method in combination with numerical simulations:

$$p_\alpha = \{\Omega_{\text{m}0}, A_s, n_s, \alpha_s, \Omega_{\text{m}0}h^2, \Omega_{\text{b}0}h^2, \Omega_K, w_0, w_a, m_{\nu,\text{tot}}, b_g(z_i), P_{\text{sn}}(z_i)\}. \quad (14)$$

In this parameter estimation we did not use the reconstruction method (i.e., we set $c_{\text{rec}} = 1$ for the reconstruction parameter in Eq. 8), because the reconstruction method of BAO peaks alters the shape and amplitude of the power spectrum. With this implementation, we can include the shape and amplitude information of the power spectrum for constraining the cosmological parameters, marginalized over uncertainties of the nuisance parameters. Also note that, for the parameter estimation, we included a broader range of cosmological parameters such as the curvature Ω_K and the dark energy parameters (w_0, w_a), which also cause a suppression

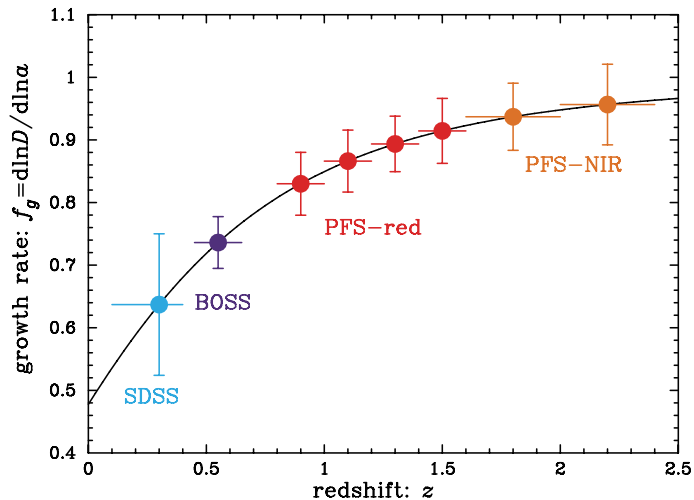


FIG. 8.— Marginalized errors in reconstructing the growth rate, $f_g \equiv d \ln D / d \ln a$, in each redshift slice.

in the growth rate of structure formation as do the massive neutrinos. However, we assumed linear bias parameters for each redshift slice, but instead included parameters to model the residual shot noise contamination, which mimic a scale-dependent bias. As can be found from Table 3, the PFS survey can achieve a precision of $\sigma(m_{\nu, \text{tot}}) \simeq 0.13$ eV. However, we again note that, even though we included marginalization over other parameters, the neutrino mass constraint is sensitive to the level of our understanding of nonlinearity effects such as nonlinear bias or nonlinear evolution of matter clustering as we will discuss below in § 2.2.5. If we restrict the parameter forecast to the power spectrum information up to $k_{\text{max}} = 0.1$ h/Mpc , where the linear theory assumption is considered to be valid, the expected constraint of neutrino masses is degraded to $\sigma(m_{\nu, \text{tot}}) \simeq 0.55$ eV. Thus an understanding of the nonlinearity effects is important to obtain a higher-precision, robust constraint on the neutrino mass.

2.2.5. Discussion of other systematic errors

There remain theoretical and observational systematic errors that may affect our PFS cosmology program. To realize the full potential of the PFS cosmology survey, we must carefully consider and account for these errors.

Uncertainty in the modeling of galaxy power spectrum:

The linear theory of structure formation is not sufficiently accurate to be compared with the measured power spectrum of galaxies even at BAO scales, given the statistical precision of the PFS cosmology survey. In other words, interpreting the the galaxy power spectrum is complicated by non-linear effects such as those relating to large scale structure and the connection between the galaxy and dark matter distributions. An advantage of the PFS cosmology survey is its focus on higher redshift; the rate of evolution in large scale structure, and hence the effect of non-linearities, is reduced at higher redshift. There are promising developments towards an accurate modeling of the galaxy power spectrum based on a suite of high-resolution simulations as well as refined perturbation theory, at BAO scales that are still in the mildly non-linear regime (Matsubara 2008; Taruya et al. 2009; Matsubara 2011; Taruya et al. 2012; Sugiyama & Futamase 2012). Fig. 9 compares the nonlinear matter power spectra computed from the refined perturbation theory and from N -body simulations

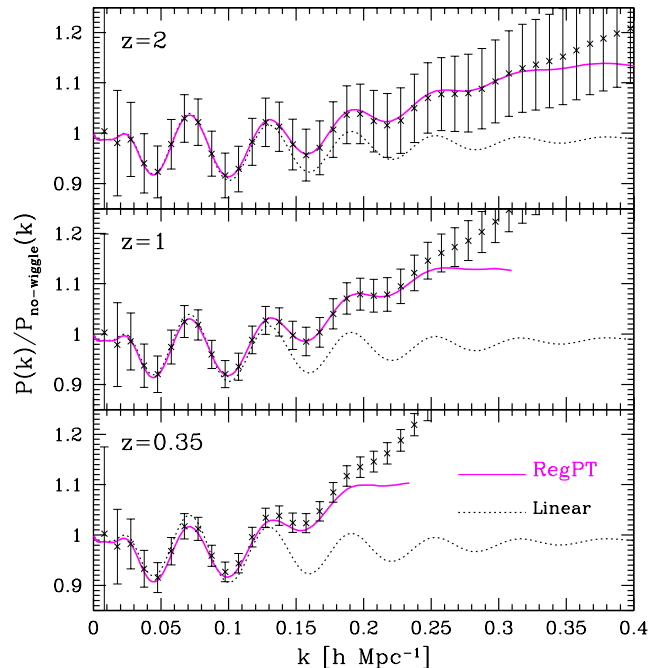


FIG. 9.— Nonlinear matter power spectra at different redshifts, $z = 0.35$, 1 and 2 in the bottom, middle and upper panels, respectively. For illustrative purposes, the power spectrum is divided by the linear power spectrum with BAO features not included. The data points with error bars in each panel are the power spectrum estimated from N -body simulations, where the error bars are the expected 1σ statistical errors of the power spectrum measurement at each k bin, assuming the survey volume of 3 $(\text{Gpc}/h)^3$ and the comoving number density of 3×10^{-4} $(h/\text{Mpc})^3$. The survey parameters roughly correspond to those for the $z = 1$ and 2 slices of the PFS cosmology survey (see Table 2). The solid curve shows the analytical prediction based on the refined perturbation theory (Taruya et al. 2012), which shows a satisfactory agreement with the simulation result, up to a higher wavenumber for higher redshift slices.

for different redshift slices, $z = 0.35$, 1 and 2 (Taruya et al. 2012). The figure clearly shows that non-linearities have a reduced effect at higher redshift and also that the refined perturbation theory provides a better match to the simulation results. A gain in the maximum wavenumber (k_{max}) up to which to include the power spectrum information for the cosmological analysis is equivalent to having a larger survey volume; a factor 2 gain in k_{max} is equivalent to a factor 8 larger survey volume in the sampling variance limited regime²⁰. Thus the PFS survey, in combination with the refined theoretical model, provides a more robust and powerful cosmological result than one based on a survey at lower redshift.

We also stress that there will be many synergistic opportunities enabled by the fact that the PFS survey will be undertaken in the same area of sky as the HSC imaging survey. Weak lensing information from HSC will be very effective in correcting and calibrating systematic effects inherent in the galaxy clustering analysis, nonlinear redshift-space distortion and the galaxy bias uncertainty, up to the $z \sim 2$ slice (Hikage et al. 2012a,b; Nishizawa et al. 2012). The spectroscopic data from the PFS survey can likewise be used to calibrate the photo- z errors and the redshift distribution of HSC imaging galaxies, which is one of the major uncertainties in the HSC cosmology analysis. Thus, by combining the HSC imaging

²⁰ The cumulative statistical precision, $(S/N)^2$, for the power spectrum measurement scales with the Fourier-space volume as $\propto k_{\text{max}}^3$.

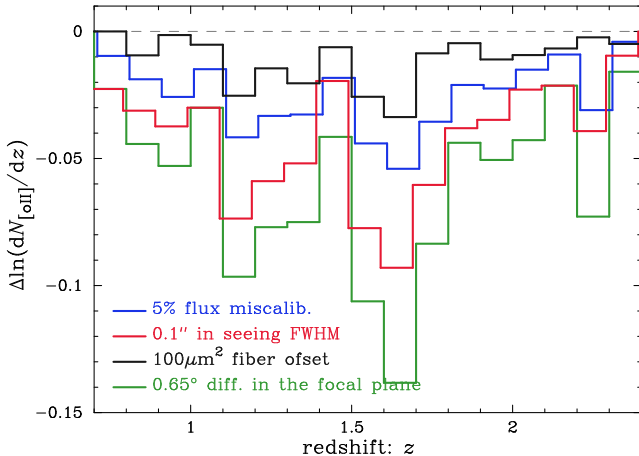


FIG. 10.— How observational systematic errors affect the selection function of the detected [O II] emission-line galaxies as a function of redshift, computed by using our exposure time calculator in combination with the COSMOS mock catalog (see Section 2.2.2). Here we assumed the fixed threshold $S/N = 8.5$ for the [O II] line detection. As for working examples, we consider the fiber positioning offset by $10 \mu\text{m}^2$ from the true centroid, misestimation of PSF FWHM by $0.1''$, and 5% error in flux calibration. For comparison, we also show the difference between the numbers of detected [O II] emitters at the center and edge (0.65 degrees in radius) of the focal plane. These observational effects change the number of detected [O II] emitters.

and PFS spectroscopic surveys, we can significantly improve the cosmological constraints, making the joint HSC and PFS experiments comparable to a Stage-IV Dark Energy experiment in the parlance of recent US studies.

Observational systematic errors:

The PFS cosmology survey relies on the use of [O II] emission-line galaxies, detected with S/N greater than a given threshold ($S/N = 8.5$ assumed throughout this document). A variety of observational factors will affect the detection efficiency of this line, causing apparent density fluctuations in the observed galaxy distribution. These include

- Offset of the fibers from its expected position, e.g. due to a systematic error in the astrometric solution and/or imperfect positioning.
- Variation in the throughput over the field angle (e.g. due to the vignetting).
- A misestimation in the seeing FWHM. The PSF misestimation causes a biased estimate of the intrinsic [O II] flux.
- A flux miscalibration such as an error in the magnitude zero point.

In Fig. 10, we use our exposure time calculator to estimate how the systematic errors mentioned above change the number of detected [O II] emitters in each redshift bin, where we employed the same threshold $S/N = 8.5$. Here we consider some typical values for each of the systematic errors as indicated by the legend. Thus, the systematic errors might alter the number of detected galaxies in each pointing, and the effects generally vary with different pointings, causing apparent density fluctuations of the detected galaxies on the sky.

Thus the systematic errors need to be well corrected in order for us not to obtain a biased constraint on the growth rate or cosmological parameters from the measured power spectrum

amplitudes. A calibration of the systematic errors requires an adequate strategy of the PFS cosmology survey; e.g., frequent observations of standard stars, and a large-angle dithering (tiling) offset between different pointings. In particular, we are planning to use, for the calibration, the sample of [O II] emission-line galaxies taken from the PFS galaxy survey (see Section 4 for details). With its much deeper depth and much higher completeness in the PFS galaxy survey, the sample allows us to understand intrinsic properties of [O II] emission-line galaxies such as the luminosity function, the line width and the line ratio of [O II] doublet. We will in turn use the calibration sample of [O II] emitters in the PFS galaxy survey to estimate the selection function of [O II] emitters in the PFS cosmology survey as a function of observational conditions and redshift.

2.3. Scientific Requirements for PFS Cosmology Survey

As discussed above, PFS has the unique capability to execute a very powerful cosmology survey across a wide range of redshifts, considerably extending current and planned BAO surveys on ≤ 4 m-class telescopes. Here Tables 4 and 5 summarize requirements on the survey parameters and the instrument parameters for the PFS cosmological applications.

3. PFS GALACTIC ARCHAEOLOGY

Summary: The Subaru PFS offers an unprecedented opportunity to investigate the assembly histories of both baryonic and dark matter components of two typical, large galaxies, namely the Milky Way and M31. This will be achieved through the measurements of radial velocities and elemental abundances for a large sample (\sim a million) of their member stars. We here describe our Galactic Archaeology (GA) science case for a PFS survey designed to incorporate the envisaged medium-resolution (MR) mode, adopting $R = 5,000$ over the spectral range of $7,100\text{--}8,850 \text{ \AA}$ in the red arm, combined with the baseline low-resolution (LR) mode of $R = 2,000\text{--}3,000$ in the blue arm. The MR mode will allow the measurement of multiple α -element abundances for stars in the Milky Way, elucidating the detailed chemical evolution history for each of the Galactic components. This mode will further enable us to study the global chemo-dynamical evolution and dark-matter distribution of Galactic dwarf spheroidal galaxies, which are the possible remaining building blocks of the Milky Way. This fundamental science is possible only with the α -element abundance measurements and more precise radial velocities offered by the planned medium-resolution mode of PFS.

3.1. Galactic Archaeology Objectives

Our understanding of how galaxies like the Milky Way and M31 formed and evolved in the expanding Universe remains limited. The current paradigm of cosmic structure formation based on the Λ CDM model proposes that galaxy formation is driven by hierarchical assembly of dark matter halos, starting from sub-galactic scales. The repeated merging and overall clustering of many small dark halos over cosmic time forms a larger, galaxy-sized halo. The associated cooling and collapse of baryonic matter confined in the dark halos at each stage of the hierarchy forms the visible galaxies, with the morphology of the final galaxy set by the physics of star formation and of the merging process. Indeed, mergers are predicted to play a key role in the creation of stellar halos, bulges, thick disks and even some parts of thin disks.

TABLE 4
COSMOLOGY SURVEY REQUIREMENTS

Science yield requirements	
Distance measurements	$\lesssim 3\%$ measurement of $D_A(z)$ and $H(z)$ in each of 6 redshift bins via BAO (0.8–1.0, 1.0–1.2, 1.2–1.4, 1.4–1.6, 1.6–2.0, and 2.0–2.4)
Dark energy reconstruction	$\lesssim 7\%$ measurement of $\Omega_{\text{de}}(z)$ in each of 6 redshift bins via BAO
Curvature	Measure Ω_K to $\lesssim 0.3\%$ via BAO
Growth of structure	$\lesssim 6\%$ measurement of the growth rate of structure in each of 6 bins via RSD
Galaxy catalog requirements	
Redshift range	$0.8 \leq z \leq 2.4$ ($0.8 \leq z \leq 1.6$ minimum)
Number density of galaxies	$\geq 2900 \text{ deg}^{-2}$
dN/dz of ELGs	$\bar{n}_g P_g > 1$ ($0.8 < z < 1.6$) or $\bar{n}_g P_g > 0.5$ ($1.6 < z < 2.4$) at $k = 0.1 h/\text{Mpc}$
Total survey area	$\geq 1400 \text{ deg}^2$
Incorrect redshift fraction	$< 1\%$
Redshift precision, accuracy	$\Delta z/(1+z) < 0.0007$, 1σ ($\sigma_v < 200 \text{ km/s}$)
Survey geometry	Width > 7.5 degrees; ≤ 4 contiguously-connected survey regions
Survey implementation requirements	
Total nights	≈ 100 clear nights
Lunar phase	Dark (1 of 2 visits) or age < 7 days (other visit)
Imaging survey	HSC <i>gri</i> data to ≈ 26 th magnitude AB (5σ)

TABLE 5
PFS INSTRUMENT REQUIREMENTS FOR THE PFS COSMOLOGY SURVEY

Wavelength coverage	$650 \leq \lambda \leq 1260\text{nm}$ ($650 \leq \lambda \leq 1000\text{nm}$ minimum)
Number of fibers	2400
Overhead	$< 0.2 \times$ the open-shutter time
Throughput	Average $> 22\%$ (red) or $> 24\%$ (NIR) Worst part of band, $> 20\%$ (red) or $> 18\%$ (NIR) (Excludes atmosphere, central obscuration + WFC vignetting, and fiber aperture effect.)
Fiber aperture factor	Encircled energy in fiber is $\geq 59\%$ (point source) or $\geq 45\%$ (galaxy, $r_{\text{eff}} = 0.3''$) (Equivalent to $0.8''$ FWHM seeing + $11 \mu\text{m}$ rms/axis additional aberration + $0.12''$ fiber offset.)
Spectrograph image quality	$\leq 14 \mu\text{m}$ rms per axis (excluding fiber geometric size, pixel tophat, and internal defocus due to thickness of red CCD)
Spectral resolution	Red: $R \sim 3000$; NIR: $R \sim 4000$ (to resolve out OH lines but limit read noise)
Stray light	Near OH lines: Lorentzian wings at $\leq 3 \times$ amplitude of perfect grating Diffuse: equivalent to $\leq 2\%$ of total sky brightness spread over detector
Read noise	≤ 3 (red) or ≤ 4 (NIR) e^- rms per pixel (If the NIR channel is not reset between exposures, $\leq 4\sqrt{2} e^-$ rms is acceptable.)
Sky subtraction accuracy	$< 1\%$ of sky background per 4-pixel resolution element

However, CDM models have encountered several fundamental difficulties in explaining observations on galactic scales; the model predicts an excess of small scale clustering power than observed. One of the most serious issues is the prediction of many more subhalos in a Milky Way-sized system than the modest number of visible satellites. This discrepancy can only be reconciled if the vast majority of small halos are dark. Our understanding of the star formation process on these small scales, which correspond to dwarf satellite galaxies, remains limited, so there may well be a large population of dark satellites. They would then only reveal their presence through their dynamical effects on visible systems. Alternatively, the assumption that CDM is collisionless may not be correct (Ostriker & Steinhardt 2003, see Fig. 11 for the predictions of various dark matter models). The merging history of the ‘building blocks’ of galaxies is determined by the power spectrum, i.e. by the nature of dark matter, and this we plan to investigate through the study of the stellar populations in both the Milky Way and M31.

Our primary science goal with Subaru/PFS is thus to constrain the assembly process of dark matter halos on Galactic scales, and in particular test the predictions of CDM, by dedicated observations of old stars nearby, formed at high look-back times. Resolved ancient stars in the Milky Way, M31 and

other Local Group galaxies are ideal targets because they offer us our most detailed views of galactic structure and evolution through their kinematics and chemical abundances (Freeman & Bland-Hawthorn 2002). Kinematics of stars reflect past galaxy collapse and/or merging events. Their distribution in phase space as defined by integrals of motion such as angular momentum remains basically unchanged (e.g., see Fig. 12 and Helmi & de Zeeuw 2000). The chemical abundances of stars reflect their past star-formation history and chemical evolution, possibly in association with the dynamical state of proto-galactic clouds such as their collision and merging (e.g., De Silva et al. 2007; Nissen & Schuster 2010). All of these processes are predicted to be controlled by hierarchical clustering of CDM via self-gravity on galactic and sub-galactic scales (e.g., Bullock & Johnston 2005; Cooper et al. 2010; Font et al. 2011). Thus, to assess what CDM models predict, it is essential to derive the spatial distribution of dark matter subhalos in the Galaxy and M31 through their dynamical effects on visible stellar systems. Stars are indeed ideal tracers of a background gravitational field dominated by dark matter.

To make progress we propose to obtain spectra for about a million stars in the Milky Way and M31, as one component within the framework of the proposed PFS Subaru Strategic Program. These spectroscopic studies will be in strong syn-

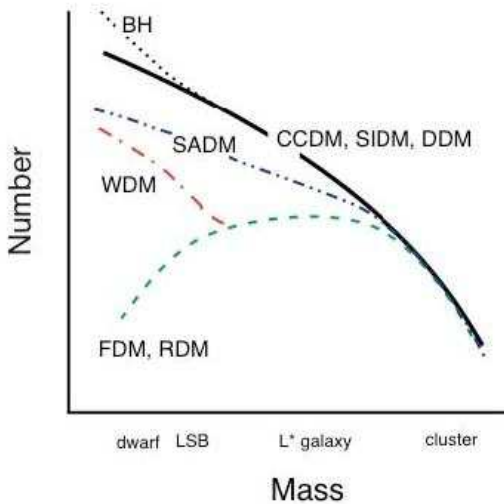


FIG. 11.— An illustration of how the number of objects of a given type depends on their present day mass for different dark matter models (Ostriker & Steinhardt 2003) including Collisionless Cold dark matter (CCDM), Strongly Self-Interacting dark matter (SIDM), Warm dark matter (WDM), Repulsive dark matter (RDM), Fuzzy dark matter (FDM), Self-Annihilating dark matter (SADM), Decaying dark matter (DDM) and Massive Black Holes (BH). Observations on small scales are key to distinguishing these.

ergy with the upcoming astrometric satellite, Gaia, that will provide very precise measurements of distances and proper motions for Galactic stars, and with the HSC survey which will provide the essential large imaging data set. Therefore, PFS, in combination with Gaia and HSC, will provide us with unique data in the area of near-field cosmology. With these data we hope to gain an ultimate understanding of the nature of dark matter and the associated galaxy formation processes.

The main questions we seek to address in our dedicated Galactic Archaeology (GA) survey are summarized as follows.

1. *What is the merging history of the Milky Way? – addressing the role and nature of dark matter in galaxy formation.*
 2. *How did the old Galactic components (thick disk and stellar halo) form? – addressing baryonic physics at early epochs.*
 3. *How does M31 differ from the Milky Way? – contrast merging and baryonic processes on small scales in two systems.*
- 3.2. *Science goals with the planned medium-resolution mode*

The implementation of the planned MR mode of $R = 5,000$ in the red arm will allow us to investigate further important aspects in the GA science case. We describe here the two main science goals in GA with the MR mode: α -element to iron abundance ratios and precision radial velocities.

3.2.1. Alpha elements

The planned MR mode will enable us to unravel the temporal chemical evolution of building blocks of the Galactic halo and thick disk, in addition to surviving Galactic satellites, through their elemental abundances. In addition to iron, the α -elements observable in the wavelength range

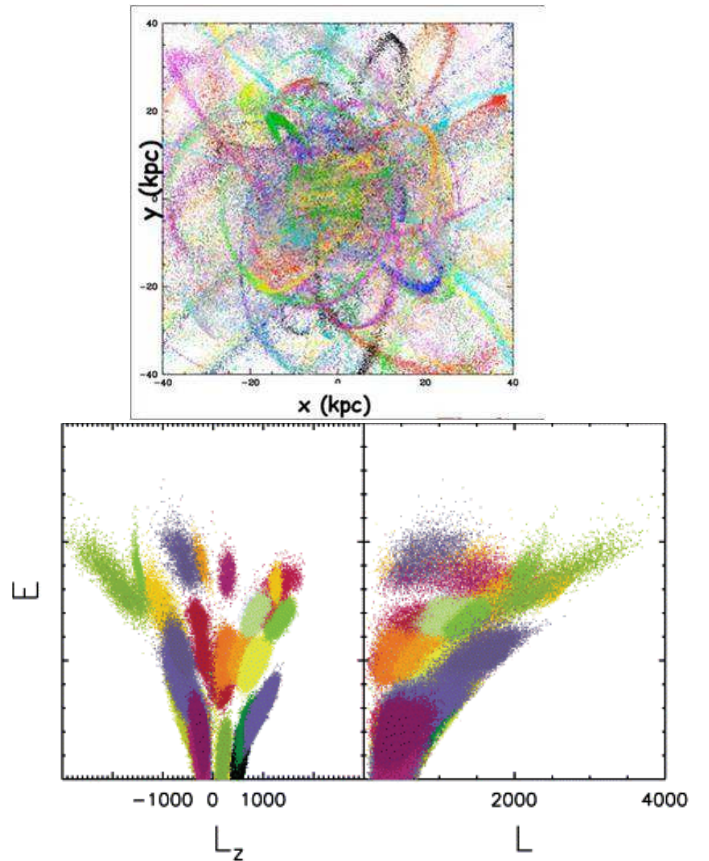


FIG. 12.— Top: Model distribution of tidal streams in a Milky Way-like galaxy in spatial coordinates where the different colors represent different satellites (from Freeman & Bland-Hawthorn 2002). These stream-like features disappear after several dynamical times. Bottom: Model distribution of nearby stars in the integrals of motion space, i.e., E vs. L_z and E vs. L , based on numerical simulations of satellites falling into the Milky Way (from Helmi & de Zeeuw 2000). The different colors represent different satellites. Shown is the final distribution of stars after 12 Gyr within about 6 kpc from the Sun, after convolution with the errors expected for Gaia. It is clear that each of the progenitor galaxies can be traced via the current phase space distribution.

$\lambda \simeq [700, 900]$ (nm) provide the ratios $[X/Fe]$ with $X=Mg, Si, Ca, Ti$ (Fig. 13). These abundance ratios depend sensitively on the relative contributions of core collapse (Type II) supernovae, from short-lived massive stars (masses greater than $\sim 8M_{\odot}$) and Type Ia SNe, which explode on longer timescales. Stars formed from gas that was enriched predominantly by Type II SNe show a high $[\alpha/Fe]$ ratio, reflecting the yields of core-collapse SNe; such ‘high-alpha’ stars will be expected to form early in the enrichment process, on timescales of 10^7 years after the onset of star formation, a typical life time of the SN progenitors. Further, more massive progenitors produce higher α -element abundances (see Fig. 14 for the case of oxygen, one of the α -elements). On the other hand, Type Ia SNe produce very significant iron on longer timescales, typically $\sim 10^9$ years after the birth of the progenitor stars (with $< 8M_{\odot}$); stars formed out of gas that has been enriched by Type Ia SNe show a low $[\alpha/Fe]$ ratio. Thus, the plot of $[\alpha/Fe]$ vs. $[Fe/H]$ shows a high $[\alpha/Fe]$ plateau at low $[Fe/H]$ where short-lived Type II SNe dominate then a turn-down at higher $[Fe/H]$ – but fixed delay time ($\sim Gyrs$) – when Type Ia SNe start to explode and contribute iron. For example, a system with lower star formation rate (SFR) shows the turn-down in $[\alpha/Fe]$ vs. $[Fe/H]$

at lower [Fe/H]. Also, if the initial mass function (IMF) of core-collapse progenitors were biased to more massive stars, the $[\alpha/\text{Fe}]$ ‘plateau’ would have a higher value; a change of IMF slope of ~ 1 over the progenitor mass range of 10 to $100 M_{\odot}$ predicts a difference in $[\alpha/\text{Fe}]$ of at least 0.3, which is thus detectable if this ratio is measured to better than 0.2 dex (Wyse & Gilmore 1992).

Therefore, in addition to the overall metallicity (provided by our low-resolution (LR) survey) which reflects the integrated star formation and chemical evolution up to that star’s birth, the measurements of $[\alpha/\text{Fe}]$ ratios provided by the MR mode will enable us to identify substructures through chemical ‘tagging’ with elemental abundance patterns, establish timescales of enrichment and star formation and constrain the IMF, for each of the major stellar components of the Milky Way and surviving satellite galaxies. Indeed, this is what Galactic Archaeology should ultimately pursue as a goal, based on coordinated observation of higher-resolution stellar spectra.

It is also worth emphasizing that Subaru/PFS will offer us a very large FoV that is ideal for exploring Milky Way dwarf spheroidal (dSph) galaxies, such as Fornax, Ursa Minor and Sextans, out to their tidal radii. In order to measure the enrichment histories of these systems, it is essential to measure their $[\alpha/\text{Fe}]$ distributions across large spatial areas, whereas present samples with elemental abundance measurements are limited to the stars in the inner regions (e.g., Kirby et al. 2009, 2010). PFS’s spectral coverage, resolution, and field of view will make it the most powerful instrument to study the putative building blocks of the Milky Way halo and to study star formation at the smallest scales.

3.2.2. Precision radial velocities

The red-arm MR mode provides us with more precise radial velocities of stars than the original spectrograph design can achieve. The MR mode will provide velocities with errors $\sim 3 \text{ km s}^{-1}$ rather than $5\text{--}10 \text{ km s}^{-1}$ with the LR mode. This improvement for radial velocity measurements is essential for isolating cold kinematic substructures in the halo and thick disk. These substructures possibly originate from building blocks of the Milky Way such as dSphs, with adiabatic evolution in phase space ‘cooling’ their internal kinematics. Arguably even more importantly, the MR mode will enable us to separate and measure the internal kinematics of Galactic dSphs (having velocity dispersion typically $< 10 \text{ km s}^{-1}$) over much larger spatial areas—out to their tidal radii—than previous spectroscopic studies have explored with comprehensive sampling.

Our present investigations of the dark-matter distribution in dSphs are mostly limited to the inner regions, where abundant member stars are available from spectroscopic observations even with a small FoV (e.g., Walker et al. 2009). Recently, Walker & Peñarrubia (2011) develop a method for measuring the slopes of mass profiles in the inner regions of dSphs and conclude that the Fornax and Sculptor dSphs have ‘cores’ of constant dark-matter density. This technique relies upon the existence and identification of chemodynamically distinct sub-populations of member stars, each defined by spatial distribution, kinematics and metallicity. This motivates the PFS survey of these and other dSphs, to obtain the necessary velocity and metallicity data to apply their method. Further, most existing mass models of dSphs are based on the simple assumption of spherical symmetry, and in order to derive more detailed, realistic spatial distributions of their dark

halos, such as their global shape and mass, we require line-of-sight velocity data for stars over much larger areas, and full two-dimensional coverage (not just major/minor axes), as demonstrated by recent mass models (e.g., see Fig. 15 and Hayashi & Chiba 2012). It is also of great importance to have velocity data out to the tidal radii of dSphs, thereby enabling us to estimate the true total mass of a dark halo (through the abrupt change of the velocity dispersion profile in the edge) and detecting any effects of Galactic tides in their outskirts.

The advent of the large FoV and fiber multiplexing of Subaru/PFS is tremendously advantageous in selecting member stars of dSphs from background/foreground field stars out to their tidal radii (Fig. 16). It is worth noting here that since the probability of finding true member stars in the outer parts of dSphs is generally small, a pre-imaging survey of target dSphs using HSC with a newly developed narrow-band filter (NB515 filter with $\text{CW} = 5145 \text{ \AA}$ and $\text{BW} = 80 \text{ \AA}$, which is similar to the DDO51 filter²¹) will be very useful for efficiently distinguishing red-giant branch (RGB) stars in dSphs from foreground dwarf stars. Our experiments using Suprime Cam with a proto-type NB515 filter suggest that the number of RGB candidates within a fiducial RGB locus of a color-magnitude diagram for observed stars, after NB515-imaging selection, is narrowed down to about 50 % of that without using this NB filter (Tanaka et al. 2013 in preparation). Thus, the combination of HSC and PFS will allow us to explore this important dark-matter science; dSphs are the ideal sites for studying the nature of dark matter because these galaxies are largely dark-matter dominated and their past star formation is not likely to have modified the dark-matter distribution. Furthermore, this selection of member stars in dSphs is essential for the measurement of their α -element abundances with the same MR mode out to large radii, thereby enabling us to characterize the global chemo-dynamical evolution of dSphs.

3.3. GA survey plan

Now that the MR mode will allow us to address GA science subjects beyond what is achievable with the LR mode as described above, we summarize our survey plan in Table 6. The primary targets are stars in the Milky Way and dSphs using both the MR and LR modes and bright red giant stars in a wide area of M31’s halo with the LR mode.

3.3.1. The Milky Way and dSphs

As detailed in Section 3.4, the MR mode will enable us to obtain the ratios $[\text{X}/\text{Fe}]$ with $\text{X}=\text{Mg, Si, Ca, Ti}$ with precisions of $\Delta[\text{X}/\text{Fe}] \sim 0.2$ dex for spectra with S/N of about 60 per resolution element. Primary Milky Way targets in our dedicated large survey using this higher-resolution mode will be bright stars with $V < 19$ mag, which are observable even in bright time; exposure times of 2700 sec are needed to obtain sufficiently accurate $[\text{X}/\text{Fe}]$ ratios. The MR mode will be further dedicated to the survey of fainter Milky Way stars, in addition to member stars of dSphs with $V < 21$ mag in grey/dark time, for which we require exposure times of 7200 sec. Thus, this mode will offer us an efficient usage of allocated PFS nights including some bright/grey time.

The LR PFS survey of radial velocities combined with Gaia astrometry data will provide six-dimensional phase-space in-

²¹ The DDO51 filter is an intermediate filter in the Washington photometric system, where the strong surface gravity sensitivity of the Mg I triplet and MgH band features near 5150 \AA allows discrimination between dwarfs and giants of F-K spectral type.

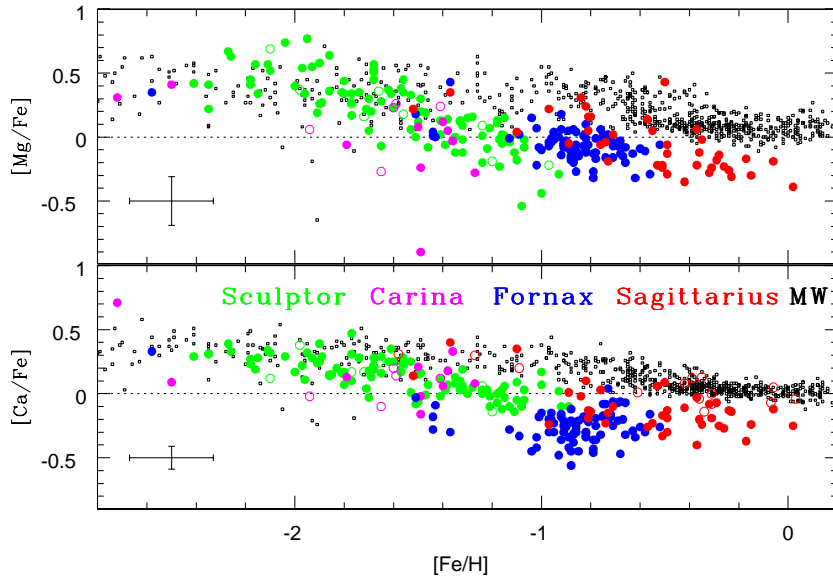


FIG. 13.— Alpha-elements (Mg and Ca) in four nearby dwarf spheroidal galaxies: Sgr, Fnx, Scl and Carina. The small black symbols denote the abundances of local MW disk and halo stars (from Tolstoy et al. 2009). PFS will measure the α -element abundances for a much large number of stars in the Galactic halo, thick disk and their substructures, in addition to member stars across the radial extent of dSphs, identified by their kinematical and spatial distributions.

TABLE 6
SUMMARY OF GALACTIC ARCHAEOLOGY SURVEY

Survey	Mode	Mag. Range (mag)	Exposures (sec)	No. Fields	Survey Time (nights)	Comments
<i>Bright time:</i>						
The Milky Way	MR+LR(blue)	$V < 19$	2700	208	20	Thick disk: $b = 30, 0 < l < 270$
The Milky Way	MR+LR(blue)	$V < 19$	2700	46	5	Thick disk: $b = -30, 60 < l < 120$
<i>Grey time:</i>						
dSph	MR+LR(blue)	$V < 21$	7200	28	7	Fnx, Scl, LeoI, UMi & Dra
The Milky Way	MR+LR(blue)	$V < 21$	7200	40	10	Halo: $47 < b < 73, l = 90 & 270$
The Milky Way	LR	$V < 22$	7200	48	12	Outer disk: $l = 180$
The Milky Way	LR	$V < 22$	7200	24	6	'Field of Streams'
<i>Dark time:</i>						
dSph	MR+LR(blue)	$V < 21$	7200	8	2	Sextans
M31 halo	LR	$21.5 < V < 22.5$	18000	50	31	HSC sample
dlrr	LR	$V < 22.5$	18000	4	3	NGC6822, IC10 & WLM
Total				456	96	

formation for Galactic stars, with which it is possible to identify individual progenitors as building blocks of the Milky Way, in the form of kinematically distinct clumps in phase space (Helmi & de Zeeuw 2000; Gómez et al. 2010). With $[\alpha/\text{Fe}]$ ratios of these stars obtained from our MR spectroscopy, it will be possible to set important limits on the star formation and chemical evolution histories in each building block of the Milky Way halo. Furthermore, the $[\alpha/\text{Fe}]$ ratios are excellent discriminators of the thick disk from the thin disk, with which one can set important limits on the formation scenario of the thick disk by investigating its rotational and orbital properties as a function of $[\text{Fe}/\text{H}]$ (Lee et al. 2011). We will also quantify the velocity distribution of the thick disk as a function of spatial coordinates and the asymmetry/symmetry of its dynamical properties, providing constraints on the role of dynamical heating by CDM sub-halos and/or visible satellites in thick disk formation (e.g., Hayashi & Chiba 2006). To address these issues, we focus on three regions sensitive to azimuthal streaming velocity (disk rotation) at the halo/disk interface: $(l, b) = (90^\circ, \pm 30^\circ)$ and $(270^\circ, +30^\circ)$, where each block includes a sufficient number of targets (e.g., as many as 2000 stars per PFS FoV, in-

cluding more than 500 F/G turnoff stars with $V < 20$ mag) to derive the spatial dependence of the velocity distribution. Full spatial motions of these stars, in synergy with Gaia, and their $[\alpha/\text{Fe}]$ ratios from the MR mode of PFS will allow us to gain new insights into the origin of the thick disk as well as the star formation history of halo progenitors. In addition, taking advantage of the wide FoV of PFS, we will also target other Milky Way samples and obtain the distribution of $[\alpha/\text{Fe}]$ ratios for selected bright stream stars ($V < 19$ mag), so that their star-formation history is constrained and compared to other regions. This survey requires in total ~ 300 PFS pointings (~ 390 sq. degree), for each of which 2700 sec of exposure is required.

In addition to these survey regions using the MR mode, we plan to observe Milky Way stars as faint as $V = 22$ mag, with the LR mode, in the regions of the outer disk near $l = 180^\circ$ and in the 'Field of Streams', to clarify the chemo-dynamical nature and origin of these substructures. In particular, outer disk regions including the so-called Monoceros stream are expected to contain abundant tidal debris from a merging dwarf galaxy (e.g. Peñarrubia et al. 2005) which can be probed by observing G5V stars as faint as $V = 21.5 - 22$ mag with

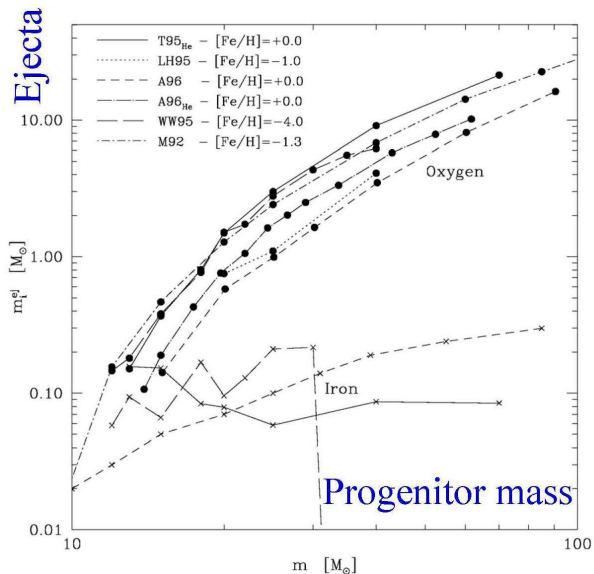


FIG. 14.— Mass of ejecta from Type II SN in the form of oxygen (an α -element; upper four curves) and iron (lower three curves) yields as a function of progenitor mass (from Gibson 1998). Note that a higher oxygen yield is ejected from a more massive progenitor, while the iron yield is approximately constant.

Subaru/PFS; a $V = 20$ mag limit, practical for 4m telescope projects, would be largely incomplete in probing these merger remnants (see Fig. 17).

Our proposed survey regions are summarized in Fig. 18. We note the number of sample stars required in each survey mode, i.e. for thick disk, stellar halo and outer disk, follows the justification of the required sample size described in Section 3.2.

As described in the previous section, the MR mode in Subaru/PFS will be essential to determine the global chemodynamical state of Galactic dSphs across their radial extent. We will use the MR mode for most of these dSphs in grey time, where we will observe member stars as faint as $V = 21$ mag with 7200 sec of exposure for each PFS pointing. We require four PFS pointings for those dSph with large tidal radii (Fornax, Sculptor and UMi: see Fig. 16) and one PFS pointing for each of LeoI and Draco. Since repeat velocity measurements are necessary for identifying binary effects, we require at least 28 PFS pointings in total for these dSphs. Sextans has a large tidal radius (~ 160 arcmin), for which we need many PFS pointings. To efficiently execute this observing run, we will request dark time in spring for this particular target. For a sample of Local Group dIrr galaxies, we will target RGB stars down to $V = 22.5$ mag (in the summer/fall season) using the LR mode and in order to obtain S/N as large as 20 at $\lambda = 5,000 \text{ \AA}$, we require dark time and 5 hr exposures per pointing for these stars.

The Gaia intermediate data release is expected by the time the PFS GA survey commences. Gaia and ground-based imaging surveys, such as Pan-Stars, VST, and Skymapper, are likely to find many streams and ultra-faint dwarf galaxies. The MR mode of PFS will uniquely provide the resolution and field of view necessary for follow-up spectroscopy of these new-found structures.

3.3.2. The M31 halo

The primary targets in the M31 survey are bright red giants with $21.5 < V < 22.5$ mag, i.e., stars around the tip

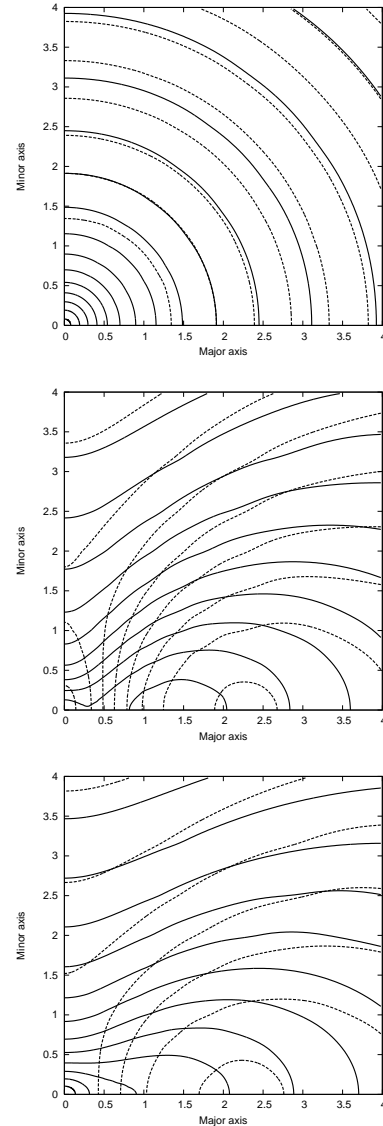


FIG. 15.— Contours of line of sight velocity dispersion of stars in the meridional plane for models of dSphs, where major and minor axes are normalized by a stellar scale length. Solid and dashed lines show NFW and cored dark-halo models, respectively (from Hayashi & Chiba 2012). Top: spherically symmetric model for both dark halo and luminous stellar components, with their axial ratios denoted as $Q = 1$ and $q = 1$, respectively. Middle: $(Q, q) = (1, 0.8)$. Bottom: $(Q, q) = (0.8, 0.8)$. Note that the 2D distribution of velocity dispersion depends sensitively on shapes and profiles of both dark halo and luminous stellar components. PFS, with its large FoV, will play an essential role in these velocity measurements.

of the RGB with $I \simeq 20.5$ selected along the minor axis of the galaxy (Fig. 19). Pre-imaging observations and selection of the candidate halo giants will be provided by an HSC imaging survey and we will utilize a newly developed narrow-band filter, NB515, to assist in removing foreground Galactic dwarfs. A survey along the minor axis will enable us to derive the chemodynamical properties of the general M31 halo as well as to study in detail several stellar streams, including a cold stream-like feature in the north-west part of the halo, part of which corresponds to Stream F discovered by previous Subaru observations (Tanaka et al. 2010). The distribution of stars along these M31 streams will be especially useful in constraining the number of orbiting dark matter subhalos, which

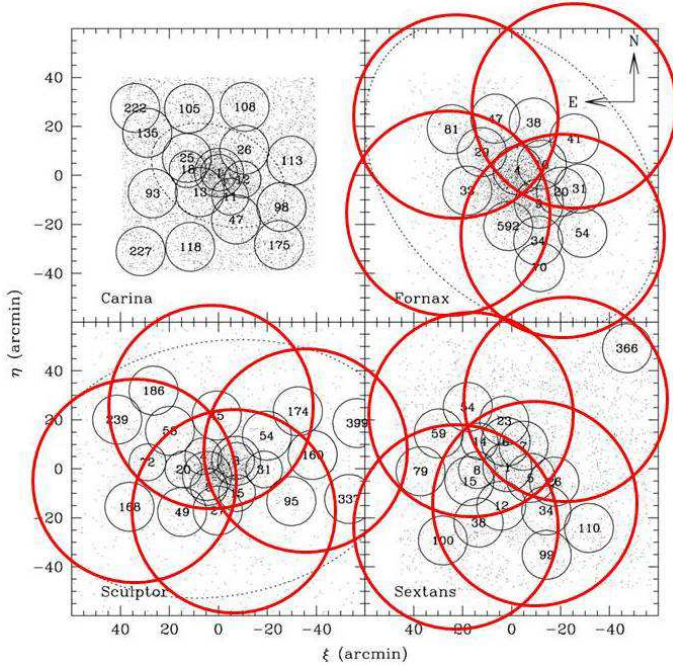


FIG. 16.— Proposed Subaru/PFS pointings (red circles) for the wide-field velocity measurements of some Galactic dSphs (Fornax, Sculptor and Sextans) reaching their tidal radii (dotted lines). Note that previous velocity measurements were limited only to the central parts (black circles) (adapted from Walker et al. 2009).

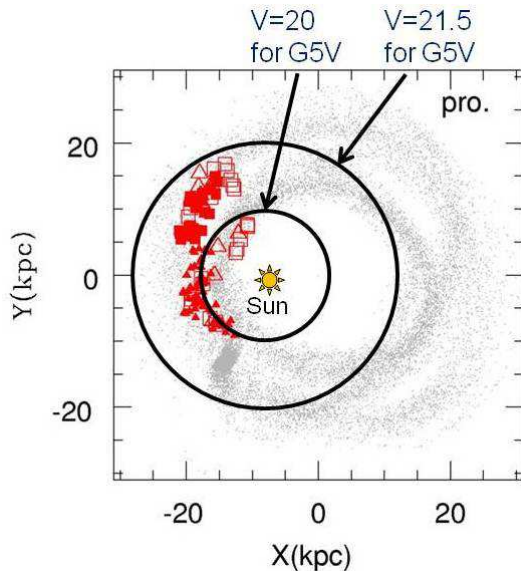


FIG. 17.— Spatial distribution of simulated tidal debris of a merging dwarf galaxy associated with the Monoceros stream (adapted from Peñarrubia et al. 2005). The Sun is placed at $(X, Y, Z) = (-8, 0, 0)$ kpc. Red triangles and squares denote positions of previously detected stream stars. Note that $V = 20$ mag limit for G5V stars is largely incomplete in probing these tidal debris compared with $V = 22$ mag limit.

are predicted to induce detectable density variations along the stream through dynamical disturbances (Carlberg et al. 2011). A careful subtraction of foreground Milky Way stars through spectroscopic observations will be crucial for constraining the number of orbiting CDM subhalos in Andromeda and comparing with theoretical predictions.

PFS will measure radial velocities and metal abundances for M31 halo stars to set important constraints on their in-

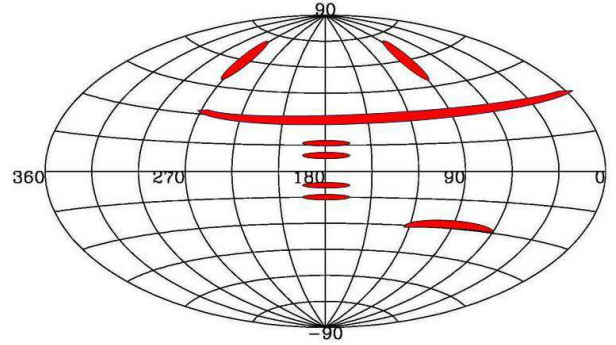


FIG. 18.— Proposed survey fields in the thick disk, stellar halo, and outer disk regions of the Milky Way in the galactic coordinate system.

trinsic chemo-dynamical properties. Spectroscopic metallicities derived for individual stars will represent a major advance over those derived photometrically or by stacking spectra. To estimate the number of RGB stars in the M31 halo per PFS field, we follow the recent observations with Keck/DEIMOS by Gilbert et al. (2012), in which the pre-selection of candidate RGB targets using the DDO51 filter was made. At a projected distance of 80 kpc from the M31 center, we expect ~ 2600 objects per PFS field (including significant foreground/background contamination even after NB515 pre-selection), among which about 100 secure RGB stars of the M31 halo can be extracted. We propose to observe ~ 66 sq. degrees (~ 50 pointings) as shown in Fig. 19. In order to obtain spectra with $S/N \simeq 20$ per resolution element at $\lambda = 5000$ Å, 5 hr exposures are required at $V = 22.5$ mag. Thus, $\simeq 30$ nights are required for this component of the survey.

In summary, for all the GA survey targeting the Milky Way, dSphs and the M31 halo, we require a total of 96 nights.

3.4. Estimation of stellar atmospheric parameters from MR spectra

This medium-resolution survey at $R = 5,000$ will yield stellar spectra similar to those provided by the Keck/DEIMOS instrument, with which we have sufficient experience and well-calibrated techniques to measure multi-element α abundances and quantify their uncertainties (Kirby et al. 2008, 2010). MR spectra with 1.3 Å to 1.5 Å FWHM in the red spectral region ($7,000$ Å $\leq \lambda \leq 9,000$ Å, see Fig. 20) yield multiple abundance dimensions, such as $[\text{Fe}/\text{H}]$ and $[\alpha/\text{Fe}]$, as well as other stellar atmospheric parameters, as clearly demonstrated by E. Kirby and his collaborators using Keck/DEIMOS data (Kirby et al. 2008, 2009). The method makes use of a large grid of stellar synthetic spectra parametrized by effective temperature (T_{eff}), surface gravity ($\log g$), metallicity ($[\text{Fe}/\text{H}]$), and α -element abundance $[\alpha/\text{Fe}]$. The atmospheric parameters and metal abundances are then derived with the χ^2 fitting to an observed PFS spectrum. This spectral modeling method for the determination of metallicities is advantageous compared to an empirical spectrophotometric one, such as the Ca II infrared triplet method, where the latter is affected by the assumed ratio of $[\text{Ca}/\text{Fe}]$ and limited to the calibrated range of metallicity. Furthermore, this method enables us to obtain individual abundances of α -elements in addition to Fe, namely Mg, Si, Ca, and Ti, which characterize the yields of massive stars that exploded as Type II SNe.

Fig. 21 shows the feasibility of deriving $[\text{Fe}/\text{H}]$ and $[\text{Mg}/\text{Fe}]$ from PFS-MR spectra of $\Delta\lambda = 1.4$ Å, in comparison with

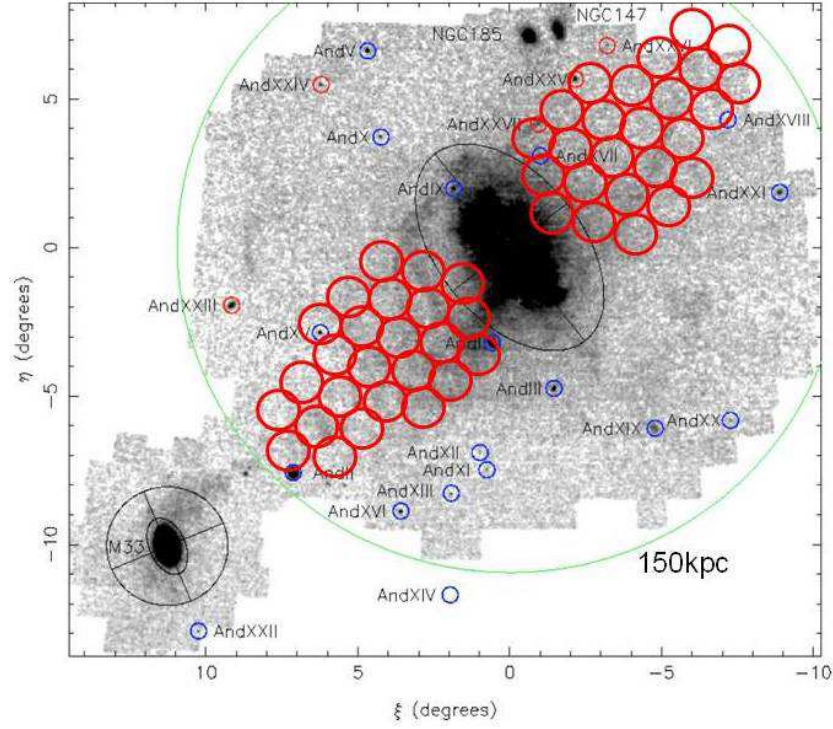


FIG. 19.— Proposed PFS pointings along the minor axis of M31’s halo (~ 50 pointings), in which several stellar streams are included. The map of RGB stars is taken from Richardson et al. (2011).

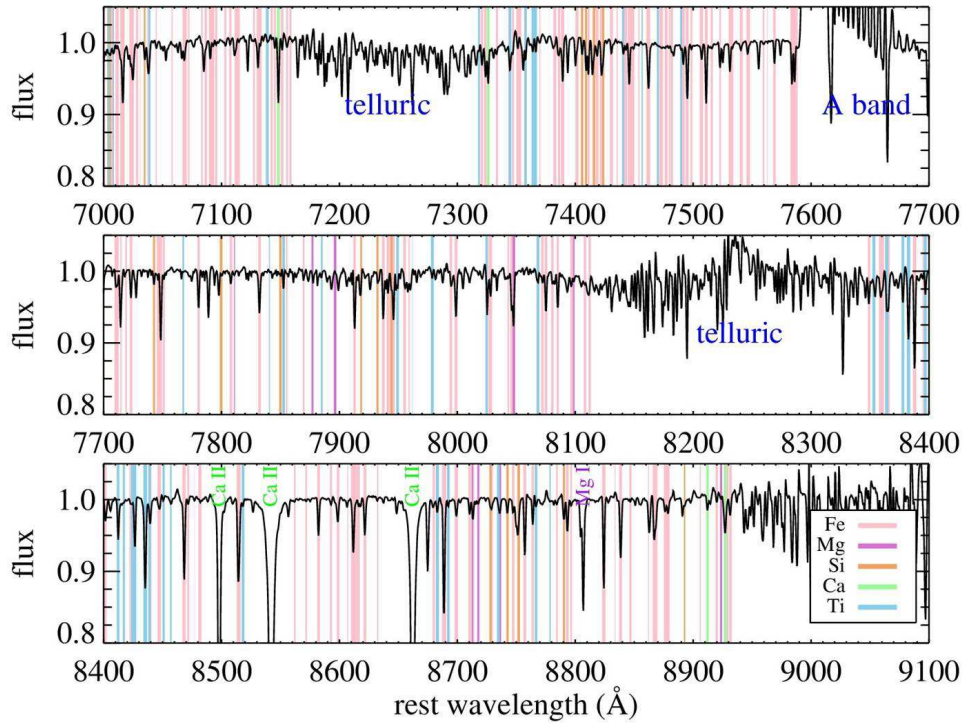


FIG. 20.— Spectrum of a red giant star in the Sculptor dSph, with $\Delta\lambda = 1.5 \text{ \AA}$. This has been obtained by slightly degrading a Keck/DEIMOS spectrum with $\Delta\lambda = 1.2 \text{ \AA}$. This spectral region contains many weak metal lines as well as significant Ca II triplet lines.

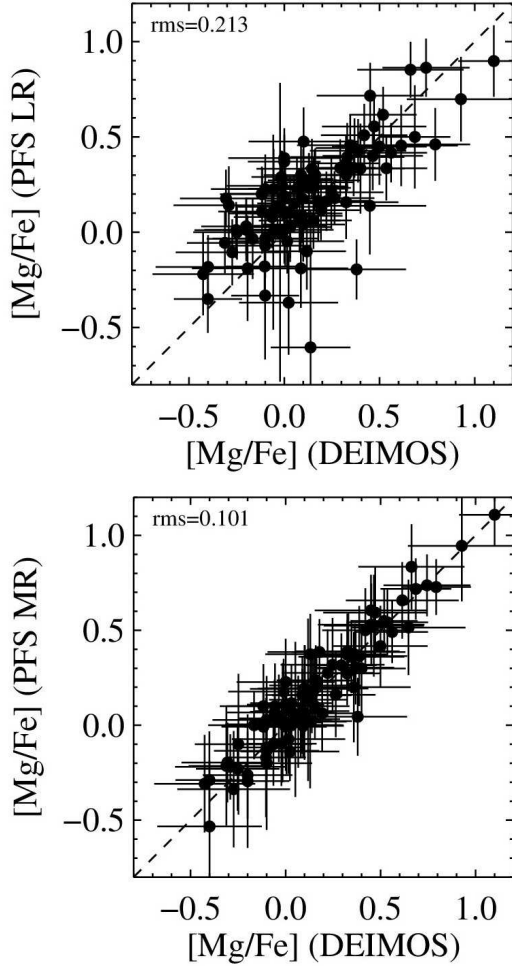


FIG. 21.— Left: Comparison of $[\text{Mg}/\text{Fe}]$ ratios derived from PFS-LR spectra ($\Delta\lambda = 3 \text{ \AA}$) to those of the original DEIMOS data ($\Delta\lambda = 1.2 \text{ \AA}$; where the former spectra are made by degrading the resolution of the latter ones), for 400 red giant stars in the Sculptor dSph.. Right: The same comparison but for PFS-MR spectra ($\Delta\lambda = 1.4 \text{ \AA}$). These panels indicate that the expected errors in $[\text{Mg}/\text{Fe}]$ derived from PFS-LR spectra (~ 0.3 dex) are too large to distinguish field halo stars with $[\text{Mg}/\text{Fe}] \sim 0.3$ dex from disk stars and/or recently accreted stars with $[\text{Mg}/\text{Fe}] \leq 0.0$. On the other hand, PFS-MR provides the $[\text{Mg}/\text{Fe}]$ measurement precision required for this determination.

$\Delta\lambda = 3 \text{ \AA}$ (LR mode). It is clear from these figures that the uncertainty in $[\text{Mg}/\text{Fe}]$ derived from PFS-MR spectra should be of order ~ 0.2 dex (taking into account an error of $[\text{Mg}/\text{Fe}] \sim 0.15$ dex in DEIMOS) and is thus small enough to distinguish field halo stars with $[\text{Mg}/\text{Fe}] \sim 0.3$ dex from disk stars and/or recently accreted stars with $[\text{Mg}/\text{Fe}] \leq 0.0$. Our simulations using DEIMOS data also suggest that this precision of multi-element α abundances is possible with ~ 0.75 hour exposures for bright stars of $V < 19$ in bright time and ~ 2 hour exposures for stars as faint as $V = 21$ in grey/dark time.

3.5. Instrument requirements for MR GA survey

For the MR mode, a spectral resolution at least as high as $\Delta\lambda = 1.5 \text{ \AA}$ and $S/N = 60$ per resolution element over the wavelength range $7,100 \text{ \AA}$ to $8,850 \text{ \AA}$ will allow us to determine $[\text{X}/\text{Fe}]$, with $\text{X} = \text{Mg}, \text{Si}, \text{Ca}, \text{Ti}$, to a precision of ~ 0.2 dex. The resolution of the LR mode ($\Delta\lambda = 3 \text{ \AA}$, $R \sim 3,000$) yields $\Delta[\text{X}/\text{Fe}] \sim 0.3$ dex, insufficient to distinguish field halo stars, with $[\text{X}/\text{Fe}] \sim 0.3$, from disk and tidal stream stars with

$[\text{X}/\text{Fe}] \sim 0$ (see Fig. 21). A MR capability for PFS, such as described here, is necessary to achieve the science goals proposed in this document.

We also note that in order to determine radial velocities with accuracy of $\sim 3 \text{ km s}^{-1}$, a resolving power of $R = 5,000$ (i.e. that of the planned MR mode) is required with a wide wavelength coverage, in particular for the red region where highest S/N ratios are expected.

The Galactic Archaeology requirements are summarized in Table 7.

In addition to the dedicated GA survey described here, there are a number of other important questions that may be addressed with both LR and MR modes of PFS. These include: (1) chemo-dynamical properties of the Galactic bulge/bar and the transition(s) between the bulge, inner disk and halo components in the Milky Way, (2) kinematics of the outer parts of halo globular clusters in the Milky Way, and (3) identification and analysis of globular clusters in M31. These studies of these issues can be carried out through PI-led programs.

4. PFS GALAXY EVOLUTION SURVEY

Summary: The goal of the PFS Galaxy Evolution Survey is to follow the growth of the full panoply of modern-day galaxies from cosmic dawn to the present. While we know some of the basic physical processes that drive galaxy evolution (dark matter halo merging, gas accretion, star formation and associated energy release, galaxy merging, black hole accretion and associated energy release), how and when they operate, and their relative importance, remain unknown. We will use the unprecedented wavelength coverage of PFS, in particular from 1 to $1.26 \mu\text{m}$, to explore the redshift desert between $1.4 < z < 2.2$ when the star formation rate density and black hole growth were at their peak. Using $\text{Ly } \alpha$ emission, we will trace the growth of galaxies and black holes all the way to the epoch of reionization, $2 < z < 7$. Thanks to deep broad- and narrow-band imaging enabled by the HSC survey, we will be able to study these young galaxies with unprecedented statistics using PFS. We propose a 100 night survey covering 16 deg^2 with these main components: (i) A color-selected galaxy survey of 500,000 galaxies using 785,000 fiber-hours over 16 deg^2 from $z = 1$ to $z = 2$ to a limiting magnitude of $J_{\text{AB}} = 23.4 \text{ mag}$, with a $z < 1$ component limited to $J_{\text{AB}} = 21 \text{ mag}$, and a magnitude-limited component covering 2.6 deg^2 ; (ii) A survey of 140,000 bright dropout galaxies and $\text{Ly } \alpha$ emitters over $2 < z < 7$, using 247,000 fiber-hours; (iii) A survey of $\sim 50,000$ color-selected quasars from $3 < z < 7$, using a total of 1600 fiber hours in this survey and 21,000 fiber hours in the BAO survey.

The most important requirements for our science are the following:

1. The multiplexing capability of PFS is a critical component of our survey design, allowing us to observe hundreds of thousands of objects.
2. The sensitivity in the NIR is most crucial to our redshift success. We assume that in 3 hrs of integration we can measure continuum redshifts from the 4000 \AA break down to $J_{\text{AB}} = 23.4 \text{ AB mag}$. We find that this is achievable with the default instrument configuration, at an effective $R \approx 300$ in the NIR arm, if the scattered light going down each fiber is no more than a few percent of the sky brightness; the nominal requirement is 0.5%.

TABLE 7
SUMMARY OF GALACTIC ARCHAEOLOGY REQUIREMENTS

Mode	Requirements & Comments
LR ($R = 2000\text{-}3000$)	For the Milky Way stars ($V < 22$) and M31 halo ($21.5 < V < 22.5$) Velocity precision of $5\text{--}10 \text{ km s}^{-1}$ [Fe/H] to ~ 0.2 dex, no other elements measurable $\lambda = 3800 \text{ \AA}$ to $1 \mu\text{m}$ incl. Ca II HK, Ca I, Mgb/MgH, CaT ~ 2200 fibers, $\sim 10^6$ stars
MR ($R = 5000$)	For the Milky Way stars ($V < 19$ in bright and $V < 21$ in grey/dark time) Velocity precision of 3 km s^{-1} [Fe/H] to 0.15 dex, [X/Fe] (X=Mg, Si, Ca, Ti) to ~ 0.2 dex $\lambda = 7100$ to 8850 \AA incl. CaT and α -element lines ~ 1000 fibers, $\sim 10^5$ stars

3. We assume that in a 3 hr integration we can achieve $> 5\sigma$ line detections of $\sim 10^{-17} \text{ erg s}^{-1} \text{ cm}^{-2}$ at effective resolution $R = 1300$ for the full spectral band in the blue and red arms and 75% of the NIR arm, including systematic errors in sky subtraction (see §4.3).

4.1. Extragalaxy Science Objectives

The Sloan Digital Sky Survey has provided us with a detailed understanding of the optical properties and large-scale distribution of present-day galaxies. Large redshift surveys such as zCOSMOS (Lilly et al. 2009), DEEP2 (Cooper et al. 2006), and VVDS (Le Fèvre et al. 2005) have studied areas of ≤ 2 square degrees at $z \sim 1$; at this epoch galaxies had similar morphologies, luminosity ranges, and environmental characteristics as they do today. However, the bulk of the stellar and black hole mass was assembled at $1 < z < 2$ (Fig. 22), when the universe was a very different place. We want to understand how galaxies and gas are distributed relative to dark matter halos at these epochs, how each of these components interact (via merging, cooling flows, star formation, energy feedback, and reionization), and whether star formation proceeded in a fundamentally different way at that crucial epoch of mass assembly. To date there are spectroscopic samples of only a few thousand blue, star-forming galaxies with $z > 1.4$, covering $< 1 \text{ deg}^2$ (e.g., Steidel et al. 2010). Particularly difficult to study is the so-called redshift desert $1.4 < z < 2.2$, since no strong and reliable redshift indicators fall in the optical bandpass. Even with the current generation of multi-object near-infrared spectrographs, it will not be possible to survey the solid angles proposed here, which allow us to tie together galaxy evolution with the large-scale environment. The PFS spectrograph, with a wavelength coverage of $0.38\text{--}1.26 \mu\text{m}$, is specifically designed to explore the redshift desert over volumes comparable to the SDSS at low redshift. *We propose the first large-area spectroscopic survey of roughly half a million galaxies in the redshift range $1 < z < 2$, when the bulk of stellar mass was assembled.*

While the bulk of the stellar mass in galaxies was assembled between $1 < z < 2$, the star formation rate density likely peaked at even earlier times (Fig. 22), and so to get a full picture of galaxy evolution we must study the earliest cosmic epochs as well. The wide wavelength coverage of PFS allows us to observe galaxies from $z \sim 2$ to the redshift frontier of $z \sim 7$ (Fig. 22) within the *same survey design*. It is prohibitive to perform a rest-frame optical continuum selection at $z > 2$. Instead we will target high-redshift Lyman break galaxies (LBGs) and Ly α emitters (LAEs) at $2 \lesssim z \lesssim 7$. We will obtain unprecedented numbers of spectra of both populations, particularly at $z > 5$, to probe the epoch of reionization. With these samples we will chart the evolution of star forma-

tion rate, metallicity, galaxy density, and large-scale structure as a function of redshift. We will probe the epoch when the star formation of early galaxies changed the ionization state of the intergalactic medium (IGM) in what is called cosmic reionization. The large area of the PFS spectrograph allows us to survey wide enough areas on the sky to study the topology of ionized bubbles in the IGM at this epoch ($\sim 10^6 \text{ Mpc}^3$) as well as to conduct a census of young galaxies at $2 \lesssim z \lesssim 7$. We will have a sample two orders of magnitude larger than those that came before.

It is now recognized that all massive galaxies contain supermassive black holes (SMBHs) in their centers, with masses ranging from $10^5 - 10^{10} M_{\odot}$. The evolution of black hole growth with cosmic time resembles that of the star-formation activity. The steep drop-off of both at $z < 2$ points to a link between supermassive black hole growth and galaxy formation. Moreover, the masses of SMBHs are correlated with those of their host bulges in the present-day Universe, suggesting that they evolved together (e.g., Kormendy & Richstone 1995; Magorrian et al. 1998; Marconi & Hunt 2003). A full understanding of galaxy evolution requires study of the accretion history of SMBHs. We will target color-selected quasars that are \sim three magnitudes fainter than the SDSS to a redshift of $z = 7$ and study their clustering properties, the evolution of BH mass density with cosmic time, and evolution in the metal content and ionization state of the intergalactic medium.

We propose to study galaxy formation and cosmic reionization from $z = 1$ to 7 seamlessly. We will conduct the first spectroscopic census of young galaxies at $2 \lesssim z \lesssim 7$ up to the reionization epoch, based on 60,000 spectra of LBGs and LAEs in a wide range of environments. No existing or planned galaxy evolution surveys in the next ten years can compete with our combination of depth, redshift coverage, and area (Fig. 23).

The wide wavelength coverage and large area of the PFS will enable an enormously powerful galaxy evolution survey. We envision a 16 deg^2 survey over ~ 100 nights, or a million fiber-hours. All observations will be taken with twenty-minute exposures; given the rapid reconfiguration of PFS, we thus have tremendous flexibility in observing various targets for total integration times ranging from twenty minutes to six hours or more. At $1 < z < 2$, using color selection, we will survey to a depth of $J_{\text{AB}} \approx 23.4$ mag with three-hour integrations, which will allow us to study a fair sample of galaxies down to a stellar mass of $\sim 10^{10} M_{\odot}$ at $z \approx 2$, with a stellar-mass matched $z < 1$ sample down to $J = 21$ mag observed with twenty-minute integrations. Finally, to understand our color selection, we will include a 2.6 deg^2 magnitude-limited

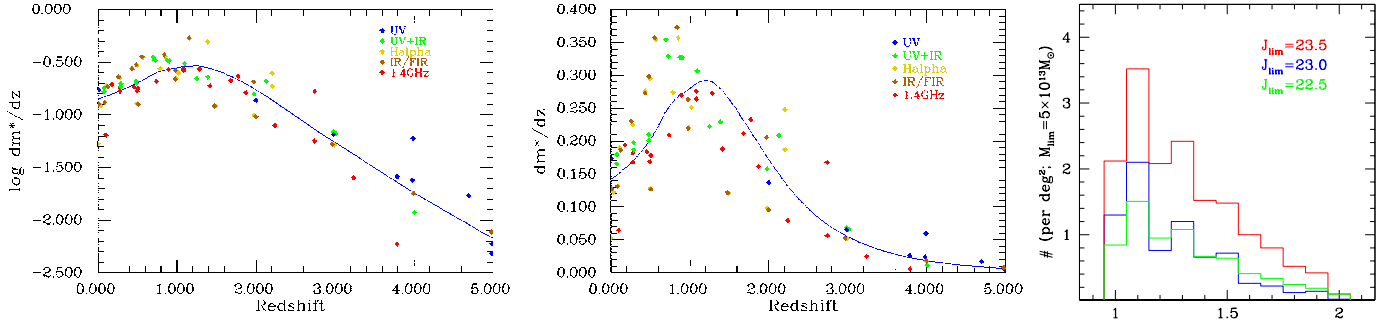


FIG. 22.— *Left*: The differential build-up of stellar mass as a function of redshift using both a logarithmic (left) and linear (middle) stretch. The data are from Behroozi et al. (2013), and dm^*/dz is in units of $[M_\odot/\text{yr}/\text{Mpc}^3]$. *Right*: Expected number of clusters with $M > 5 \times 10^{13} M_\odot$ per deg^2 survey volume with the stated depths. The estimates use the “lightcone” simulations of Sehgal et al. (2010) and populate halos with galaxies using the halo occupation distribution model from Tinker & Wetzel (2010).

survey to $J_{\text{AB}} \approx 23.4$ mag. To extend our study of typical galaxies to yet higher redshift, at $2 \lesssim z \lesssim 7$ we will target star-forming galaxies. We expect to observe 60,000 Lyman break and Lyman alpha emitting galaxies, an order of magnitude increase over existing spectroscopic samples. Taken together, the survey will give us enormous leverage to link the evolution of galaxies from cosmic dawn to the peak epoch of stellar mass growth.

We will focus on three imaging surveys for target selection. We will target 16 deg^2 of the HSC Deep survey that contains existing deep NIR imaging down to $J_{\text{AB}} = 23.4$ mag. HSC UltraDeep covers 3.5 deg^2 and we will perform deeper spectroscopy in this area. Finally, HSC Wide covers 1400 deg^2 , over which we will search for rare high-redshift quasars ($z > 3$).

The primary science goals of the PFS galaxy evolution survey are the following:

1. **The Build-up of Stellar Mass Density:** We will derive stellar masses and star formation rates from the spectra (Fig. 24). It has been shown that stellar population modeling works well even at our low resolution (e.g., Kriek et al. 2006, 2011; Panter et al. 2007; Chen et al. 2012). We will measure star formation rates both from the modeling and from [O II] emission out to $z \sim 2.5$, which we will calibrate using $\text{H}\alpha$ out to $z \approx 1$. At yet higher redshift, we can use the UV continuum as a star formation rate indicator (Fig. 24). We will trace the stellar mass function and star formation history of galaxies as a function of color and galaxy density at $1 < z < 2$.
2. **The Growth of Structure:** We will measure the spatial correlation functions of galaxies on both small and large scales (i.e., one and two halo terms; Fig. 23 right). Spectroscopic redshifts give significantly better clustering measurements than do photometric redshifts, and will allow us to perform halo occupation modeling as a function of redshift. On large scales, we will measure the galaxy bias as a function of galaxy properties and redshift, which is a key constraint on galaxy formation models. On smaller scales, we can study the properties of galaxies in cluster and group environments, and see how galaxy formation is related to environment and dark matter halo mass. We will use a combination of weak lensing from the Hyper Suprime-Cam survey and clustering from the PFS survey at low redshifts, and

clustering alone at higher redshifts to tie the average properties of the galaxy population to their underlying dark matter halos, and the group and cluster halos in which they live. We will also study the cluster/proto-cluster population as a function of redshift. Over the survey volume, we expect to find ~ 325 clusters with mass (at that epoch) $M > 5 \times 10^{13} M_\odot$ (including ~ 65 massive clusters with $M > 10^{14} M_\odot$) at $1 < z < 2$ (Fig. 22), an unprecedented sample when compared to the very few found in current deep pencil-beam surveys (Sehgal et al. 2010). At $2 \lesssim z \lesssim 6$ we expect to find ~ 100 proto-clusters using LBGs and LAEs as tracers.

3. **Gas Inflow and Outflow:** We will trace the interplay between gas accretion and feedback using both direct and indirect means. We will trace the mass-metallicity relation using strong emission-line diagnostics for $z < 1.6$ and with stellar photospheric lines in the UV at $z > 2$ by stacking spectra (Ando et al. 2007). We will search for outflow or inflow using interstellar absorption lines such as Mg II, S IV, C IV, etc in stacked spectra. We will also stack background galaxy and quasar spectra as a function of impact parameter around foreground galaxies to map out the gas kinematics in the outer halos of star forming galaxies (e.g., Steidel et al. 2010; Tumlinson et al. 2011; Bordoloi et al. 2011). Using the galaxies themselves as a backlight, we will search for the signature of cold-gas inflow and test the cold accretion hypothesis (e.g. Dekel & Birnboim 2006) with a sample ~ 20 times larger than the one of Steidel et al.
4. **The Build-up of Supermassive Black Holes:** We will measure the quasar luminosity function from $3 < z < 7$ to ~ 3 mag deeper than the SDSS. A wide-area search of $> 1000 \text{ deg}^2$ is needed to find rare luminous $z > 6$ quasars, while we will study fainter populations over the 16 deg^2 galaxy survey. Using quasar emission lines we will study the evolution of the BH mass function, and the accretion history of these black holes. We will be able to study the clustering properties of the quasar population using cross-correlation with the dropout galaxies in our sample, which will reveal the typical dark halo mass of the quasar population as a function of redshift and luminosity (e.g., Adelberger & Steidel 2005), and relate the relative growth of galaxies and BHs. Finally, we will uncover obscured and

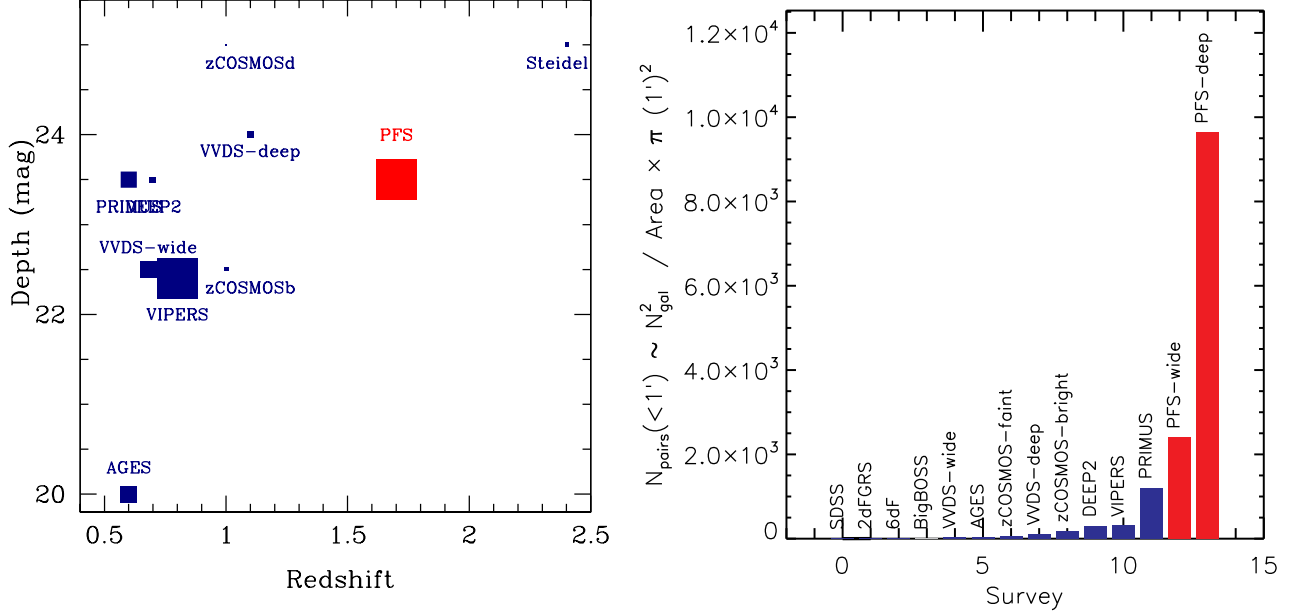


FIG. 23.— *Left*: Depth versus redshift for existing and planned large redshift surveys with $z < 2.5$. The symbol size represents survey area. Each survey is placed roughly at the median redshift of the survey. PFS occupies a unique position in this parameter space, as it is the *only* large-area survey capable of filling in the redshift regime between $1.5 < z < 2$. *Right*: This figure shows the number of spectroscopic pairs separated by less than one arcminute. It highlights the power of PFS to (i) study small-scale clustering on the group scale and (ii) probe the gas distribution in galaxy halos using absorption line probes. Fiber-based spectroscopic surveys doing only one pass over the sky suffer from the fiber collision limitation and cannot access small-scale pairs. “PFS-wide” here is the BAO survey described in §2, while “PFS-deep” is the survey here.

low-luminosity active galaxies using emission-line diagnostics in the $1 < z < 2$ survey.

5. The Epoch of Reionization, Ionized Bubbles: For the first time, we will constrain the topology of ionized bubbles at $z \sim 7$ with a complete spectroscopic sample of LAEs. Current surveys (e.g., Ouchi et al. 2010) have shown the promise of using the mean $\text{Ly } \alpha$ profile shape as a tracer of neutrality, but the small samples offer no information on large-scale spatial variations (Fig. 25). We will exploit the $\sim 9,000$ LAEs from our PFS survey to search for variations in $\text{Ly } \alpha$ profiles over scales of 10 Mpc, comparable to the expected size of typical ionized bubbles. We will calibrate the intrinsic $\text{Ly } \alpha$ line shape using a critical sample of LAEs at $z \sim 2.2 - 2.4$, for which we will have robust systemic redshifts from [O II].

6. The Epoch of Reionization, Neutral Fraction: We will utilize the evolution of the $\text{Ly } \alpha$ luminosity function (Fig. 25) (e.g., Ouchi et al. 2010) and the complementary measure of the fraction of galaxies with $\text{Ly } \alpha$ emission, with unprecedented large samples of LAEs and LBGs, respectively (Stark et al. 2011). This dual approach will allow us to calibrate possible intrinsic evolution in the $\text{Ly } \alpha$ luminosity function arising from changes in the comoving star formation density. Linking emission line demographics to LBG colors will address possible effects of dust extinction. The resulting decline in the visibility of $\text{Ly } \alpha$ over $6 < z < 7$ will then be interpreted in terms of a change in the neutral fraction using appropriate models (e.g., McQuinn et al. 2007). We will obtain complementary constraints on the neutral fraction using the Gunn-Peterson troughs of $z \sim 6 - 7$ quasars.

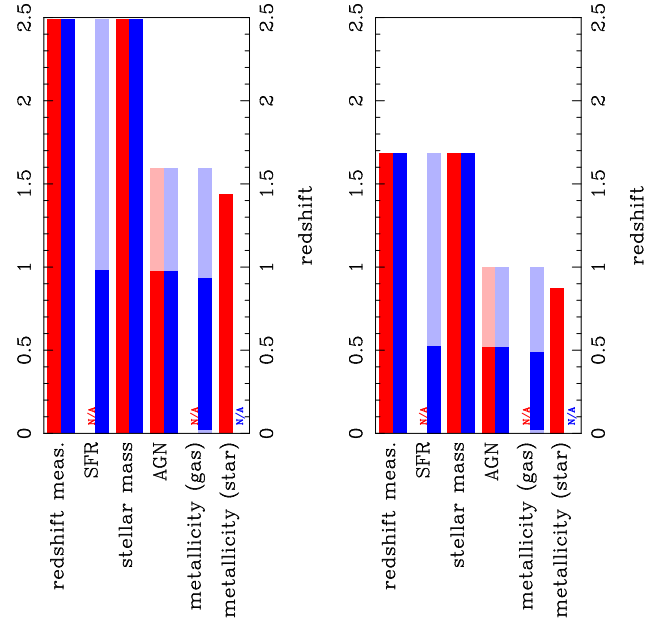


FIG. 24.— Redshift range over which various spectroscopic properties of galaxies can be tracked assuming a flux-limited survey down to $J_{\text{AB}} = 23.4$ mag. *Left*: The capabilities of PFS with the full wavelength coverage (optical+NIR). *Right*: The same, but with only the blue+red coverage. The dark and light areas show the redshift range where a primary and secondary set of spectral features will be available for galaxies with masses above a characteristic value (M^*). Passive and star forming galaxies are marked in red and blue, respectively.

We wish to strongly emphasize the power of the wide wavelength coverage of PFS. The NIR arm allows us to measure the [O II] line (and thereby reliable redshifts) out to $z = 2.4$ (Fig. 24). The NIR arm thus opens the opportunity to study

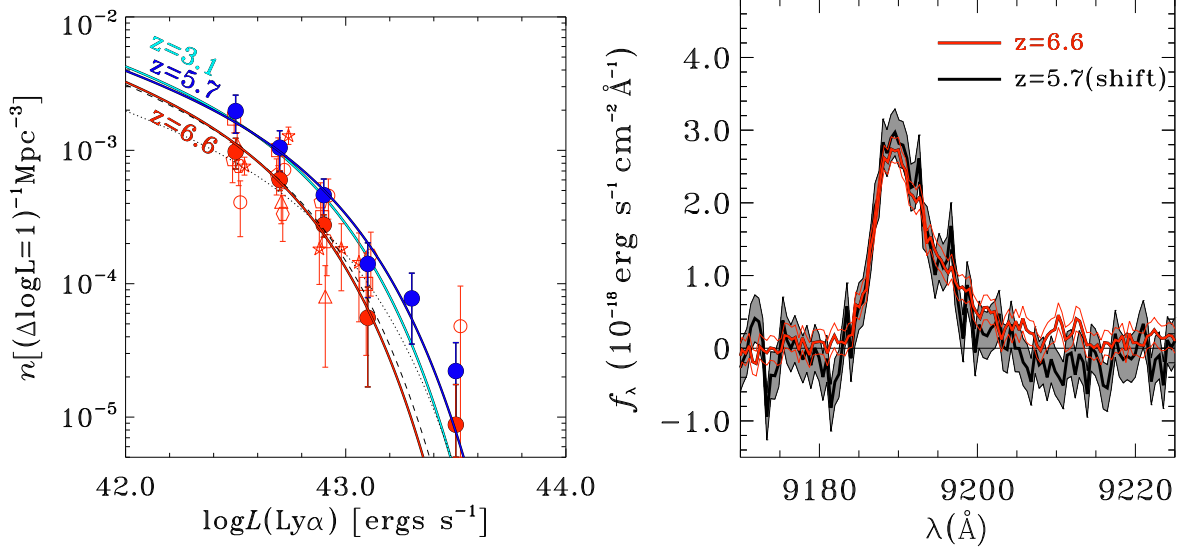


FIG. 25.— *Left*: Evolution of Ly α luminosity functions from $z = 3.1$ to $z = 6.6$ (Ouchi et al. 2010). Red filled circles are the best estimates for $z = 6.6$ LAEs, and the red solid line is the best-fit Schechter function of $z = 6.6$ LAEs. Blue filled circles and solid line are data points and the best-fit Schechter function, respectively, of the $z = 5.7$ LAEs. For reference, the cyan solid line is the best-fit Schechter function of the $z = 3.1$ LAEs (Ouchi et al. 2008). We will use evolution in the Ly α luminosity function to search for the signature of reionization as absorption from neutral hydrogen systematically suppresses Ly α emission. *Right*: Evolution of Ly α line profiles in existing data (Ouchi et al. 2010). Red and black thick lines represent composite spectra of LAEs at $z = 6.6$ and 5.7 , respectively. For comparison of line shapes, the composite spectrum of the $z = 5.7$ LAEs is redshifted to $z = 6.6$, and scaled by an arbitrary factor. One sigma errors of the composite spectra are shown with thin red lines for $z = 6.6$ LAEs and gray shading for $z = 5.7$ LAEs. We hope to do seven times better in any deg² patch of the sky by stacking the much larger sample of objects in the PFS survey.

the crucial, and largely unexplored, epoch of $1 < z < 2$. It allows us to trace galaxy populations from low to high redshifts with no gaps. There will be no redshift desert with this spectrograph. As illustrated in Fig. 24, we will have access to many important emission and absorption features over an unprecedented range of redshifts, which will enable new and important science. We will cross-calibrate star-formation and metallicity indicators such as [O II] and H α ; both can be observed to $z \approx 1$. We can also study the physics of Ly α emission via its profile shape by obtaining accurate redshifts from the [O II] line for thousands of LBGs with $2.1 < z < 2.4$.

4.2. Simulated Data

In this section we will show that our main science goals are achievable. Our exposure times will be 20 min, after which we can plan to leave our brightest targets, thanks to the rapid fiber repositioning time. For the faintest $1 < z < 2$ targets ($J_{AB} = 23 - 23.4$ mag) we will spend three hours per galaxy. The integration times for higher redshift sources will range from one to sixteen hours. We have generated realistic simulated spectra to determine what types of measurements are feasible as a function of continuum and line luminosity. Specifically, we take the instrument specifications and reasonable assumptions for the properties of the sky emission and our ability to model it. We demonstrate that with our chosen exposure times, we can accomplish our science goals of (1) measuring emission line fluxes and line-widths and thus redshifts and (2) measuring absorption-line redshifts. Finally, we explore a variety of assumptions about sky brightness and scattered light from the point of view of survey design.

Our model for the throughput of the spectrograph includes the quantum efficiency of the chips, light-losses at the fiber due to seeing, losses in the fiber and fiber coupling, reflectivity of the Subaru primary mirror and transmission of the

corrector, throughput of the camera and collimator (including vignetting) and dichroics as a function of wavelength, the grating transmission, and the atmospheric transparency. The spectral simulator models the two-dimensional distribution of source and sky photons on the chip, then collapses along the spatial direction to produce simulated one-dimensional spectra and the corresponding error arrays. The noise calculation includes shot noise from the source, sky emission lines, and sky continuum, as well as readnoise, dark current, and thermal background.

The most important, and most challenging, aspect of our simulations involves modeling the sky, which dominates the noise in the red and NIR arms. Our treatment is the same as that outlined in §2 and assumes that we can measure the overall sky spectrum at a given time at the 0.5% level. This requirement is theoretically possible, given Poisson errors, but technically challenging in practice. For instance, (Bolton et al. 2012) achieve $\sim 1\%$ sky subtraction in the red in BOSS. Relative to our system, the BOSS fibers are short and move very little, and BOSS takes calibration frames at every pointing. On the other hand, the BOSS spectrographs move with the telescope, and thus suffer flexure and temperature variations that do not impact the fixed and temperature-controlled PFS spectrographs. Furthermore, the native PFS spectral resolution is higher, which will facilitate sky subtraction. Accordingly, an additional Gaussian random deviate with an amplitude that is 0.5% of the sky flux, is added to the error budget of each pixel, with bright sky lines bleeding over into adjacent pixels. Finally, we assume that 0.5% of the total flux in the sky is spread across the detector as a smooth background and include the relevant shot-noise. We revisit these assumptions later in the section, and show that our survey is robust even if our assumptions for each are overly optimistic.

The spectra shown here are inverse variance weighted and

smoothed to $R = 400, 300, 300$ for the blue, red, and NIR arms respectively (Figs. 26, 27, and 28) for viewing purposes only. When we examine [O II] emission lines, we instead use $R \approx 1200$ to properly resolve emission lines with $\sigma = 100 \text{ km s}^{-1}$. A large fraction of the spectrum is eaten by night sky lines; these low resolution spectra give a convenient representation of their information content. For reference, the unsmoothed spectra are shown as well. All of our assumptions are summarized in Table 11.

In the following, we show simulation results for four different templates: a blue and red galaxy at both $z \approx 1.7$ and at our redshift limit of $z \approx 1.9$, a Lyman-break galaxy (LBG), and a QSO. The galaxy templates are stellar population model fits to NEWFIRM Medium-Band Survey photometry for galaxies spanning the color-magnitude diagram. These fits, from the code EAZY (Brammer et al. 2008) include emission lines. Since the region surrounding the 4000\AA break and the [O II] line is of particular importance, we splice in spectra with considerably higher spectral resolution between $3700\text{-}4500\text{\AA}$. We splice a stack of DEEP2 galaxies from Schiavon et al. (2006) into the red galaxy template. For the blue galaxy splice, we use a model star-forming galaxy with emission-line EWs based on Kriek et al. (2011). These are shown in Fig. 26 at our detection limit of $J = 23.4 \text{ mag}$ at $z \approx 2$, observed in a 3hr integration with PFS.

The LBG template is based on the spectral energy distribution from Reddy et al. (2012). We add emission lines to match the EWs in Shapley et al. (2003); the objects shown in Fig. 27 in the bottom panel are representative of objects with high Ly α EW in their sample. From these simulations it is clear that we will be able to detect both Ly α down to our detection limits and interstellar absorption features in our brighter targets. Finally the QSO spectra are generated from the composite spectrum from Van den Berk et al. (2001).

4.2.1. Continuum Redshifts

One of our greatest challenges comes in measuring absorption-line redshifts for $z \approx 2$ galaxies at our flux limit. In practice, we expect that many of our targets will have some [O II] emission, since most red galaxies have low EW emission lines (e.g., Ho et al. 1997; Yan et al. 2006). Nevertheless, there will certainly be passive red galaxies for which the 4000\AA break will be the primary source of redshift information. It will be measured in the NIR arm. While we do not yet have full redshift measurement software in place for our spectral simulations, we use the S/N in the 4000\AA break as a proxy for our ability to measure a reliable continuum-based redshift. We assume that with a $S/N > 5$ in the break itself we will be able to measure a redshift (e.g., Tonry & Davis 1979). Note that this is a crude proxy for a redshift measurement: in principle we want a code that can uniquely identify the 4000\AA feature. On the other hand, we expect the task will be eased by the presence of some [O II] emission in most of our real sources.

Fig. 29 (top) demonstrates the expected S/N in the 4000\AA break as a function of apparent J -band magnitude and redshift, for both a typical red and blue galaxy. These figures reveal a number of important things. First, even at our flux limit, we expect to achieve redshift success ($S/N > 5$ in the 4000\AA break) for both red and blue galaxies, independent of their break strength. Second, because we are selecting galaxies in the J -band, the blue galaxies are considerably brighter at the 4000\AA break than the red galaxies for the majority of

the redshift space. Thus, although their break strengths are weaker, there is still higher S/N in the continuum for these templates. Third, because the red galaxies have a relatively steep spectrum, their break strength actually increases as the break shifts into the J -band at higher redshift at a fixed apparent magnitude.

We have made a few critical assumptions in modeling the background, particularly in the NIR, which we will now relax. We assumed that the scattered light fraction is only 0.5% of the sky photons (as is the specification for PFS), and that we can subtract the sky to within 0.5% as well. We investigate our redshift success if either the scattered light fraction is larger or we are unable to perform such reliable sky subtraction.

First, we assume that we can only achieve 2% sky subtraction, rather than the specified 0.5%. In practice, this assumption has little impact on the S/N calculations for a broad feature like the 4000\AA break, because we inverse-variance weight the pixels and mask strong sky features anyway.

Changing the scattered light fraction does make a difference. Rather than taking 0.5% of the power in the sky and spreading it uniformly over the entire chip, we take 5% of the power in the sky. Since we increase the number of photons in the continuum with this test, we directly degrade our S/N . To calculate the level of degradation when we increase the scattered light fraction, we first note that over the J -band, the continuum photons (both from true sky continuum and from thermal background) contribute $\sim 6\%$ of all background photons. The rest come from sky lines. We also note that $\sim 60\%$ of the scattered photons fall on science pixels. For a scattered light fraction of 5%, we will increase the background continuum level by 60% of 5% or 3%, or a factor of 1.5. This gives a $\sqrt{1.5} \approx 20\%$ reduction in S/N due to the increased continuum level. With this degradation, we can still expect to achieve redshift success based on our simulations. However, our ability to measure more detailed spectral properties of the galaxies would suffer. Thus, our proposed program will be feasible even if the assumptions about scattered light are overly optimistic.

4.2.2. Galaxy Physical Parameters

Our spectra will facilitate more than just a redshift survey, as Fig. 26 demonstrates. With the typical spectra at $z \approx 1.5 - 1.7$ shown here, we can achieve a $S/N > 5$ in broad-band spectral indices (Fig. 29), allowing us to measure the continuum shape and thus constrain stellar populations. For a $z \approx 1.5$ galaxy, we will even be able to detect indicators of the stellar abundances from stellar absorption features (Fig. 26). Finally, we will have access to emission features such as [O II] and higher-order Balmer lines (including $H\beta$ at $z = 1.6$) that will allow us to constrain the star formation rate and the internal extinction (see next section). These simulations motivate our three-hour total integration times.

4.2.3. Emission Line Fluxes and Widths

To test our ability to detect and characterize emission-line objects, we generate a picket-fence of emission lines across the entire waveband, similarly to the discussion in Section 2.2.1. We generate [O II] models as a pair of Gaussians at $\lambda, \lambda 3726.2, 3728.9$, with a ratio of 2 : 1. The pair of lines are assumed to have the same intrinsic width, and we generate two models with $\sigma_{\text{gas}} = 100$ and 200 km s^{-1} respectively. We also generate Ly α models as skewed Gaussians.

Many of our science cases depend on our ability to measure not only the line centroid of emission lines but also the line

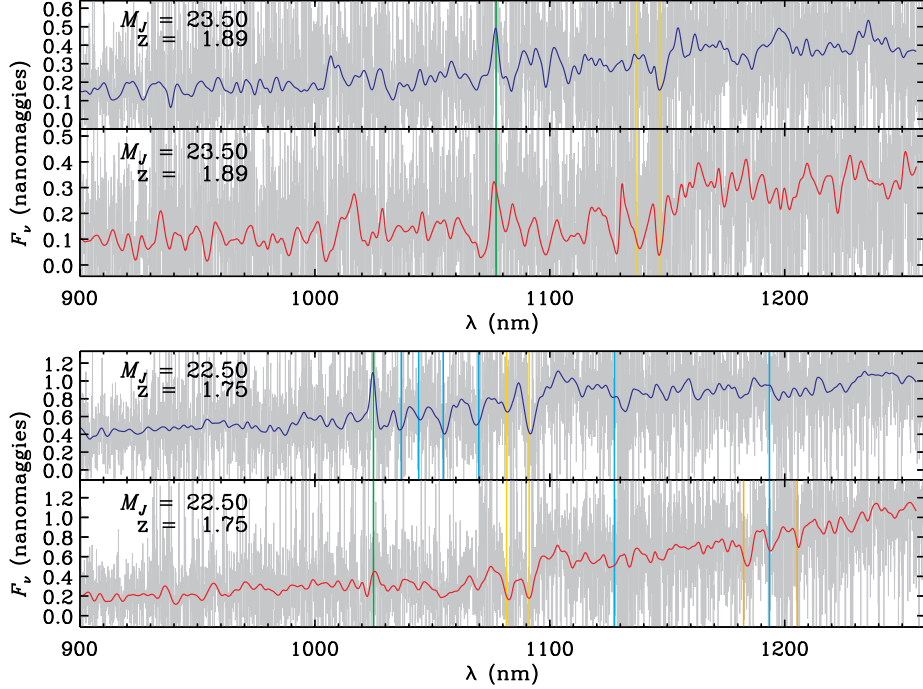


FIG. 26.— Simulated spectra as observed in three-hour integrations (see text) demonstrating the power of PFS. The spectra are plotted in units of “nanomaggies”, a unit of flux used by the SDSS, defined such that one maggie is the flux from an AB= 0 object, 3631 Janskys. Thus 1 nanomaggie is equivalent to an apparent AB magnitude of 22.5, 3631×10^{-9} Jy or 3.631×10^{-29} erg s $^{-1}$ cm $^{-2}$ Hz $^{-1}$. The grey lines show the observed spectra, while the red and blue overlotted spectra are binned to a resolution of $R = 400, 300, 300$ in the blue, red, and NIR arms respectively. The green line indicates the position of the [O II] doublet, the blue lines indicate the higher-order Balmer lines, the gold lines show the Ca H+K lines, and the orange lines indicate the G-band and Fe4383. The spectral templates are partly based on stellar population synthesis models of NEWFIRM Medium Band Survey galaxy photometry, which provides some constraint on the emission line equivalent widths. In the 4000 Å break region, we splice in a higher-resolution composite spectrum from the DEEP2 survey (Schiavon et al. 2006). We show total integration times of three hours. From top to bottom, we show the blue and red galaxy pair with $J_{AB} = 23.5$ mag at $z = 1.89$ and the same pair with $J_{AB} = 22.5$ mag at $z = 1.75$. In this case, we will have very rich spectral diagnostics to determine the physical properties of the galaxies.

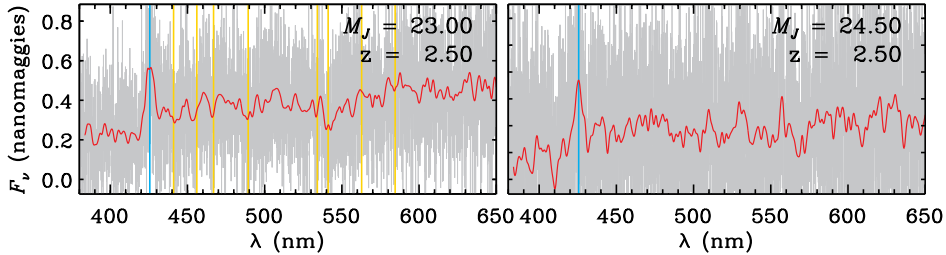


FIG. 27.— Star-forming galaxies selected as a U -band dropouts with $J_{AB} = 23, 24.5$ mag, as observed in a three-hour total integration with PFS. As above, the grey lines are the observed PFS spectra, while the red overlotted spectra are at effective resolution of $R = 400, 300, 300$ in the blue, red, and NIR arms respectively. The cyan line denotes Ly α . The gold lines demarcate strong interstellar features Si II λ 1260, O I+Si II λ 1303, C II λ 1334, Si IV λ 1398, Si II λ 1526, C IV λ 1546, Fe II λ 1608, and Al II λ 1670. The spectral energy distribution is based on a spectral synthesis model from Reddy et al. (2012), with emission line EWs based on Shapley et al. (2003). For the brighter targets (left) we will detect ISM absorption lines in individual spectra, while we will stack fainter targets (right).

widths and fluxes. For [O II] lines with a combined flux of $F = 10^{-17}$ erg s $^{-1}$ cm $^{-2}$, we find that we can recover the total flux within $< 20\%$, and the line-width to within $< 40\%$. This is true over the full extent of the blue and red arms, and for $\sim 75\%$ of the NIR arm (the remainder are cases where the [O II] overlaps directly with sky emission lines). We recall that this flux is typical of [O II] emitters at $z \approx 2$ (Takahashi et al. 2007). We repeat the experiment for the Ly α emission lines with $F = 0.8 \times 10^{-17}$ erg s $^{-1}$ cm $^{-2}$, which is again typical of LAEs at $5 < z < 7$. We recover Ly α fluxes and linewidths at the 10% level in the blue arm. In the red arm we can only recover linewidths at the 20% level. However, these

limits are for individual objects; we will do better using stacking. Thus, we will do a factor of ~ 20 better at measuring the composite Ly α profile of high redshift emitters. Finally, we attempt linewidth measurements for our QSO spectra. Even with half-hour integration times at our magnitude limit, we expect to measure the CIV linewidth with 40% precision. The S/N of the spectra will not compromise our goal of measuring spectral shapes and estimating SMBH masses from these spectra. While there are well-known uncertainties in calculating reliable SMBH masses using broad UV lines, we will be in a good position to compare the SMBH masses derived from different emission lines observed in the same spectra (e.g.,

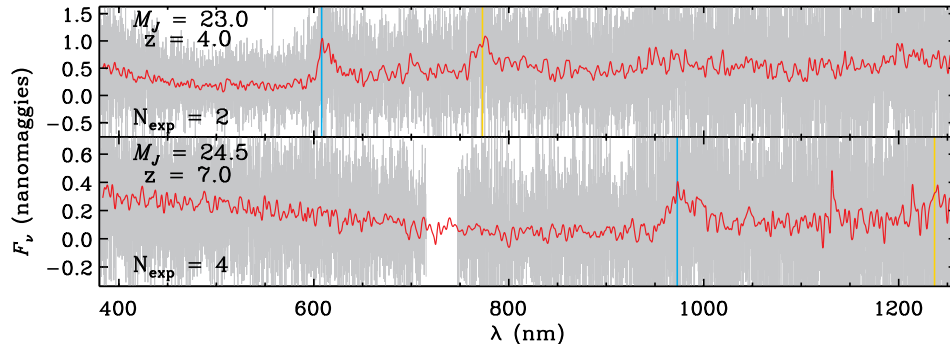


FIG. 28.— Two QSO spectra. As above, the grey lines are the observed PFS spectra, while the red spectra are at effective resolution of $R = 400, 300, 300$ in the blue, red, and NIR arms respectively. The top one assumes a 30 min total integration time, as we will have in the BAO survey described in Section 2, while the bottom one assumes a full hour of total integration time as is proposed for the QSOs observed in the galaxy-evolution survey described in this Section. In both, the cyan line marks the position of Ly α while the gold line denotes CIV.

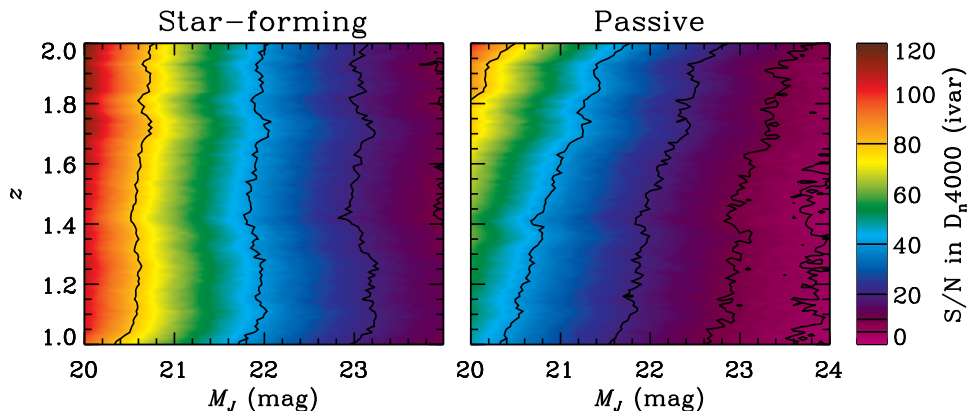


FIG. 29.— *Top*: The S/N ratio in the 4000 Å index as a function of J_{AB} -band magnitude and redshift. The color scale indicates S/N , as indicated by the scale bar, while the contours denote $S/N = 5, 10, 20, 40, 80$. Here we assume a fiducial scattered light fraction of 0.5%, and that we can subtract the sky to within 0.5% as well.

Shen et al. 2008).

4.3. The Survey Fields

Over the coming years, the Hyper Suprime-Cam on Subaru will perform an ambitious imaging survey in *grizy*. The survey will have three components with different depths. That of most interest to us is the HSC Deep layer, which will reach a 5σ depth of $i \approx 27.2$ mag. There is also narrow-band imaging planned that will be of crucial importance in selecting Ly α emitters at high redshift. J -band imaging provides the cleanest method for selecting a sample of redshift $1 < z < 2$ galaxies for study with PFS. From the PFS spectroscopy, our strongest continuum redshift constraint comes from the 4000 Å break, which falls in the NIR arm (the J -band) for $z \gtrsim 1.5$, and thus purely from S/N considerations, we select targets in the J -band for the $z < 2$ survey. Selection down to $J_{\text{AB}} = 23.4$ mag will survey galaxies with $M^* \gtrsim 10^{10} M_\odot$ (§4.6).

To select a complete sample, we should have imaging ~ 1 mag deeper than the magnitude limit (e.g., Newman et al. 2012). For $z < 2$ selection, we want $J_{\text{AB}} = 24.5$ mag photometry over 16 deg^2 . For the high-redshift star-forming galaxies, the ideal photometry would have $J_{\text{AB}} = 26$, $H_{\text{AB}} = 25.6$, $K_{\text{AB}} = 25$ over 16 deg^2 , and a bit deeper over the HSC 3.5 deg^2 Ultradeep area. The fields we have chosen (*XMM-*

LSS, *ELAIS-N1*, and *DEEP2-3*) all have infrared coverage now to $J_{\text{AB}} = 23.4$ mag. Ongoing and planned imaging including *UKIDSS-DXS*, *VISTA-VIDEO*, and *COSMOS* cover 6.5 deg^2 to $J_{\text{AB}} = 24.5$ mag. Thus, at the absolute minimum, we need an additional 10.5 deg^2 to $J_{\text{AB}} = 24.5$ mag and $K_{\text{AB}} = 23.5$ mag. The most efficient way to achieve this goal at the present time is *VISTA* - assuming 9h per band per deg^2 , we would need ~ 190 hrs or thirty *VISTA* nights. This represents a large, but not prohibitive, investment. To achieve the full depths of $J_{\text{AB}} = 26$, $H_{\text{AB}} = 25.6$, $K_{\text{AB}} = 25$ over 16 deg^2 and the deeper limits in the Ultradeep area would require a 1500 hr program, which is more difficult.

Our fields have been selected to maximize overlap with multiwavelength data sets, including X-ray data to study accretion activity and mid-infrared data to probe obscured star formation and accretion. In particular, we are excited about the prospect to use *Spitzer* and *Herschel* data for measuring complementary star formation rates to those derived from emission lines or continuum fitting. Between the *SERVS*, *SWIRE*, and *COSMOS* surveys, there is *Spitzer* data to at least $4 \mu\text{Jy}$ at $3.6 \mu\text{m}$ in the same 9 deg^2 with the NIR coverage. There is U -band data with $\text{AB}=26$ mag depth from CFHT that we will use in the selection of high redshift star forming galaxies. We also have good overlap with the *HerMES* fields (*HerMES* Collaboration et al. 2012). By the same

token, our survey fields will provide natural targets for ALMA and/or CCAT.

4.4. Survey Design and Target Selection: Continuum-selected $z < 2$ Survey

As we discuss the time needed for each component, we will use the natural unit of fiber-hours (we will also convert to night-equivalents, but note that these are misleading since we plan to observe all types of targets at all times for efficiency). In a 100-night survey, assuming 2000 science fibers and 6 hr nights, we have 1.2 million fiber hours.

Our primary goal for the $z < 2$ survey is to study the evolution of the $\sim L^*$ galaxy population, which leads to the following choices:

- 1. Magnitude limit, with color selection:** Based on our spectral simulations, we can expect to reach a $S/N > 5$ in the 4000 Å break in 3 hr exposures at our limiting magnitude of $J_{AB} = 23.4$ mag (Fig. 29). With this magnitude limit, we expect to probe masses as low as $10^{10} M_{\odot}$ at $z \approx 2$ based on the NEWFIRM Medium-Band redshift survey (Fig. 30), although we are only complete for stellar masses $\gtrsim 10^{11} M_{\odot}$. We will describe various color selections below. In order to observe the same population at low redshift, we plan to observe all objects to a limiting magnitude of $J_{AB} = 21$ mag. Since we will spend only 20 min per galaxy at these bright limits, we get these 6000 galaxies per deg² essentially for free, and they provide a low-redshift comparison sample (e.g., for comparing H α and [O II]-derived star formation rates).
- 2. Magnitude-limited component:** We propose to perform a purely magnitude-limited survey to $J_{AB} = 23.4$ mag, with the same exposure times as outlined above, in 2 PFS pointings. With two independent pointings, we will sample different large-scale structures, and given that we expect ~ 10 clusters with $M > 10^{14} M_{\odot}$ and $z > 1$ in this volume, we expect to sample a range of environments in these pointings. Ideally, this component would be completed early in the survey. This small (82,000 fiber hours or ~ 8 night) investment, includes observations of an additional 24,000 galaxies per deg² over the nominal color-selected survey, that will allow us to tune and understand our color selection in detail in preparation for the main survey. Furthermore, we can investigate rare populations that our color selection may exclude. Finally, the bias of the galaxies used for the cosmology survey may be a strong function of redshift, as it involves a color cut which may select astrophysically distinct populations of galaxies at different redshifts. The bias, and the relationship of the selected galaxies to the full galaxy population, needs to be understood in order to use the sample for cosmological inferences, especially when combining clustering measurements at different redshifts. (Note that the BAO scale itself is actually fairly insensitive to these details, as the bias is scale-independent on these very large scales).
- 3. Area:** The area should be large enough to minimize cosmic variance. In 16 deg² we cover a volume a few tenths that of the SDSS main galaxy sample in a redshift bin at $z \approx 2$, which should sample a fair volume of the

TABLE 8
IMPACT OF COSMIC VARIANCE

9.1	0.02	0.02	0.02	0.03
9.6	0.02	0.02	0.03	0.03
10.1	0.02	0.02	0.03	0.03
10.6	0.02	0.03	0.03	0.04
11.1	0.03	0.03	0.04	0.05
11.6	0.04	0.05	0.06	0.07

NOTE. — The logarithmic error bars on the number density in each logarithmic stellar mass bin ($\log M_{\odot}$; column 1) are shown for four redshift ranges: $1 < z < 1.4$ (Col. 2), $1.4 < z < 1.8$ (Col. 3), $1.8 < z < 2.2$ (Col. 4), $2.2 < z < 2.6$ (Col. 5), assuming a 16 deg² area. The error bars are derived using the method of Moster et al. (2010).

universe. To quantify the level of cosmic variance, in Table 8 we show the expected error bars on the number density of galaxies in mass and redshift bins derived using the method of Moster et al. (2011). Thus over the survey area of 16 deg² our analysis will not be cosmic variance limited.

4.4.1. Color Selection

A major strength of the SDSS was the simple magnitude-limited selection with an easy-to-model selection function. We would like to replicate that ideal to the extent possible, but require a color selection if we want to spend more than half of our time observing galaxies with $1 < z < 2$. We have explored various color-selection techniques to maximize the time spent in the redshift range of interest and outline their strengths and weaknesses here. Note that in addition to the main survey of 16 deg², we require a purely magnitude-limited sample over 2 PFS pointings to be observed early in the survey, which will allow us to calibrate our selection methods. A similar strategy was adopted by DEEP2 (Davis et al. 2003). In Table 9 we show the number of targets by magnitude, number density, and exposure time.

We outline three potential color selections here:

- 1. Photometric redshifts:** As a straw-man, using photometric redshifts is a very appealing strategy, as it utilizes all of the exquisite HSC imaging. We are testing the capability of HSC Deep to measure reliable photometric redshifts. Based on simulations run by M. Tanaka of photometric redshifts from HSC Deep data, the completeness, or the fraction of objects with $z_{\text{spec}} > 1$ that correctly have $z_{\text{phot}} > 1$, is 93%. The contamination, which is the fraction of objects at $z_{\text{spec}} < 1$ that have $z_{\text{phot}} > 1$, is 5%. Our ability to measure reliable photometric redshifts should improve dramatically in the coming years, as we gain access to real HSC data, and take advantage of ongoing redshift surveys in our field (e.g., VIPERS). A major concern with using the photometric redshift is systematic error (for instance, in the template set). We will be measuring photometric redshifts for a population without good spectroscopic coverage, and therefore there is room for significant spectral differences between the templates and the targets. Much more work is needed to deter-

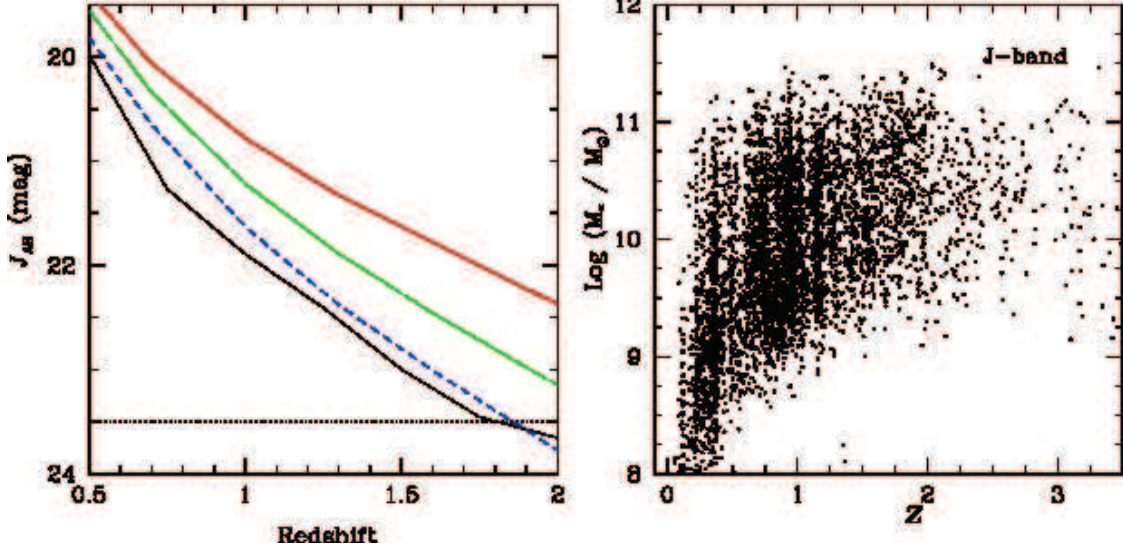


FIG. 30.— *Left*: Illustrative models of galaxies with different evolutionary histories based on Maraston (2005) stellar population models. All models have $\tau e^{-\tau}$ star formation histories, and are normalized to be L^* galaxies today. In red is a red galaxy progenitor with a final mass of $M^* = 6 \times 10^{10} M_{\odot}$. In green is a more typical star-forming galaxy with a final mass of $M^* = 3.4 \times 10^{10} M_{\odot}$ with an extended history, while the blue line is a more extreme star forming system with a final mass of $M^* = 2.3 \times 10^{10} M_{\odot}$. For reference, in black is the mean apparent J -band magnitude of a $3 \times 10^{10} M_{\odot}$ galaxy at each epoch from the K -band selected NEWFIRM medium-band survey. *Right*: Expected stellar mass distribution for our $1 < z < 2$ survey, based on the NEWFIRM Medium Band Survey (Whitaker et al. 2011). We apply a J -band magnitude limit of 23.4 mag, but note that the total number of points in the figure corresponds to a 0.2 deg^2 survey; we will spectroscopically observe 125 times as many objects. Without a redshift selection, a large fraction of the galaxies in a magnitude-limited sample have $z < 1$. The banding in the figure is due to large scale structure; our much larger volume will average over this cosmic variance.

TABLE 9
ALL TARGETS

Mag. (1)	z (2)	Selection (3)	N deg^{-2} (4)	Sampling (5)	Int Time (6)	Area (7)	Fiber Hours (8)
$J_{AB} < 21$	$z < 1$	photoz	6k	0.8	0.3	16	23k
$J_{AB} = 21 - 22$	$1 < z < 2$	photoz	1.5k	0.8	0.3	16	5.8k
$J_{AB} = 22 - 23$	$1 < z < 2$	photoz	8.4k	0.8	2	16	215k
$J_{AB} = 23 - 23.4$	$1 < z < 2$	photoz	12k	0.8	3	16	460k
$J_{AB} < 23.4$	$z < 2$	all	47k	0.8	0.3-3	2.6	82k
$NB387 = 25$	$z = 2.2$	LAE	300	1	2	16	9.6k
$NB816 = 25$	$z = 5.7$	LAE	230	1	5	16	18.4k
$NB921 = 25$	$z = 6.6$	LAE	240	1	5	16	19.2k
$NB101 = 26$	$z = 7.3$	LAE	14	1	6	3.5	0.3k
$i = 24$	$2 < z < 3$	LBG	4.6k	0.4	3	16	88k
$i = 24$	$3 < z < 4$	LBG	840	1	3	16	40k
$i = 25$	$4 < z < 6$	LBG	100	0.1	6	16	4.8k
$z = 26$	$2 < z < 4$	LBG	8k	0.1	16	3.5	45k
$z = 26$	$4 < z < 6$	LBG	4k	0.1	16	3.5	22k
$J < 24$	$3 < z < 7$	QSO	30	1	0.5	1400	21k
$J < 25$	$3 < z < 7$	QSO	100	1	1	16	1.6k

NOTE. — Col. (1): J -band magnitude (AB) or narrow-band magnitude. Col. (2): Redshift range. Col. (3): Selection method. Col. (4): Number of galaxies per deg^2 . For the continuum-selected sources, we have adopted the mean of the number densities from the COSMOS and NEWFIRM catalogs. The LBGs are grouped in redshift with $\delta z \approx 1$. Note that the 1400 deg^2 QSO search will be part of the BAO survey. Col. (5): Fraction of galaxies that we will sample. Col. (6): Integration time (hrs). Col. (7): Survey area (square degrees). Col. (8): Fiber hours.

mine whether photometric redshift selection can provide an unbiased sample selection.

- IRAC CH1-CH2 Selection:** Galaxy spectral energy distributions peak at $\lambda = 1.6 \mu\text{m}$, redward of which is the Rayleigh-Jeans tail. As this feature moves through the IRAC bandpasses (particularly CH1 = $3.6 \mu\text{m}$ and CH2 = $4.8 \mu\text{m}$), the CH1-CH2 color goes through a distinct minimum at $z \approx 0.8$ and then rises monotonically towards higher redshift (Fig. 31 left). A simple cut of CH1-CH2 > -0.1 effectively selects $z > 1.3$ galaxies

(e.g., Papovich 2008). Using the NEWFIRM Medium Band Survey (Whitaker et al. 2011), we find that the completeness, or the fraction of objects with $z > 1$ that are selected by this method, is 64%, while the contamination, or fraction of selected objects that have $z < 1$, is 30%. The numbers are not as impressive as the photometric redshifts, but the selection is easily modeled and relatively free of systematics. There is *Spitzer* data of sufficient depth over \sim half of the 16 deg^2 field.

- griJ* Selection:** Inspired by the DEEP2 color selec-

tion, we have designed an optical/NIR color selection that is effective at removing $z < 0.8$ interlopers. The color region we select is defined by $i - J > 1.15$ or $(g - r) < 0.87(i - J) + 0.196$ and $J_{AB} < 23.4$ mag (Fig. 31 *right*). Again based on the NEWFIRM Medium Band Survey, the completeness (fraction of galaxies with $z > 1$ that we select) in this case is 93%. The contamination (galaxies in the final sample with $z < 1$) is 42%. However, if we look at galaxies in the final sample with $z < 0.8$, the contamination is only 24%. Therefore, this simple color selection, with all bands to be observed, is very promising if we decide to target $z > 0.8$ galaxies. The total number of objects per deg^2 would increase by 37%. These numbers come from the NEWFIRM catalog but change little when we use the COSMOS photometric redshift catalog instead. We view this color selection as a very promising option. In what follows, the numbers assume a perfect cut at $z = 1$, but the appropriate correction would only be an increase of 37% for the number density of continuum-selected galaxies.

All of these selections assume J -band imaging to the desired depth of $J_{AB} = 24.5$ mag for the entire 16 deg^2 field. Should we fail to acquire the additional 7 deg^2 of J -band imaging, we can also use a pure optical-band color selection: $1.405(g-r) + 0.505(r-z) - 2.150(i-y) < 0$, which has high completeness (93%) and 29% contamination for $z > 0.8$, based on COSMOS data. In this way, we can mitigate incompleteness due to including shallow J -band data.

We hope to additionally mitigate contamination through real-time redshift determinations. The main contaminant in a continuum-limited sample is moderate-redshift, intrinsically faint galaxies that are likely strongly star forming and thus have strong emission lines. We should be able to identify their redshifts with a single 20 min exposure, if we can carry out real-time analysis of the spectra. Thus, we can move to another target in < 1 hr, given the fact that the fibers are individually deployable. In addition, we will sharpen our target selection by using the redshift information from the cosmology survey, and the VIPERS spectroscopy, which overlaps with our fields. Finally, with our magnitude-limited component, we will work to understand our selection bias.

4.4.2. Target Sampling

We must also make a scientific choice about sampling. If we sparsely sample the galaxy population, we can cover a wider area more quickly, and still sample the average properties of the population. However, we will lose information on small scale clustering (Fig. 23). Specifically, the PFS survey will allow accurate measurements of the evolution of the abundance and clustering of galaxies as a function of stellar mass and of the galaxy-galaxy lensing signal (utilizing the imaging from the Hyper Suprime-Cam survey), from $1 \leq z \leq 2$. These results can be used to constrain the evolving relation between the stellar mass of galaxies and the mass of the halos in which they reside. To investigate how well we need to sample galaxies in our survey in order to measure this evolution, we have generated mock catalogs using the semi-analytical model of De Lucia et al. (2006), which is based upon the dark matter halo merger trees drawn from the Millennium simulation (Springel et al. 2005). We have considered four redshift bins of $\Delta z = 0.3$ and used bins in stellar mass of $\Delta \log M_* = 0.3$ each.

Fig. 33 shows the fractional error in the projected correlation function w_p on 100 kpc scales for sampling rates of 30, 50, and 100%. On the smallest scales the errors are dominated by the number of pairs of galaxies expected at a given separation (thus benefiting from increased sampling), while on the largest scales, the errors are dominated by sample variance. We can see that reaching sampling rates $\sim 80\%$ is important for the errors, while for higher levels of completeness we get diminishing returns. In practice it is challenging to achieve higher levels of completeness anyway, so we adopt 80% sampling.

In a similar manner we would also like to simulate the galaxy-galaxy lensing signal expected around the PFS galaxy sample, using the redshift distribution of sources from the HSC imaging survey. We will model the galaxy clustering results, the stellar mass function measurements, and the galaxy-galaxy lensing results in the framework of a halo occupation distribution model (see e.g., Leauthaud et al. 2012). The joint analysis of such data with realistic errors can be used to judge the sampling requirement for the galaxy evolution component of the PFS survey.

4.4.3. Summary

Taking 80% sampling, we plan for a total of 69 nights, or 704,000 fiber-hours, for this component of the survey, assuming 3 hrs per galaxy in the faintest half-magnitude bin. We additionally include a magnitude-limited component over 2.6 deg^2 that adds 82,000 fiber hours (~ 8 nights). In Fig. 30, we show that we will be able to observe galaxies with masses $M > \sim 10^{10} M_\odot$ at our redshift limit, allowing us to study the progenitors of L^* galaxies today. Thanks to the J -band selection, we will be sensitive to the red sequence even at $z \approx 2$, as shown in Fig. 32. The PFS survey is compared in redshift, depth, and area to other existing and upcoming surveys in Fig. 23. Our survey is designed to explore a hitherto unknown epoch in cosmic history, at the time when the bulk of the stellar mass in galaxies was assembled.

4.4.4. Uniqueness of the PFS Survey

As we plan for the PFS survey, many powerful NIR multi-object spectrographs are now coming online (e.g., MOSFIRE on Keck). When the PFS survey begins, large samples of $1 < z < 2$ galaxies will already be observed. What will make PFS unique? There are two aspects. The first aspect is volume. Thanks to the large field-of-view and tremendous multiplexing capability of PFS, we will achieve both high sampling and a large volume, allowing us to study the importance of environment from small groups up to Mpc scales and allowing for large samples of foreground/background pairs for absorption studies. The second is our wide wavelength coverage, which allows us to study both the rest-frame optical and rest-frame UV properties of these galaxies at one time. It is conceivable that earlier surveys will have observed a few thousand galaxies with such wide wavelength coverage when the PFS survey begins (e.g., Steidel et al. 2003); we will study half a million galaxies. The wide area of our survey, combined with the measurements of weak lensing and clustering, will allow us to link the evolution of galaxies with the evolution of dark matter halos. Furthermore, the large numbers will allow us to study spectroscopic properties of galaxies in fine bins in stellar mass, redshift, star formation rate, and environment over the full range of our survey.

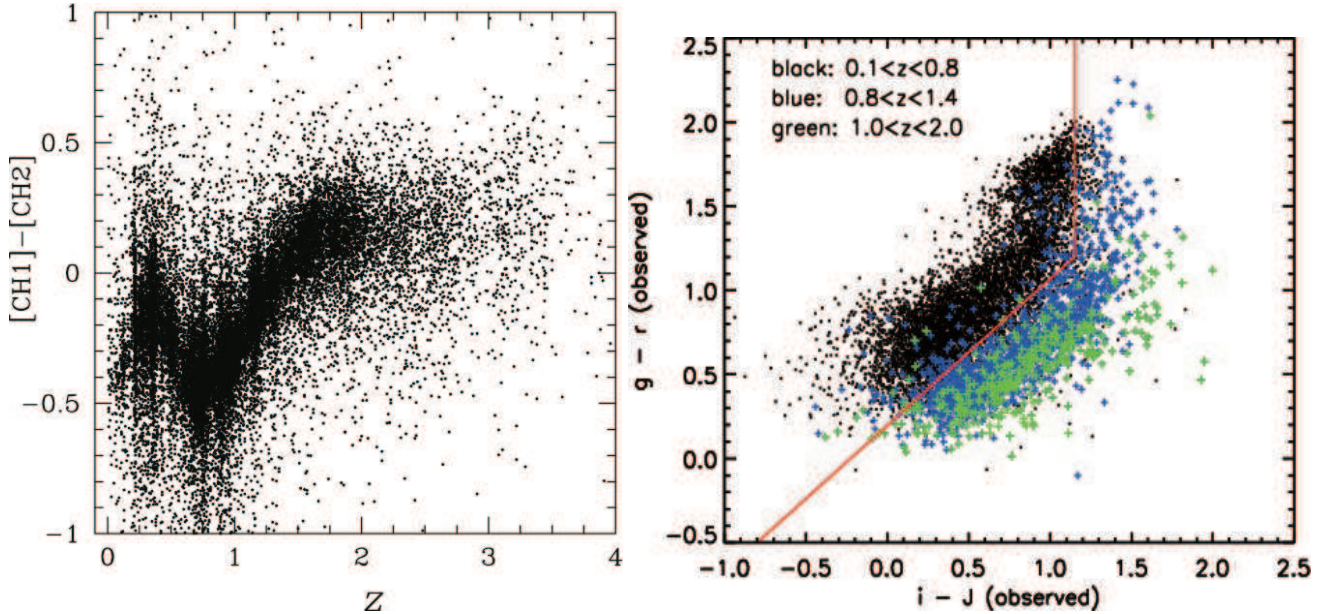


FIG. 31.— *Left*: The dependence of galaxy *Spitzer*/IRAC CH1-CH2 ($3.6 - 4.8\mu\text{m}$) color on redshift. Galaxies are from the NEWFIRM Medium Band Survey, and IRAC data have $1\mu\text{Jy}$ depth. The structure is due to the $1.6\mu\text{m}$ peak in galaxy spectra moving through the CH1 band. *Right*: The *griJ* color selection, where galaxies are from the COSMOS survey. We select galaxies with $i - J > 1.15$ or $(g - r) < 0.87(i - J) + 0.196$; the selection is highly complete ($\sim 90\%$) while the contamination is only $\sim 20\%$ for $z < 0.8$.

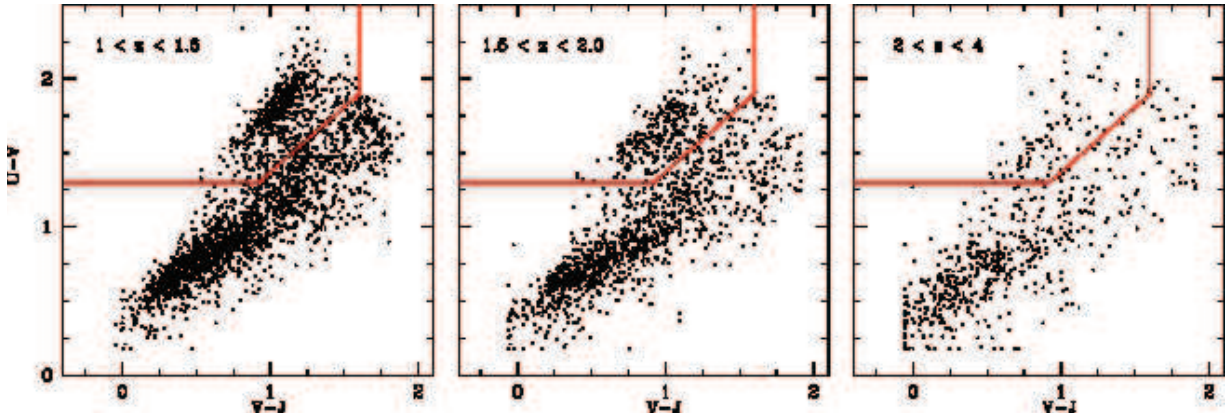


FIG. 32.— Rest-frame color-color plots of the NEWFIRM Medium Band Survey catalog, in the redshift bins indicated and with the J -band cut of 23.4 mag. In red are the color cuts used to define the red sequence by Williams et al. (2009). It is clear that we will sample the red sequence all the way to $z \approx 2$.

4.5. Survey Design and Target Selection: Galaxies at Cosmic Dawn

At higher redshifts, we wish to study the evolution in the star-forming population out to $z \approx 7$, and use this population as a tracer of cosmic reionization. While L^* -progenitors are very faint at these redshifts, we will find them via the Ly α emitter population. We will study more massive star-forming galaxy populations selected via their continuum colors.

4.5.1. Survey Design and Target Selection

The characteristics of the instrument that are important for the high-redshift component include: (1) the high multiplexing of 2000 science fibers (with 400 fibers devoted to sky); (2) the wide field-of-view (1.3 deg^2); (3) sensitivity between $3800 - 12600\text{\AA}$, (4) quick redeployment of fibers between exposures, (5) accurate and stable positioning (over a period of hours), and (6) stable fiber throughput.

In particular, for the high-redshift science case, the wide-area survey enabled by the PFS instrument allows us to cover both a high dynamic range in galaxy properties and cover a wide range of environments. Over our uniform 16 deg^2 survey, we expect to find 60,000 $z > 2$ galaxies, with those at $2 < z < 4$ brighter than $i_{\text{AB}} < 24$ and those at $z > 4$ reaching fainter magnitudes $i_{\text{AB}} < 25$. The large area will also allow us to observe multiple ionized bubbles in the IGM at $z \approx 7$, probed by Ly α emitters. The size of the ionized bubbles may be as large as ~ 1 degree at the end of the reionization epoch (McQuinn et al. 2007).

The majority of the high- z sample will be selected via photometric redshift selection using *ugrizyJHK*+IRAC when available ($M_{\text{gal}} > 10^{10} M_{\odot}$). Photometric redshift selection will deliver a smooth distribution in $N(z)$ (Fig. 34), but may miss some targets. Therefore, we will also target galaxies that are selected via standard three-color techniques but not selected via their photometric redshift. For the sake of simplic-

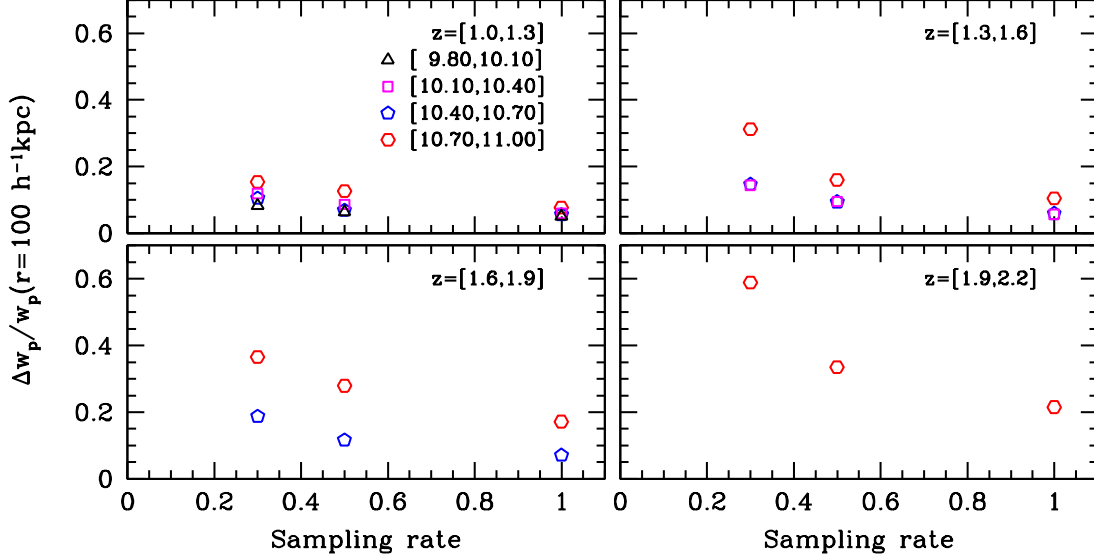


FIG. 33.— We plot the fractional error in the projected correlation function w_p at 100 kpc scales, as measured from semi-analytic models to match the PFS selection. The measurements are made in four redshift bins, with different symbols corresponding to different stellar mass bins, as indicated. We see that the uncertainties improve substantially as sampling approaches $\sim 70 - 80\%$, after which we reach diminishing returns.

ity we will refer to all continuum-selected targets as Lyman break galaxies (LBG hereafter).

The second component to the high- z galaxy survey is the spectroscopic followup of Ly α emitters (LAE) selected from the HSC Deep and Ultradeep narrow-band imaging. The narrow-band filters in the Ultradeep survey are $NB387$; $z = 2.2$, $NB816$; $z = 5.7$, $NB921$; $z = 6.6$, and $NB101$; $z = 7.3$. In the Deep survey, we will have imaging in $NB387$, $NB816$, and $NB921$. This technique provides the most certain way to identify the low-mass galaxies that likely grow into L^* galaxies today (Shimasaku et al. 2004).

Here, we provide specific details regarding the target selection that varies as a function of redshift. The exposure times are chosen to achieve a S/N of ~ 3 per resolution element, assuming $R \sim 400$ in the red continuum of the typical galaxy in each subsample, as justified below.

1. At $2 < z < 4$, we will target the bright end of the LBG luminosity function down to $i_{AB} \approx 24$ uniformly over the full 16 deg^2 survey area. We will observe sources brighter than L^* , with masses $M^* > 10^{10} M_\odot$, typically $M^* \approx 10^{11} M_\odot$ (see, e.g., Cucciati et al. 2012). Existing u -band imaging from the CFHT archive reaches 26 AB mag, which is deep enough to detect the strong drop in flux shortward of Ly α for low- z dropouts. With these data, we can identify high- z candidates down to $i_{AB} \approx 24$. If we want to study galaxies in $\delta z = 0.5$ redshift intervals with ~ 1 mag (or ten $10^{0.2} M_\odot$) bins, as well as in bins of galaxy type and environment with at least ~ 200 galaxies per bin, then we require $\sim 8,000$ targets.

Over 16 deg^2 , we do not expect to be cosmic variance limited. At $\langle z \rangle = 2.5$ the cosmic variance uncertainty in the stellar mass function will be 0.02 dex, while at $\langle z \rangle = 3.5$ it will be 0.02 dex and 0.08 dex for $\log M^* = 10.25 / M_\odot$ and $\log M^* = 11.25 / M_\odot$, respectively, according to Moster et al. (2011). Accounting for the decreasing source density per redshift bin towards higher redshifts (see Table 4.2), due to both a

flux-limited selection and an intrinsic decrease in the number density of the bright population, we plan to target $\sim 100\%$ of the sources at $3 < z < 4$ ($i_{AB} = 24.3$) and $\sim 40\%$ of the sources ($i_{AB} = 24$) at $2 < z < 3$. Over the full 16 deg^2 , the total sample will contain about 47,000 galaxies between $2 < z < 4$. Three-hour integration times are required to ensure continuum detection, as described below. The total cost is 130,000 fiber hours or effectively 11 nights of observing time.

2. Galaxies at $4 < z < 6$ with $i < 25$ mag will be targeted over the 16 deg^2 survey field with 10% sampling. The intrinsic evolution in Ly α luminosity from $4 < z < 6$ will serve as an important benchmark for evaluating the impact of reionization on the Ly α luminosity function at $z > 5$. The required integration time for this faint sample is 6 hours, again to ensure continuum detection. We will target a total of 1,600 galaxies in 4,800 fiber hours (< 1 night).
3. We will target all LAEs with $z = 5.7, 6.6$ to $NB = 25$ mag over the full 16 deg^2 area. These galaxies are very faint: we will devote 5 hrs of integration time per galaxy. Their number density is 600 per PFS FOV for both redshifts combined, so we need 38,000 fiber hours (3 nights) for this component of the survey. Crucially, we will also study the intrinsic line shapes of LAEs at $z = 2.2$, for which we can obtain a systemic redshift from the [O II] line. It is important to quantify the intrinsic variability in Ly α line shape to distinguish from changes caused by neutral absorption at the epoch of reionization. We will observe these with 2hr integrations down to a limiting Ly α flux of $2 \times 10^{-16} \text{ erg s}^{-1} \text{ cm}^{-2}$, corresponding to an [O II] flux of $\sim 8 \times 10^{-18} \text{ erg s}^{-1} \text{ cm}^{-2}$. The expected space density is ~ 390 per PFS FOV. We will have a final sample of 4800 objects at a sampling rate close to 100%. The cost of this component will be 9,600 fiber hours (< 1 night).

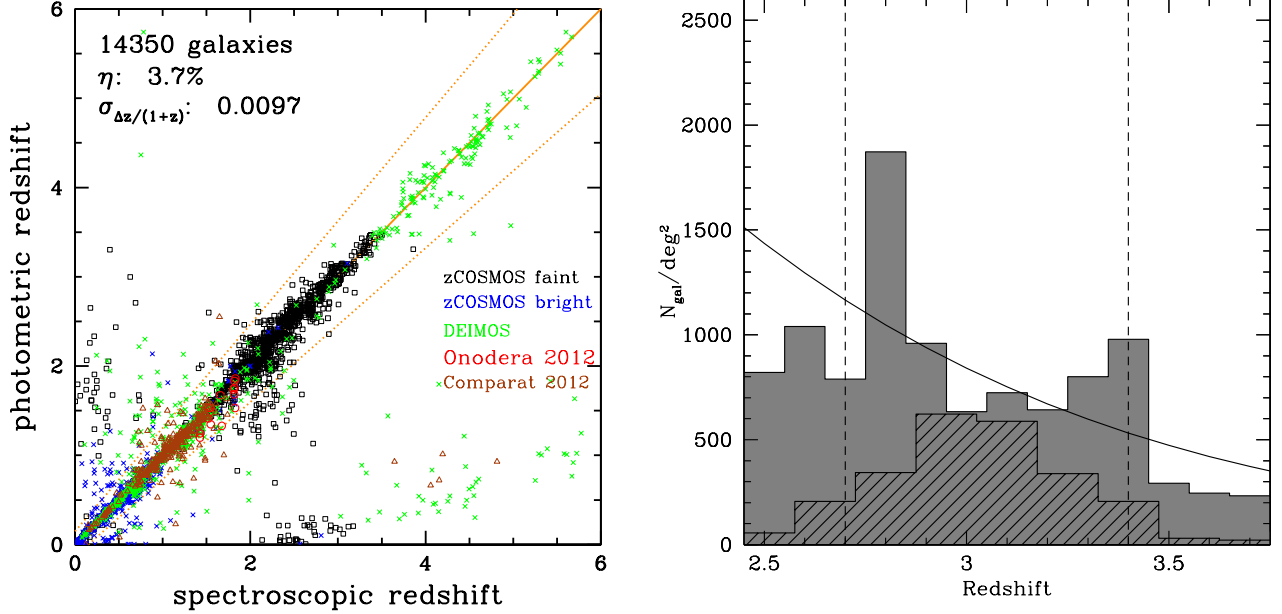


FIG. 34.— *Left:* A comparison between photometric and spectroscopic redshifts from O. Ilbert et al. in preparation from redshift measurements (zCOSMOS + DEIMOS programs) in the COSMOS field. With enough photometric coverage, photometric redshifts provide a reasonable selection method. *Right:* We contrast the gbell-shaped spectroscopic redshift $N(z)$ that results from a classic three-color LBG selection (hatched) with the result from the VVDS spectroscopic redshift sample magnitude-selected with $i_{\text{AB}} < 24.75$ (shaded) (see also Le Fèvre et al. 2013). The solid curve represents the best fit to the VVDS spectroscopic $N(z)$ equivalent to a photometric redshift distribution.

4. We will also target LBGs over the same redshift range ($2 < z < 6$) to a fainter limiting magnitude of $i_{\text{AB}} = 26$ mag (20k galaxies, using 10% sampling) within the HSC Ultra-deep area (3.5 deg^2). These require very deep exposures of 16 hours to spectroscopically identify the faintest galaxies yet observed. Based on previous work with much smaller samples, we expect a Ly α fraction of $\sim 30\%$ at $z = 3$ and at the magnitude limit, rising to $40 - 50\%$ at $z = 6$ (Stark et al. 2011). Thus, crudely speaking, we can expect a $30 - 40\%$ redshift success. This sample can be used to constrain the low end of the mass function at high redshift and to probe the circumgalactic medium of foreground galaxies as a function of impact parameter and galaxy type. This ultra-deep spectroscopic component will take 67,000 fiber hours (6 nights) to target $\sim 4,200$ galaxies (1,500 redshifts) using a 10% sampling at $i_{\text{AB}} = 24 - 26$ mag over 3.5 deg^2 .

Combining large samples of bright continuum-selected galaxies at intermediate redshifts with LAEs at the highest redshifts will allow us to trace the evolution in number-density and clustering of star-forming galaxies all the way to $z = 7$, as well as to probe cosmic reionization. Our wedding-cake structure will allow us to study both the large-scale distribution of these galaxies, as well as their detailed spectral properties for smaller, deeper samples.

4.5.2. Spectral Measurements

Here we summarize the main demands on the spectra for the high- z galaxy survey for each subsample, and justify that with the depths we plan, we will be able to achieve these goals.

1. For the continuum-selected samples, our first goal is to accurately measure a spectroscopic redshift. Our exposure times and depths are chosen to detect the continuum at the 3σ level. Based upon similar surveys

with the VLT, most spectra will have detectable spectroscopic features that provide a redshift (Le Fèvre et al. 2005; Lilly et al. 2007). In most cases, the presence of Ly α in emission or absorption is the dominant feature. We will also search for HeII $\lambda 1640$ in emission that may indicate the presence of population III stars. The expected equivalent widths for HeII range from $1 - 20\text{\AA}$, and have been detected in 10-15% of drop-out samples (e.g., Schaerer 2008). In stacks, we will use the strength and width of the line to look for signatures of winds (from Wolf-Rayet stars) and possibly signs of accretion/gravitational cooling.

2. We will search for absorption lines due to the interstellar medium, such as OI, CII, SiIV+OIV, SiII and CIV are present (see Fig. 27). These can provide information on the stellar populations and metallicities of high redshift galaxies especially for the rare, bright ($i < 23$) examples that exist in small numbers in current surveys (e.g., Shapley et al. 2003). We note that for the subsample of objects at $z \approx 2$, for which we have both [O II] and Ly α , we will also know the true rest frame of the galaxy very well. For the typical objects, using stacks of ~ 100 spectra, we will measure line profiles and velocity offsets to indicate the presence of inflows or outflows (e.g., Steidel et al. 2010).
3. Line fluxes of Ly α emitters will reach a depth, at a S/N level of 5, of $F = 0.8 \times 10^{-17} \text{ erg s}^{-1} \text{ cm}^{-2}$, which is typical of LAEs at $5 < z < 7$ depending on the line profile. We can recover fluxes and linewidths at the 10% level in the blue arm and at the 20% level in the red arm.
4. Broad emission lines ($\text{FWHM} > 1200 \text{ km s}^{-1}$) and the presence of CIV/CIII in emission will be used as a sig-

nature of AGN activity.

4.5.3. Target Selection: Quasars down the luminosity function

Like the LBG samples described above, we will pursue a two-tiered quasar selection. We will perform a quasar survey within the BAO redshift survey over 1400 deg^2 and a deeper survey within the 16 deg^2 area described here. Our target strategy is summarized in Table 9.

The PFS-AGN wide survey is based on the wide layer of the HSC multi-band imaging legacy survey (5-band optical images of g, r, i, z , and y over 1400 deg^2 , combined with available wide NIR surveys by VISTA and UKIRT). We focus on the color-selected quasar candidates at $3 < z < 7$ using color cuts similar to those used by the SDSS (Richards et al. 2002). Within the BAO survey, we will target a few tens of quasar candidates per PFS pointing to a magnitude limit of $J \leq 24$ with half-hour integration times, to achieve the number-density of quasars shown in Table 9. The primary goals include identifying $6 < z < 7$ candidates for deeper spectroscopy to study reionization, measuring the quasar luminosity and mass function over $3.5 < z < 7$, and measuring the quasar auto- and cross-correlation functions. The total number of targets is small, and it will be integrated into the wide-field cosmology survey. As shown above, we can achieve these goals in 0.5 hr integration times even at our magnitude limit (Fig. 28). We note that the PFS cosmology survey requires 2 pointings per field, each of which has 0.5 hr integration time, giving us time to observe quasars.

The PFS-AGN deep survey is based on the deep layer of the HSC legacy survey. In addition to color selection, we will also target variable objects and X-ray and mid-infrared selected objects. We will go a magnitude deeper than the PFS-AGN wide survey, and expect to target 100 active galaxies per deg^2 . The goals include finding ~ 10 faint $z \approx 7$ quasars, studying X-ray and variability selected active galaxies at $1 < z < 4$, cross-correlating absorption systems in the quasar spectra with the foreground galaxy population, and studying obscured populations in the galaxy survey that are identified via narrow emission lines. If we spend an hour per target for the majority of these targets, then it will take very few fibers from the main galaxy evolution survey.

4.5.4. Summary of the Survey

In Table 9 we show all the sub-samples that we plan to target, their expected number density per square degree, the required exposure times, and the proposed survey area. Throughout, when we quote the required number of nights, we are assuming 2000 science fibers per PFS pointing and no overhead in changing targets. We quote the number of required clear nights (that is, no weather factor has been applied). We outline a two-tiered survey, with our primary galaxy survey covering 16 deg^2 and a deeper component covering 3.5 deg^2 . To summarize, we will use the following selections to trace the evolution of galaxies from cosmic dawn to the peak epoch of stellar mass build-up:

- We will perform a continuum-selected survey of $1 < z < 2$ galaxies with $J_{\text{AB}} < 23.4 \text{ mag}$ over 16 deg^2 and $0 < z < 1$ galaxies with $J_{\text{AB}} < 21 \text{ mag}$. We will target $\sim 28,000$ galaxies per deg^2 , requiring multiple pointings per field. The primary survey will be color-selected, using a combination of HSC and NIR imaging. We will also perform a purely magnitude-limited

survey over two PFS pointings early in the survey to calibrate our selection strategy.

- At $2 < z < 7$, we trace the galaxy population using bright dropouts down to a limiting magnitude of $i < 24 \text{ mag}$ over the full 16 deg^2 . We expect to target 430 galaxies per deg^2 . We will survey much fainter LBGs to $i < 26 \text{ mag}$ over 3.5 deg^2 to study intervening absorption systems.
- We focus on LAEs at $z = 5.5, 6.6, 7.3$, in order to use the Ly α emission as a probe of reionization. Additionally we will study LAEs at $z \sim 2.3$, where we can use the [O II] emission line to measure the systemic redshift.

Adopting these survey areas and target densities, the survey requires 100 clear nights. The survey parameters are summarized in Table 10.

4.6. Requirements

We are assuming the nominal sensitivities and resolution of PFS. The feasibility of our survey relies most heavily on the sensitivity of PFS in the red and NIR arms, from which we will derive redshifts and key diagnostic information. Our numbers are summarized in Table 11. Our most important assumptions are:

1. We assume 2000 science fibers per PFS pointing (with 400 fibers devoted to sky). We also assume that it is possible to reposition fibers rapidly, so that we move off of bright targets in a short time. This large multiplexing capability is crucial for our science case, otherwise we cannot achieve the large areas and high sampling rates that make our survey unique.
2. We assume that we can measure continuum-based redshifts at our magnitude limit of $J_{\text{AB}} = 23.4 \text{ mag}$. Based on our spectral simulations, we find that in a 3 hr integration we will achieve a S/N of at least five in the 4000 \AA break in the NIR arm to measure continuum-based redshifts (Tonry & Davis 1979). We suggest real-time spectral analysis to identify low redshift interlopers after the initial 20 min integration.
3. We expect to reach a 5σ line-flux limit of at least $10^{-17} \text{ erg s}^{-1} \text{ cm}^{-1}$ over $> 75\%$ of the NIR arm. We estimate that this limit is reached in the NIR arm in 3 hrs of integration on the [O II] line. We are assuming intrinsic line widths in the galaxies of $\sigma_{\text{gas}} \approx 100 \text{ kms}^{-1}$. The S/N will degrade by $\sim 30\%$ for a galaxy with twice the dispersion, as the light is spread over roughly twice as many pixels. This gets us to $L_{[\text{OII}]} \sim 3 \times 10^{41} \text{ erg s}^{-1}$ at $z \approx 2$, which is close to the [O II] luminosity of a typical L^* galaxy at this epoch (e.g., Takahashi et al. 2007).
4. In the blue and red arms, our detection limit is deeper. We find that we can detect Ly α with $7 \times 10^{-18} \text{ erg s}^{-1} \text{ cm}^{-2}$ in the blue arm with $R \approx 1300$ at the 5σ level in 6 hrs of integration. Again we assume an intrinsic gas dispersion of 100 kms^{-1} , which is typical of measured LAEs (Ouchi et al. 2010). We are thus detecting sources with $L > 1.5 \times 10^{42} \text{ erg s}^{-1}$, which is a factor of five fainter than the typical LAE at these

TABLE 10
SURVEY PARAMETERS

$1 < z < 2$	
Selection (optical)	HSC Deep: $i < 27.2$ mag
Selection (NIR)	<i>XMM</i> -LSS, ELAIS-N1, and DEEP2-3: $J_{AB} < 23.4$ mag
Exposure time at flux limit	3 hrs
Area	16 deg ²
Number of nights	69 nights
Flux-limited survey	
Selection (NIR)	<i>XMM</i> -LSS, ELAIS-N1, and DEEP2-3: $J_{AB} < 23.4$ mag
Exposure time at flux limit	3 hrs
Area	2 PFS pointings
Number of nights	8
High-redshift galaxies	
Selection (optical)	HSC Deep: $i < 27.2$ mag
Selection (narrow-band)	HSC Deep: $NB < 25$ mag
Exposure time at flux limit	3-16 hrs
Area	16 deg ²
Number of nights	23
Total number of nights	100

redshifts (Ciardullo et al. 2012). In the red arm, our limits are slightly better. In 6 hrs our 5σ detection limit is 5×10^{-18} erg s⁻¹ cm⁻². Here our limits of 8.5×10^{42} erg s⁻¹ at $z = 5$ and 2×10^{43} erg s⁻¹ at $z = 6$ are around or slightly exceed $L_{Ly\alpha}^*$ at these epochs (Ouchi et al. 2010). Our limits are comparable to those achieved by Ouchi et al. (2010) for an individual object, and we will increase the sample size by two orders of magnitude.

5. In order to achieve the above continuum and emission-line limits above, we place strong requirements on our software, specifically in regard to sky subtraction in the red and NIR arms. We assume that we are able to determine the sky level at a given time to 0.5%. This is supported by the Poisson noise in the lines themselves, and experience with BOSS (Bolton et al. 2012). Also, we assume that 0.5% of the light hitting the detector is distributed across the entire chip as a smooth background. We show that our primary science goals will succeed if the background subtraction is poorer and scattered light fraction higher than the specifications. However, our more challenging goals of measurement continuum properties of $z \approx 1.5$ galaxies do require the three-hour integration times proposed here.

5. SCIENCE REQUIREMENTS

We now summarize the science requirements arising from the earlier sections. These requirements are necessary for deriving lower level instrument requirements and in understanding the flow of requirements from the science to detailed engineering. Establishing the science requirements flow is likewise essential in order to track the science impact of potential changes to the instrument configuration in the future. The top level science requirements and observing requirements are intended to be directly verifiable items in the project. For convenience, we list the overall drivers, item by item, both in tabular form and in more detail below.

The top-level science requirements for the PFS surveys described in the previous chapters are summarized in Table 12²².

²² Our instrumental requirements for the different scientific goals outlined in this document are somewhat different. In particular, the galaxy science,

Note that we gave the requirements for the MR mode in Table 7, which is derived from the GA science.

We briefly discuss the individual entries in Table 12.

- *Wavelength Coverage:* The triple-armed spectrograph design offers complete and simultaneous spectral coverage from 380 through 1260 nm and clearly this represents a unique feature of PFS. The driver for this requirement arises from all 3 surveys discussed in Chapters 2–4 but particularly the cosmology and galaxy surveys. The cosmology survey will enable the first BAO and RSD tests beyond $z \simeq 2$ and the galaxy survey will track emission line properties of an unprecedented sample of galaxies with no ‘gaps’ in redshift coverage.
- *Spectral Resolution:* The resolutions of the three arms of each spectrograph are designed to ensure optimal efficiency in the study of stars and galaxies over the wide wavelength range. The resolution must be higher in the red and near-infrared arm to ensure optimal sky subtraction in the dense OH forest. The minimum effective resolution in the red arm is set by our requirement to measure accurate velocities and stellar metallicities for the Galactic surveys.
- *Fiber Density:* The fiber density is set by the field of view of the provided Subaru prime focus corrector and our requirement that we optimally sample the $0.8 < z < 2.4$ galaxy population for the cosmology survey at the wavenumber k where the BAO signal is to be recovered. Formally, this sets a requirement that the mean number density of target galaxies \bar{n}_g and the galaxy power spectrum $P_g(k)$ should satisfy $\bar{n}_g P_g \simeq 1$ (or a few) at $k \simeq 0.1 h^{-1}$ Mpc.
- *Throughput:* The throughput requirement is driven by a combination of the S/N required for the various surveys and the available observing time, and is consistent with a preliminary assessment of the instrument performance. The values in the table exclude atmosphere,

which requires the deepest exposures, have the strongest requirements on systematics such as stray light and sky subtraction. The overall requirements listed in Table 12 represent a compromise of sorts between the needs of the different scientific goals. As the instrument design becomes more solid, we will see to what extent the more stringent requirements of the galaxy evolution science are possible.

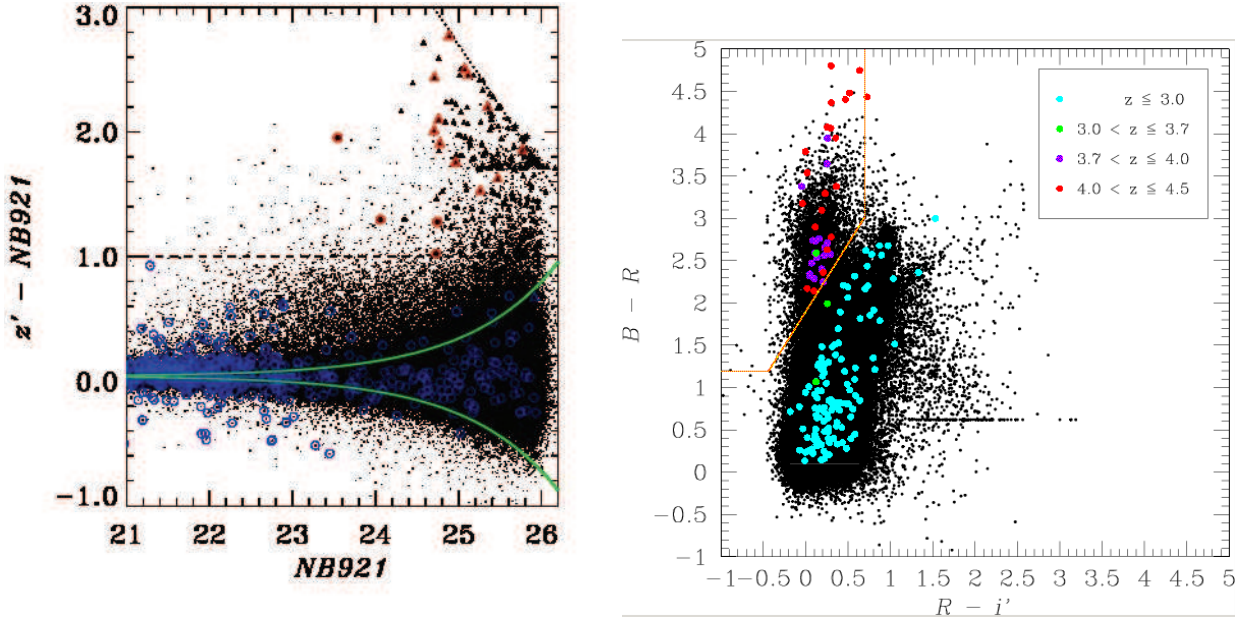


FIG. 35.— *Left*: Color magnitude diagram of narrow-band excess color ($z' - NB921$) vs. narrow-band magnitude ($NB921$) for selecting $z = 6.6$ LAEs in the SXDS field (Ouchi et al. 2010), which will be applied to the LAE selection of our PFS survey. Black dots present colors of all the detected objects, while black filled circles and triangles denote the $z = 6.6$ LAEs. Red and blue open symbols mark spectroscopically-identified objects in the redshift range of LAEs ($z = 6.45 - 6.65$) and interlopers, respectively. The green lines indicate 2σ errors of the color of $z' - NB921$. Dashed and dotted lines represent the color cut for the narrow-band excess and the 1σ limit of z' data, respectively. *Right*: Two color diagram of objects down to $i' \leq 26.85$ to select $z \sim 4$ LBGs in the Subaru Deep Field (Yoshida et al. 2006). The horizontal sequence along $B - R = 0.62$ shows objects which are fainter than the 1σ magnitude in both B and R . The colored symbols show objects with spectroscopic redshifts, where cyan, green, violet, and red represent objects in the range $z < 3.0$, $3.0 \leq z < 3.7$, $3.7 \leq z < 4.0$, and $4.0 \leq z < 4.5$, respectively. The thick orange line indicates the boundary which are adopted for the selection of $z \sim 4$ LBGs. Our PFS survey will use a broad-band set of $g'r'i'$ different from this BRi' bands for selecting $z \sim 4$ LBGs. However, the contamination rates of our $z \sim 4$ LBG sample will be comparable, as demonstrated by another $z \sim 4$ LBG selection with GRI bands (Steidel et al. 1999).

TABLE 11
LEVEL 2 GALAXY SURVEY REQUIREMENTS

Number of science fibers	2000
Field of view	1.3 deg. diameter
Exposure time for flux limits	3 hrs
Fraction of resolution elements above flux limit	75%
Blue Arm	
Wavelength coverage (\AA)	3800-6700
Spectral Resolution, continuum	$R \approx 400$
5σ Flux limit, continuum	24.5 AB mag
Spectral Resolution, emission lines	$R \approx 1300$
5σ Flux limit, line ($\sigma_{\text{gas}} = 100 \text{ kms}^{-1}$)	$10^{-17} \text{ erg s}^{-1} \text{ cm}^{-2}$
Red Arm	
Wavelength coverage (\AA)	6500-10000
Spectral Resolution, continuum	$R \approx 300$
5σ Flux limit, continuum	24.5 AB mag
Spectral Resolution, emission lines	$R \approx 1300$
5σ Flux limit, line ($\sigma_{\text{gas}} = 100 \text{ kms}^{-1}$)	$7 \times 10^{-18} \text{ erg s}^{-1} \text{ cm}^{-2}$
NIR Arm	
Wavelength coverage (\AA)	10000-12600
Spectral Resolution, continuum	$R \approx 300$
5σ Flux limit, continuum	24 AB mag
Spectral Resolution, emission lines	$R \approx 1300$ for line calculations
5σ Flux limit, line ($\sigma_{\text{gas}} = 100 \text{ kms}^{-1}$)	$10^{-17} \text{ erg s}^{-1} \text{ cm}^{-2}$
Sky continuum	21.56 mag AB arcsec $^{-2}$ at $1\mu\text{m}$ at zenith
OH line brightness	16.6 mag AB arcsec $^{-2}$ at J -band at zenith
Systematic in sky subtraction δ sky flux	0.5 - 2%
Overall Sky level determination	0.5%
Scattered light	23 - 19.75 AB mag

NOTE. — PFS instrument parameters that we assume in calculating simulated spectra and assessing feasibility. We show only parameters that (a) are important in our calculations and (b) differ from the assumptions in Table 1.

central obscuration, vignetting, and the fiber aperture effect.

- *Fiber Reconfiguration Time*: The reconfiguration time is set by the cosmology survey. It has a short expo-

TABLE 12
Top-Level Science Requirements

Requirement	Value	Main Driver(s)
Wavelength Coverage	380 – 1260nm	All surveys
Spectral Resolution	Blue: $R \sim 2500$ Red: $R \sim 3000$ NIR: $R \sim 4000$	Matched survey efficiency sky subtraction, stellar metallicities radial velocity precision
Fiber Density	≥ 2400 per 1.3 deg. diameter hexagonally-shaped field	$\bar{n}_g P_g \simeq$ a few @ $k = 0.1 h/\text{Mpc}$ requirement in BAO survey
Throughput ^a	Average: $\geq 22\%$ (blue) $\geq 22\%$ (red) $\geq 24\%$ (NIR) Worst part of band: $\geq 20\%$ (blue) $\geq 20\%$ (red) $\geq 18\%$ (NIR)	Matched survey efficiency
Fiber Reconfig. Time	$\lesssim 3\text{min}$ in total	15min exposure in BAO survey
Sky Subtraction Accuracy	$\lesssim 1\%$ of sky background per 4-pixel resolution element	in all surveys
Stray Light	\lesssim a few % of total sky brightness spread over detector	in all surveys
Read Out	≤ 3 (Red) e^- rms per pixel ≤ 4 (NIR) e^-	in all surveys
Wavelength Calibration	$\lesssim 0.1\text{\AA}$ ($\sim 1/20\text{th}$ of a resolution element)	for velocity precision
Fiber Diameter	1.13'' deg. diameter at the field center 1.03'' at the edge	Optimal S/N for galaxy survey
Pre-Imaging Data	<i>gri</i> to 25mag over 1400 deg ² <i>griz+NB515</i> survey to $V \simeq 22.5\text{mag}$ <i>grizy+NBS+J</i> to $\sim 27\text{mag}$ over 16 deg ²	Color selection of ELGs for BAO survey Selection of stars in Milky Way/M31 Color selection for galaxy survey
Survey Area	~ 1400 deg ² for BAO ~ 500 deg ² for GA survey ~ 16 deg ² for galaxy survey	Statistical requirements, cosmic variance, matching HSC data

^a Excludes atmosphere, central obscuration + WFC vignetting, and fiber aperture effect.

sure time, because the cosmology survey must survey a large volume by targeting strong line emitting galaxies. If the exposure time is $\simeq 15$ minutes, a reconfiguration time (including slewing, acquisition, guiding, fiber positioning and verification) should be completed in under 3 minutes to maximize survey efficiency.

- *Sky Subtraction Accuracy*: This is set by the requirement for high quality spectra at faint limits in all surveys. It is particularly driven by the need for accurate absorption line measures in the red and near-infrared spectral regions where the OH forest is dense.
- *Stray Light*: As for sky subtraction, given the intensity of the OH night sky emission.
- *Detector Read Out*: This is set by the signal/noise requirements of each survey, noting their likely photon and sky-noise components.
- *Wavelength Calibration*: This is determined by the radial velocity accuracy requirement for the Galactic surveys.
- *Fiber Diameter*: This is determined by the optimal signal/noise requirements of the galaxy and cosmology

survey, noting the distribution of line emission in these extended sources.

- *Pre-Imaging Data*: This is determined by each individual survey and the various color-criteria to be adopted in optimally selecting either galaxies in a particular redshift range with certain star formation characteristics or stars of a given luminosity class in the Milky Way or M31. The aim is to ensure that all the relevant data not currently in hand is taken by HSC.
- *Survey Area*: This varies from one survey to another but is driven by statistical and/or cosmic variance requirements and the availability of HSC imaging data.

6. OUTSTANDING ISSUES

Our primary goal has been to present the science case for PFS in the context of an anticipated 300-night Subaru Strategic Program (SSP) and, thereby, to define the scientific requirements for the instrument as summarized in the previous section. The successful review of this science case and its associated technical document has led to an agreement to begin PFS construction with an anticipated first light in early 2017.

Science planning will naturally continue and here we briefly describe those activities in the context of instrumental choices, the design of the survey and the broader impact of

PFS beyond the initial SSP.

It should be understood that PFS planning involves two rather different communities: the international partnership focused scientifically via the PFS Survey Committee, and the Japanese astronomical community, whose interests are coordinated by the National Astronomical Observatory of Japan and its appointed national committees.

In the following we briefly introduce some of the items which will form the basis of the project discussions.

6.1. Requirements Flowdown

As discussed in Section 5, for a project with the size and complexity of PFS, formal science and instrument requirements are necessary to guide the design and construction of the system, and allow the rapid assessment of design or performance changes during the course of the project. They will also guide the instrument test plan to be developed at a later stage in the project; each requirement will include the method for validating that it has been met. The full documentation of formal and tracked requirements will define the required performance of the instrument system and the subsystems in order to achieve the science goals.

The requirements can be broken into several levels, and we will use the following definitions. The Level 1 (L1) requirements are the top level science requirements that comprise the reason for building the instrument. The Level 2 (L2) requirements are ones that are imposed on the entire instrument or multiple subsystems. Requirements on a single subsystem are Level 3 (L3) requirements. Level 4 (L4) requirements are the requirements created by the subsystem designers in order to implement the Level 3 requirements.

Although the top level science requirements, L2, are summarized in Section 5, they will be refined (the L1 requirements are described in detail in Sections 2 – 4 for each science case). These focus on the science driven requirements and may not yet be complete. Specifically, they do not yet include all of the instrument level operational and interface requirements. The L3 and L4 requirements are in the process of being developed. Although there has been extensive discussion of these requirements, they are not yet ready for this documentation.

The PFS project office will lead the effort to refine, formalize, and document the L1-L4 requirements, in coordination with the science and instrument working groups. This process will be complete for the L1-L3 requirements soon. The documentation will consist of a formal list of individual requirements with a description, rationale, and validation method listed for each requirement. The rationale will consist of a short paragraph explaining why the requirement is needed, any assumptions that were made, and what design effort drove the requirement. It puts the requirement in context, and helps reduce ambiguities and misunderstandings. All of the instrument requirements are intended to be verified during the acceptance testing of the instrument, under a written test plan.

6.2. Planning the Subaru Strategic Program

The three Working Groups have, thus far, largely worked independently in defining their science requirements and there has been little discussion of how to integrate the 3 surveys into a single coherent observing program. Ultimately the PFS partnership will have to take the programs described in Sections 2 – 4 forward and write one or more Subaru Strategic

Programs for consideration by the NAOJ Subaru Time Allocation Committee.

Issues that the PFS team will address in discussions with NAOJ and the HSC team will include:

- Selecting fields within the HSC imaging survey
- Science prioritization of the various survey components
- Target sharing and exposure time optimization
- Bright and dark time balance on the telescope

The bright and dark time balance will depend critically on the question of how the Subaru Observatory intends to operate PFS alongside HSC and the bright time use of PFS will, in turn, depend on whether there is a feasible intermediate dispersion capability.

6.3. Legacy Value

The Subaru archive is formally a responsibility of NAOJ, but the quality and delivery of the survey products are that of the current PFS science team. No negotiations have yet taken place on this important issue, but we expect a full agreement on responsibilities, proprietary periods, international access etc.

6.4. Synergy with Other Facilities

PFS will have a significant impact beyond the surveys discussed in this document in two ways.

Firstly, the survey fields will deliver spectroscopic data of value to extant imaging facilities. During the pre-LSST era we can expect inquiries from those international teams for access to PFS data. Such access could be dealt with largely under the auspices of the Subaru archive discussed above, but there may be cases where new collaborations will be valuable, either to the PFS team, the Japanese community or both. Such opportunities will need to be considered and the roles and rights of the PFS team, NAOJ etc fully understood.

A potentially more interesting opportunity is the likelihood of new collaborations with both current imaging survey telescopes and future facilities such as LSST, Euclid and perhaps ultimately TMT, beyond the scope of the Subaru Strategic Program (SSP) introduced here. Formally, beyond the SSP, PFS will become the property of NAOJ but the current partnership may have the opportunity to participate and contribute in future surveys conducted in conjunction with other facilities.

7. SUMMARY

Our intention via this document is to describe in as much detail as practical, the exciting scientific programs we have designed for the Subaru Prime Focus Spectrograph, as well as to present our first iteration for a Subaru Strategic Program (SSP) of $\simeq 300$ nights that would realize these goals. The flow-down from these science requirements has been summarized in the context of the top-level instrument requirements which provide important constraints on the technical design of each component of PFS.

PFS will likely be the first massively-multiplexed spectrograph on a large aperture telescope to achieve first light. Its unique capabilities on an 8 meter platform at an excellent site promise exciting discoveries in 3 broad areas: the nature of dark energy through an ambitious survey of emission line

galaxies over an unprecedented redshift range $0.8 < z < 2.4$, the assembly history of the Milky Way and M31 through strategically-designed programs that exploit astrometric data from the Gaia mission, and galaxy evolution over a wide range in redshift ($1 < z < 7$) exploiting PFS' unique wide wavelength coverage.

Although our initial goal is to construct the instrument and conduct a refined version of the SSP presented in this article, we are strongly motivated to consider the longer term role of

this survey instrument in the era of LSST, Euclid and TMT.

This work is supported in part by the JSPS Core-to-Core Program "International Research Network for Dark Energy", by World Premier International Research Center Initiative (WPI Initiative), MEXT, Japan, and by the FIRST program "Subaru Measurements of Images and Redshifts (SuMIRe)", CSTP, Japan.

REFERENCES

- Adelberger, K. L., Steidel, C. C. 2005, *ApJ*, 630, 50
 Albrecht, A., et al., The Dark Energy Task Force Report, astro-ph/0609591
 Alcock, C., Paczynski, B. 1979 *Nature* 281, 358
 Anderson, L., et al. 2012, *MNRAS*, 427, 3435
 Ando, M., Ohta, K., Iwata, I., Akiyama, M., Aoki, K., Tamura, N. 2007, *PASJ*, 59, 717
 Behroozi, P. S., Wechsler, R. H., & Conroy, C. 2013, *ApJ*, 770, 57
 Blake, C., et al. (WiggleZ team) 2011, *MNRAS*, 415, 2892
 Bolton, A. S., Schlegel, D. J., Aubourg, É., et al. 2012, *AJ*, 144, 144
 Bordoloi, R., et al. 2011, *ApJ*, 743, 10
 Brammer, G. B., van Dokkum, P. G., Coppi, P. 2008, *ApJ*, 686, 1503
 Bullock, J. S., & Johnston, K. V. 2005, *ApJ*, 635, 931
 Carlberg, R. G., et al. 2011, *ApJ*, 731, 124
 Ciardullo, R., et al. 2012, *ApJ*, 744, 110
 Chen, Y.-M., et al. 2012, *MNRAS*, 421, 314
 Coil, A., et al. 2008, *ApJ*, 672, 153
 Contaldi, C. R., Peloso, M., Kofman, L., Linde, A. 2003, *JCAP* 07, 002
 Cooper, M. C., et al. 2006, *MNRAS*, 370, 198
 Cooper, A. P., et al. 2010, *MNRAS*, 406, 744
 Cucciati, O., et al. 2012, *A&A*, 539, 31
 Dalal, N., Dore, O., Huterer, D., Shirokov, A. 2008, *Phys. Rev. D* 77, 123514
 Davis, M., Faber, S. M., Newman, J., et al. 2003, *SPIE*, 4834, 161
 Dekel, A., & Birnboim, Y. 2006, *MNRAS*, 368, 2
 De Lucia, G., Springel, V., White, S. D. M., Croton, D., & Kauffmann, G. 2006, *MNRAS*, 366, 499
 De Silva, G. M., Freeman, K. C., Bland-Hawthorn, J., Asplund, M., Bessell, M. S. 2007, *AJ*, 133, 694
 Efstathiou, G. 2003, *MNRAS* 343, L95
 Eisenstein, D., et al. 2005, *ApJ* 633, 560
 Eisenstein, D., Seo, H.-J., Sirko, E., Spergel, D. N. 2007, *ApJ*, 664, 675
 Font, A. S., et al. 2011, *MNRAS*, 416, 2802
 Freeman, K., & Bland-Hawthorn, J. 2002, *ARAA*, 40, 487
 Freivogel, B., Kleban, M., Martinez, M. R., Susskind, L. 2006, *JHEP*, 03, 039
 Gibson, B. K. 1998, *ApJ*, 501, 675
 Gilbert, K. M. et al. 2012, *ApJ*, 760, 76
 Gómez, F. A., Helmi, A., Brown, A. G. A., Li, Y.-S. 2010, *MNRAS*, 408, 935
 Guth, A. H., Nomura, Y. 2012, arXiv:1203.6876
 Guzzo, L., et al. 2008, *Nature*, 451, 541
 Hayashi, H., & Chiba, M. 2006, *PASJ*, 58, 835
 Hayashi, K., & Chiba, M. 2012, *ApJ*, 755, 145
 Helmi, A., de Zeeuw, P. T. 2000, *MNRAS*, 319, 657
 HerMES Collaboration, Oliver, S. J., Bock, J., et al. 2012, arXiv:1203.2562
 Hikage, C., Takada, M., Spergel, D. N. 2012, *MNRAS*, 419, 3457
 Hikage, C., Mandelbaum, R., Takada, M., Spergel, D. N. 2012, arXiv:1211.1009
 Ho, L. C., Filippenko, A. V., & Sargent, W. L. W. 1997, *ApJS*, 112, 315
 Hu, W., Haiman, Z. 2003, *Phys. Rev. D* 68, 063004
 Jovel, S., et al. 2011, *A&A* 504, 359
 Kaiser, N., *MNRAS* 227, 1 1987
 Kirby, E. N., Guhathakurta, P., & Sneden, C. 2008, *ApJ*, 682, 1217
 Kirby, E. N. et al. 2009, *ApJ*, 705, 328
 Kirby, E. N. et al. 2010, *ApJS*, 191, 352
 Kleban, M., Schillo, M., arXiv:1202.5037
 Komatsu, E., *WMAP Team* 2011, *ApJ Suppl.*, 192, 18
 Kormendy, J., Richstone, D. 1995, *ARA&A*, 33, 581
 Kriek, M., et al. 2006, *ApJ*, 649, L71
 Kriek, M., van Dokkum, P. G., Whitaker, K. E., Labbé, I., Franx, M., Brammer, G. B. 2011, *ApJ*, 743, 168
 Leauthaud, A., Tinker, J., Bundy, K., et al. 2012, *ApJ*, 744, 159
 Lee, Y. S. et al. 2011, *ApJ*, 738, 187
 Le Fèvre, O., et al. 2005, *A&A*, 439, 845
 Le Fèvre, O., et al. 2013, arXiv:1307.0545
 Le Fèvre arXiv:1307.0545
 Lilly, S. J., et al. 2007, *ApJS*, 172, 70
 Lilly, S. J., et al. 2009, *ApJS*, 184, 218
 Linder, E. 2003, *Rhys. Rev. Lett.*, 90, 091301
 Linder, E. 2005, *Rhys. Rev. D* 72, 043529
 Maraston, C. 2005, *MNRAS*, 362, 799
 Marconi, A., Hunt, L. K. 2003, *ApJ*, 589, L21
 Magorrian, J., et al. 1998, *AJ*, 115, 2285
 Matsubara, T. 2008, *Phys. Rev. D* 77, 063530; *Phys. Rev. D* 78, 083519
 Matsubara, T. 2011, *Phys. Rev. D* 83, 083518
 McQuinn, M., Hernquist, L., Zaldarriaga, M., & Dutta, S. 2007, *MNRAS*, 381, 75
 Moster B.P., Somerville R.S., Newman J.A., and Rix H., 2011, *ApJ*, 731, 113
 Newman, J. A., Cooper, M. C., Davis, M., et al. 2012, *ApJS*, submitted (arXiv:1203.3192)
 Nishimichi, T., Taruya, A. 2011, *Phys. Rev. D* 84, 043526
 Nishizawa, A., Takada, M., Nishimichi, T., in preparation.
 Nissen, P. E., Schuster, W. J. 2010, *A&A*, 511, L10
 Orsi, A., Baugh, C., Lacey, C., Cimatti, A., Wang, Y., Zamorani, G. 2010, *MNRAS*, 405, 1006
 Ostriker, J. P. & Steinhardt, P. 2003, *Science*, 300, 1909
 Ouchi, M., et al. 2008, *ApJS*, 176, 301
 Ouchi, M., et al. 2010, *ApJ*, 723, 869
 Padmanabhan, N., Xu, X., Eisenstein, D., Scalzo, R., Cuesta, A. J., Metha, K., Kazin, E., arXiv:1202.0090
 Panter, B., Jimenez, R., Heavens, A. F., Charlot, S. 2007, *MNRAS*, 378, 1550
 Papovich, C. 2008, *ApJ*, 676, 206
 Peacock, J. A., et al. (the 2dF team) 2001, *Nature*, 410, 169
 Percival, W., et al. 2007, *MNRAS*, 381, 1053
 Peñarrubia, J. et al. 2005, *ApJ*, 626, 128
 Planck Collaboration: Ade, P. A. R. et al. 2013, arXiv:1303.5084
 Planck Collaboration: Ade, P. A. R. et al. 2013, arXiv:1303.5076
 Reddy, N., et al. 2012, *ApJ*, 744, 154
 Richards, G. T., et al. 2002, *AJ*, 123, 2945
 Richardson, J. C., et al. 2011, *ApJ*, 732, 76
 Saito, S., Takada, M., Taruya, A. 2008, *Phys. Rev. Lett.*, 100, 191301
 Saito, S., Takada, M., Taruya, A. 2008, *Phys. Rev. D* 80, 083528; 2011, *Phys. Rev. D* 83, 043529
 Schaerer, D. 2008, *IAU Symposium*, 255, 66
 Schiavon, R. P., Faber, S. M., Konidaris, N., et al. 2006, *ApJ*, 651, L93
 Sehgal, N., et al. 2010, *ApJ*, 709, 920
 Seo, H.-J., Eisenstein, D. 2003, *ApJ*, 598, 720
 Seo, H.-J., Eisenstein, D. 2007, *ApJ*, 665, 14
 Shapley, A. E., Steidel, C. C., Pettini, M., Adelberger, K. L. 2003, *ApJ*, 588, 65
 Shen, Y., Greene, J. E., Strauss, M. A., Richards, G. T., & Schneider, D. P. 2008, *ApJ*, 680, 169
 Shimasaku, K., Hayashino, T., Matsuda, Y., et al. 2004, *ApJ*, 605, L93
 Alosar, A., et al. 2013, *JCAP*, 4, 26
 Springel, V., White, S. D. M., Jenkins, A., et al. 2005, *Nature*, 435, 629
 Sobral, D., et al. 2010, *MNRAS*, 404, 1551
 Stark, D. P., Ellis, R. S., & Ouchi, M. 2011, *ApJ*, 728, L2
 Steidel, C., Adelberger, K., Shapley, A. 2003, *ApJ*, 592, 728
 Steidel, C. C., et al. 2010, *ApJ*, 717, 289
 Sugai, H., et al. 2012, *SPIE*, 8446, 84460Y-13
 Sugiyama, N. S., Futamase, T. 2012, arXiv:1210.7499
 Takada, M., Komatsu, E., Futamase, T. 2006, *Phys. Rev. D* 73, 083520
 Takahashi, M. I., et al. 2007, *ApJS*, 172, 456
 Tanaka, M., et al. 2010, *ApJ*, 708, 1168
 Tang, J., Kayo, I., Takada, M. 2011, *MNRAS*, 416, 2291
 Taruya, A., Nishimichi, T., Saito, S., Hiramatsu, T. 2009, *Phys. Rev. D* 80, 123503
 Taruya, A., Nishimichi, T., Saito, S. 2010, *Phys. Rev. D* 82, 063522
 Taruya, A., Bernardeau, F., Nishimichi, T., Sandrine, C. 2012, *Phys. Rev. D* 86, 103528
 Tinker, J. L., Wetzel, A. R. 2010, *ApJ*, 719, 88
 Tolstoy, E., Hill, V., & Tosi, M. 2009, *ARAA*, 47, 371
 Tonry, J., & Davis, M. 1979, *AJ*, 84, 1511
 Tumlinson, J., et al. 2011, *Science*, 334, 948
 Van den Berk, D. E., et al. 2001, *AJ*, 122, 549
 Walker, M G., & Peñarrubia, J. 2011, *ApJ*, 742, 20
 Walker, M G., et al. 2009, *AJ*, 137, 3100
 Whitaker, K. E., et al. 2011, *ApJ*, 735, 86
 Williams, R. J., Quadri, R. F., Franx, M., van Dokkum, P., Labbé, I. 2009, *ApJ*, 691, 1879
 Wyse, R. F. G., & Gilmore, G. 1992, *AJ*, 104, 144
 Yan, R., Newman, J. A., Faber, S. M., et al. 2006, *ApJ*, 648, 281
 Yoshida, M., et al. 2006, *ApJ*, 653, 988

APPENDIX
PFS COLLABORATION

Principal Investigator (PI)

Hitoshi Murayama Kavli Institute of the Physics and
Mathematics for the Universe (Kavli IPMU, WPI), Japan;
Physics Department, University of California, Berkeley;
Lawrence Berkeley National Laboratory, Berkeley, USA

Co-Chairs of the PFS Survey Committee

Richard Ellis Caltech, USA
Masahiro Takada Kavli IPMU, Japan

Co-Chairs of the PFS Science Working Groups

PFS Cosmology WG

Masahiro Takada Kavli IPMU, Japan
Christopher Hirata Caltech, USA
Jean-Paul Kneib LAM, France

PFS Galactic Archaeology WG

Masashi Chiba Tohoku University, Japan
Judith Cohen Caltech, USA
Rosemary Wyse JHU, USA

PFS Galaxy WG

Jenny Greene Princeton University, USA
Kevin Bundy Kavli IPMU, Japan
John Silverman Kavli IPMU, Japan
Masami Ouchi The University of Tokyo, Japan

PFS AGN/QSO WG

Tohru Nagao Kyoto University, Japan
Michael Strauss Princeton University, USA

PFS Steering Committee

H. Aihara (U. Tokyo/Kavli IPMU), N. Arimoto (NAOJ), R. Ellis (Caltech), T. Heckman (JHU), P. Ho (ASIAA), O. Le Fevre (LAM), H. Murayama (Kavli IPMU), L. Sodre Jr. (Sao Paulo), M. Seiffert (JPL/Caltech), D. N. Spergel (Princeton), Y. Suto (U. Tokyo), H. Takami (NAOJ)

Members in the PFS Science Working Groups

L. R. Abramo (Sao Paulo), H. Aihara (U. Tokyo/Kavli IPMU), W. Aoki (NAOJ), N. Arimoto (NAOJ), C. Bennett (JHU), T.-T. Chang (AIAA), M.-Y. Chou (ASIAA), J. Coupon (ASIAA), R. Dekany (Caltech), C. M. de Oliveira (Sao Paulo), O. Dore (JPL/Caltech), T. Goto (Hawaii), J. Gunn (Princeton), K. Hayashi (Tohoku), S. Hayashi (NAOJ), T. Heckman (JHU), C. Hikage (Nagoya U.), B.-C. Hsieh (ASIAA), K. Ichikawa (Kyoto U.), K. Ichiki (Nagoya U.), M. Imanishi (NAOJ), M. Ishigaki (NAOJ), M. Iye (NAOJ), I. Iwata (NAOJ), O. LeFevre (LAM), L. Lin (ASIAA), Y. T. Lin (ASIAA), I. Kayo (Toho U.), H. Karoji (Kavli IPMU), N. Katayama (Kavli IPMU), D. Kawata (UCL), E. Kirby (Caltech), T. Kodama (NAOJ), Y. Komuro (Tohoku U.), K. Maeda (Kavli IPMU), R. Mandelbaum (Princeton), T. Marriage (JHU), T. Matsubara (Nagoya U.), K. Matsuoka (Ehime U.), B. Menard (JHU), S. Mineo (U. Tokyo), H. Miyatake (U. Tokyo), A. More (Kavli IPMU), S. More (Kavli IPMU), T. Morokuma (U. Tokyo), K. Motohara (U. Tokyo), L. Moustakas (JPL), Y. Matsuda (Caltech), S. S. Murray (JHU), F. Nakamura (NAOJ), T. Nishimichi (Kavli IPMU), A. Nishizawa (Kavli IPMU), M. Oguri (Kavli IPMU), S. Okamoto (Beijing), Y. Okura (NAOJ), Y. Ono (U. Tokyo), P. Price (Princeton), A. R. Pullen (JPL), R. Quimby (Kavli IPMU), A. Raccanelli (JPL), M. Sato (Nagoya U.), M. Seiffert (JPL), A. Shimono (Kavli IPMU), D. N. Spergel (Princeton), D. K. Stern (JPL), H. Sugai (Kavli IPMU), S. Saito (Berkeley), T. Saito (Kavli IPMU), T. Storchi-Bergmann (IF-UFRGS, Brazil), Y. Suto (U. Tokyo), N. Suzuki (LBL), A. Szalay (JHU), R. Takahashi (Hirosaki U.), N. Takato (NAOJ), M. Tanaka (Kavli IPMU), M. Tanaka (Tohoku), A. Taruya (U. Tokyo), N. Tominaga (Konan U.), Y. Urata (NCU), K. Yamamoto (Hiroshima U.), K. Wada (Kagoshima U.), W.-H. Wang (ASIAA), R. Wyse (JHU), T. Yamada (Tohoku U.), N. Yasuda (Kavli IPMU), N. Zakamska (JHU)

PFS Project Office

H. Karoji (Kavli IPMU), H.-H. Ling (ASIAA), Y. Ohyama (ASIAA), H. Sugai (Kavli IPMU), A. Shimono (Kavli IPMU), N. Takato (NAOJ), N. Tamura (Kavli IPMU), A. Ueda (NAOJ)